Flexible Graphene-Based Passive and Active Spinal Cord Implants

Andrada Iulia Velea

Supervisors
Dr. **Vasiliki Giagka**, Dr. ir. **Sten Vollebregt**

Biomedical Engineering
Specialization: Medical Devices and Bioelectronics

TU Delft Delft University of Technology

Challenge the future

2019

Flexible Graphene-Based Passive and Active Spinal Cord Implants

By

Andrada Iulia Velea

in partial fulfilment of the requirements for the degree of

Master of Science
in Biomedical Engineering
Specialization: Medical Devices and Bioelectronics

at Delft University of Technology,
to be defended publicly on Friday December 13th, 2019 at 10:00 AM.

Supervisors:	Dr. Vasiliki Giagka	
	Dr. ir. Sten Vollebregt	
Thesis committee:	Prof. dr. ir. Wouter A. Serdijn,	TU Delft
	Prof. dr. Peter G. Steeneken,	TU Delft

This thesis is confidential and cannot be made public until December, 2020.

An electronic version of this thesis is available at http://repository.tudelft.nl/.

Abstract

The spinal cord, considered to be the most important path of the human body, when injured induces severe motor dysfunction. Therefore, patients affected by lesions on the spinal cord, are most of the time unable to walk, stand or perform motor activities that are trivial for healthy people. To provide a better quality of life for these patients, extensive research and effort have been put by both neuroscientists and engineers to provide clinical therapies for pain relief and locomotion restoration together with dedicated platforms that could deliver these therapies. Currently, for these purposes, epidural spinal cord stimulation is widely used. Apart from being used as a method to reduce pain, it has also been proven to promote locomotion recovery.

Apart from clinical trials, it is of great importance to understand the mechanisms that occur while delivering specific therapies. To this end, more exploratory research is mostly conducted in rodents. However, the availability of tailored neurotechnologies, for experiments conducted in small animals, is limited mostly due to size constraints. Moreover, when developing implantable devices that would target the spinal cord, careful selection of the materials used is equally important. However, understanding the underlying mechanism leading to a specific behaviour or motor outputs requires exploring and quantifying new methods of stimulation. For instance, optogenetics has been gaining a lot of popularity in the field of neural stimulation as it is a more specific technique that could help neuroscientists map the neuronal circuitry within the human body. Thus, apart from developing spinal cord implants that resemble best the anatomy of the body, while inducing as little stress as possible on the spinal cord, for exploratory reasons the developed implants must provide optogenetic compatibility.

Therefore, this thesis reports the development as well as the characterization of both passive and active spinal cord implants with optogenetic compatibility.

To achieve the desired goal of having a fully implantable, flexible spinal cord implant with optogenetic compatibility, a scalable and reproducible microfabrication process has been developed. Materials such as graphene, for transparency, flexibility and conductivity were used to develop the microelectrode arrays. Moreover, soft, polymeric encapsulation was employed to sustain the high flexibility and transparency of the implant. The end result of the microfabrication process would lead to a device consisting of a multi-layered graphene structure between two polymeric-based encapsulation layers and metal test pads for interconnection to the outside world. However, towards achieving this final structure, several challenges were encountered. Suspension of the implants after developing them on a rigid substrate, yet ensuring high quality for the graphene layer leads to several iterations of the fabrication process. Despite the challenges encountered, several prototypes were successfully developed. However, having prototypes that can only validate the process flow would not suffice. Therefore, extensive evaluation of the devices has been conducted and reported. Methods such as Raman spectroscopy and optical transmittance to evaluate the graphene layer or cyclic voltammetry and electrochemical impedance spectroscopy to characterize the performance of the fabricated devices were employed. The degree of transparency obtained using the reported microfabrication process was ~78 %, leading to the conclusion that the number of graphene layers for the final device was 10. It has been proven that graphene does not deteriorate over time when soaked in saline solution for several consecutive days and apart from that, the graphene-based implants showed no performance deterioration when bent over rods down to 3 mm in diameter. Moreover, the graphene electrodes provided impedance values of ~8 kΩ at 1 kHz frequencies, values comparable to what literature has previously reported.

Apart from developing a passive graphene-based spinal cord implant, the focus of this thesis was also to fabricate and characterize an active implant. However, embedding active components with a flexible, graphene-based array of electrodes is not trivial. Therefore, system integration of small test chips was investigated and after several iterations of flip-chip bonding processes, a complete, active, graphene-based prototype was obtained. The measurements performed after the bonding process have proven that both bonding on graphene-only as well as on graphene and metal substrates is possible and the four-point measurement results indicated resistance values ranging from 10 mΩ up to 16 Ω for individual connections, depending on the substrate used.

Therefore, with this research project, not only the first fully transparent, graphene-based spinal cord implants have been developed but also the results obtained from their characterization illustrate that the process is stable and the performance of the devices is promising.

Acknowledgement

I would like to express my sincere gratitude to all people who, in the past year, have contributed significantly to my development as a researcher as well as a person.

First, I would like to address special thanks to Vasso and Sten for guiding me through all the stages of this complex and challenging MSc thesis project and for being there, available and ready to answer my questions at all times. Even when things seemed hopeless and I ended up being in stressful situations, you were always there ready to sacrifice time and energy to clarify things. Seeing you both being so passionate and involved in this project, motivated me to keep working hard and achieve the results that we were aiming for. I am really happy, lucky and honoured to have had the opportunity to collaborate with you, it has been a great pleasure!

I would like to thank Wouter and people from the Bioelectronics group for being so nice, always helpful and friendly and for creating such an amazing atmosphere every day. It has been a great year and I am extremely grateful I had the chance to meet you all!

My office mates, who listened, gave advice and offered support whenever needed, I thank you all! Especially Alberto and Pedro for being great friends, office mates and for creating such an amazing office! Special thanks to the Bioelectronics branch in Berlin for their help with an important aspect of my project, for welcoming me and making my week there a very nice experience!

I would like to thank all people from ECTM and EKL for their help, understanding and for letting me conduct my research in a professional manner.

To all people who helped, suggested ideas or contributed in any way to the development of my project and myself, thank you all! Kambiz and Ronaldo, thank you so much for sharing your knowledge, experience and for willing to help whenever needed. I cannot express in words all my gratitude and happiness for having the chance to meet you, learn from you and exchange ideas with you all.

Thanks to all my friends, fellow students, and colleagues in Delft for filling up these years with great memories!

To my parents and family for their unconditional support, care, love and for always believing in me! With all the ups and downs, you were there for me, no matter what, believing in my potential and encouraging me at every step! Thanks to you and the education you provided me with, I am here today, hoping to make you proud! This great experience would have never been possible without you and for that, there are not enough words to express my thankfulness.

Table of contents

List of abbreviations

Central Nervous System	CNS
Central Pattern Generator	CPG
Spinal Cord Injury	SCI
World Health Organization	WHO
Epidural Spinal Cord Stimulation	ESCS
Channelrhodopsin-2	ChR2
Halorhodopsin	HaloR
Microelectrode Arrays	MEAs
Platinum	Pt
Application Specific Integrated Circuits	ASICs
Polydimethylsiloxane	PDMS
Gold	Au
Platinum-Iridium	PtIr
Electrocorticography	ECoG
Indium-Tin Oxide	ITO
Polu(3,4-Ethylenedioxythiophene)	PEDOT
Reactive Ion Etching	RIE
Chemical Vapour Deposition	CVD
Copper	Cu
Nickel	Ni
Molybdenum	Mo
Methane	CH_4
Thermal Expansion Coefficient	CTE
Silicon	Si
Poly-methyl Methacrylate	PMMA
Reduced Graphene Oxide	rGO
Cyclic Voltammetry	CV
Else Kooi Laboratory	EKL
Tetraethyl Orthosilicate	TEOS
Plasma-enhanced Chemical Vapour Deposition	PECVD
Photoresist	PR
Ultraviolet	UV
Aluminium	Al
Titanium	Ti
Hydrofluoric Acid	HF
Phosphoric Etch Solution	PES
Hydrogen Peroxide	H_2O_2
Buffered Hydrofluoric Acid	BHF
Deep Reactive Ion Etching	DRIE
Through-Si Vias	TSV
Flex-to-Rigid	F2R
Non-Conductive Adhesive	NCA
Gold-Palladium	AuPd
Electrochemical Impedance Spectroscopy	EIS
Charge Storage Capacity	CSC
Dorsal Root Ganglia	DRG
Potassium Hydroxide	KOH
Computed Tomography	CT
Nickel	Ni
Anisotropic Conductive Adhesive	ACA
Length-to-Width	L/W
Phosphate-Buffered Saline	PBS
Octafluorocyclobutane	C_4F_8
Helium	He
Tetrafluormethane	CF_4
Sulfur Hexafluoride	SF_6

List of figures

List of tables

1. Introduction

1. 1. Spinal cord and spinal cord injuries (SCIs)

The spinal cord, a structure that constitutes the central nervous system (CNS), together with the brain, is considered to be the most important path of the human body. Shaped as a long and tubular bundle of nervous tissue, the spinal cord is located within the spinal canal and is protected by the spinal column and three membranes, thus arranged, from the inside to the outside: pia mater, arachnoid mater and dura mater, as shown in Fig. 1**.** The most external of the three is separated from the spinal column by the epidural space [1], [2].

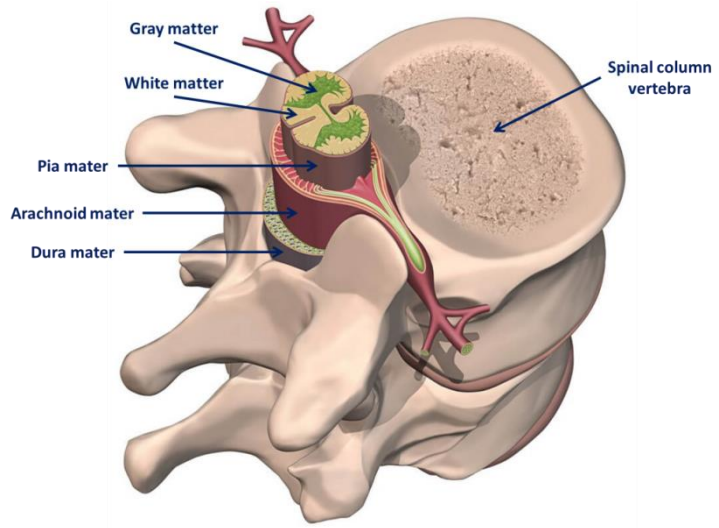

Fig. 1. Cross-section of the human spinal cord featuring its most important structures. Modified from [3].

In humans, the anatomy of the spinal column indicates the presence of 33 vertebrae: 7 cervical (C1-C7), 12 thoracic (T1-T12), 5 lumbar (L1-L5), 5 fused sacral and 4 fused caudal (coccygeal) [4]. The gross anatomy of the spinal column in mice consists of 34 segments: 8 cervical (C1-C8), 13 thoracic (T1-T13), 6 lumbar (L1-L6), 4 sacral (S1-S4) and 3 coccygeal (Co1-Co3), all synthesized in Table 1 [5].

Table 1. Segments and number of vertebrae in human and mouse spinal column anatomy.

Gross anatomy of the spinal column in humans and mice		
Segments	**Human anatomy**	**Mouse anatomy**
Cervical	7 (C1-C7)	8 (C1-C8)
Thoracic	12 (T1-T12)	13 (T1-T13)
Lumbar	5 (L1-L5)	6 (L1-L6)
Sacral	5 (fused)	4 (S1-S4)
Caudal (coccygeal)	4 (fused)	3 (Co1-Co3)

The spinal cord is mainly involved in locomotion and is responsible for delivering sensory and motor information between the brain and the peripheral nervous system. Briefly describing its internal anatomy, this consists of white matter regions, located on the outermost area of the spinal cord, and grey matter regions, located in the centre and comprising most of the spinal neuronal cell bodies. The white matter is formed by longitudinally oriented spinal tracts, while the grey matter is represented by different segments of sensory and motor neurons [6].

Locomotion is a very complex motor behaviour that allows humans to move and interact with their surroundings. Its complexity is due to the fact that it involves different categories of motor neurons as well as different parts of the body. For instance, planning and initiation of a voluntary motor activity occurs in the supraspinal areas, in the brain, while more precise and fine locomotor movements are generated in the spinal cord. The neural circuitry located here, also known as the “central pattern generator” (CPG) is directly involved in the control of reflexes, or rhythmic movements. Together with the sensory neurons, with their body located in

the dorsal root ganglia and which carry important sensory information from the surrounding environment, the motor neurons in the spinal cord form the reflex arc [7], [8], [9].

The term "spinal cord injury" (SCI) is used to describe any kind of damage to the spinal cord, caused either by trauma, disease or degeneration that affects the conduction of sensory and motor information between the brain and the rest of the body [6]. Thus, a SCI indicates that the supraspinal inputs coming from the brain may no longer be involved in locomotion. Therefore, the initiation of voluntary movements may no longer be possible.

According to World Health Organization (WHO), every year, between 250000 and 500000 people suffer from a spinal cord injury, while in the US, according to the National Spinal Cord Injury Association, about 11000 cases are reported yearly and a total of 450000 cases are currently registered [10], [11]. These numbers keep increasing and in most of the cases, SCIs are due to traumatic causes, usually leading to degradation of the quality of life of the patients.

Symptoms of SCIs depend on the location and severity of the injury; the closer the lesion is to the brain, the more effect it has on the human body. Generally, these lesions have a great impact on the ability of people to either stand or walk and this is because whenever a SCI occurs, the area below the site of lesion is the one affected.

Depending on the location, there are different terms used in the neuroscience community, such as:

- Tetraplegia or quadriplegia, when the lesion occurs in the cervical segments of the spinal cord, thus leading to loss of sensory and/ or motor function in the arms, as well as in the trunk and legs;
- Paraplegia, used for lesions occurring in the lower segments of the spinal cord and thus affecting the trunk or legs, but not the arms.

On the other hand, based on the severity of the injury, there can be either incomplete or complete SCIs. In the case of an incomplete lesion, there is a partial preservation of sensory and/or motor function below the site of injury, while in a complete SCI, there is no sign of sensory and motor function in the lowest segment of the spinal cord [6]. For locomotion- and SCIs-related mice experiments, the most interesting areas to be investigated are the spinal cord segments located under the vertebral segments T10 to L2.

Although in SCIs there is little or no supraspinal input coming from the brain, some neural activity still resides inside the spinal cord. For a better understanding of the mechanism behind this neural activity, extensive research has been conducted over the years. In the beginning, different animal species were used but in 2002, some clinical trials on eight patients were performed to prove the presence of neural activity within the spinal cord following a complete SCI. The results have shown that depending on the location of the electrical stimulation, different types of motor responses can be evoked. For instance, stimulating the dorsal surface of the spinal cord segment L2 was very effective in evoking locomotor activity, a clear evidence of the presence of CPG in humans [12].

Two key aspects of the intrinsic activity of the neuronal circuitry in the spinal cord are automaticity and plasticity. Automaticity, in healthy subjects, relates to the ability of performing complex motor tasks unconsciously. In patients affected by SCI, though, it implies that the circuitry in the spinal cord, the CPG, is able to still produce some motor outputs without supraspinal inputs but still receiving peripheral sensory input, as shown in Fig. 2 [9]. On the other hand, plasticity refers to the ability of the spinal circuitry to execute motor tasks if trained accordingly through repetitive activity [13].

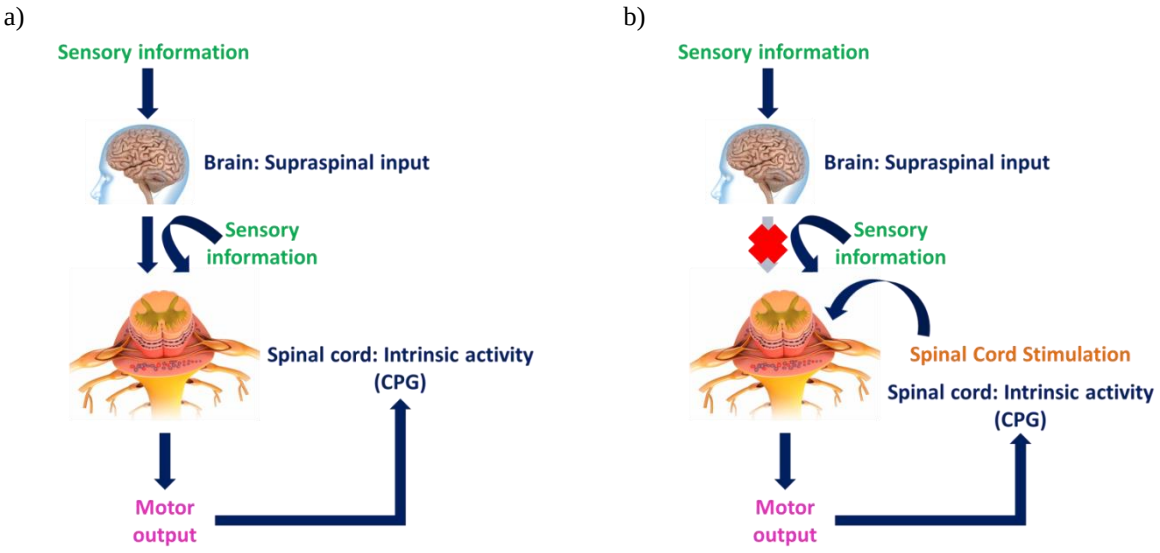

Fig. 2. Representation of the locomotion system and the implication and role of the spinal cord in healthy subjects, a) and spinal cord injured ones, b) (inspired from [9]).

As mentioned previously, in incomplete SCIs there is still some capacity to elicit motor activities in the absence of supraspinal input, if sensory information is still received from the surrounding environment. A very important role in this case is played by the automaticity and plasticity of the spinal cord. Yet, for patients suffering from complete SCIs, external input is required to achieve locomotion. As shown by the results obtained during the clinical trial in 2002 [12], by means of external electrical stimulation of different areas of the spinal cord, locomotor activity can be evoked. This is also known as "epidural spinal cord stimulation" (ESCS).

1. 2. Epidural spinal cord stimulation (ESCS)

Throughout the years, spinal cord stimulation has been showing very promising results in the restoration of motor function following a SCI. Therefore, even nowadays, the neuroscience community is trying to investigate and understand to the smallest detail the underlying mechanism of this technique.

In a traditional fashion, ESCS employs the delivery of electrical pulses to the surface of the spinal cord, using arrays of electrodes implanted outside the dura mater, within the epidural space.

On the other hand, ultimately, the wellbeing and comfort of the patients should also play an important role. Therefore, all devices, especially the implantable ones used for ESCS should resemble best the anatomical configuration of the human body. Unfortunately, currently, the ones available on the market, such as Medtronic, RestoreAdvanced, do not entirely fulfil this requirement. As illustrated in Fig. 3, the active components, encapsulated in a relatively big and stiff titanium case, are implanted somewhere inside the human body, far from the site of stimulation. From this bulky, big and stiff component, leads travel along the spine until they reach the area subjected to stimulation where they terminate into electrodes, used as an interface between the active components and the biological tissue.

Fig. 3. Representation of a typical epidural spinal cord stimulation and its implantation area, together with an illustration from a currently available device (Medtronic RestoreAdvanced).

Apart from the relatively big size of the complete device, the implantation site also constitutes a challenge due to the limited available space for the electrodes to be implanted but also because movements of the vertebrae or of the spinal cord with respect its surroundings are present. Therefore, having leads running along these critical points of the human body is not desired as they might break or cause spinal compression due to the materials used for their fabrication. Ideally, a small, compact and highly flexible implant should be considered for spinal cord applications.

1. 3. Optogenetics

As mentioned previously, ESCS using electrical pulses to activate the biological tissue has shown very promising therapeutical results throughout the years. However, understanding how the tissue responds to different stimulation paradigms is a key aspect in the evolution of the field. Knowing the biological mechanism post stimulation could help neuroscientists quantify and adjust accordingly the therapy provided. To this end, a novel stimulation method, known as optogenetics, has been thoroughly investigated in the past years.

Optogenetics is a neuromodulation technique that can activate in a more type-specific manner the biological tissue using light [14], [15]. However, to be successful, it requires the presence of genetically modified proteins (opsins), such as channelrhodopsin-2 (ChR2) or halorhodopsin (HaloR) that are sensitive and responsive to blue (~470 nm wavelength) or yellow (~570 nm wavelength) light, respectively [15].

The major advantage of using optogenetics as a means of stimulation, instead of the traditionally used, electrical-based one is the fact that it can increase the resolution of activation. This is due to the fact that only neurons that are genetically modified to respond to light will trigger action potentials. Therefore optogenetics is promising to ease the correlation of the evaluated responses to the stimulation location and pattern delivered.

Ultimately, animal experiments conducted in order to validate these optogenetic-compatible probes, have to be performed while the animal under test is moving freely, thus inducing less stress on it throughout the experiment. Moreover, a smart implant that could be used in a closed-loop fashion, stimulating different regions while performing in-situ evaluation of the recorded electrical signals is desired.

Yet, there are some very important aspects that have to be considered while developing such implants. First, the epidural space is limited and because initial prototypes have to be designed for animal experiments, size limitations are even more stringent. Apart from that, the materials used have to provide high flexibility and very little compression of the spinal cord such that the end result could resemble the anatomical configuration of the subject as much as possible. Several such flexible implants for spinal cord applications, developed throughout the years are discussed in detail in the following chapter. However, it is worth mentioning that most of the spinal cord implants that have been reported, although having a certain degree of flexibility, feature opaque, metallic electrodes which are not suitable for optogenetic-related applications. Moreover, the lack of having the active components embedded with the electrode arrays constitutes an important disadvantage as long-term evaluation of the device cannot be performed. Lastly, the encapsulation of some of the flexible spinal cord implants is not ideal as it induces compression of the spinal cord, thus leading to tissue damage and inconclusive measurement results.

1. 4. Aim of the project

As previously mentioned, ESCS has been proven to promote locomotion recovery in patients affected by SCIs [16]. However, the mechanism of action is not yet fully understood by the neuroscience community as the cellular response cannot be quantified and properly evaluated while the biological tissue is being stimulated. Therefore, there is a great need of mapping the neuronal circuitry, in the spinal cord, to the observed effects, during stimulation. Optogenetics, due to its advantage of selectively activate areas of the biological tissue which are of interest, has been gaining a lot of popularity in the field of spinal cord stimulation [14]. Unfortunately, the previously described metal-based active implants are not suitable for simultaneous optical stimulation and electrical recording of the stimulated area. To this end, dedicated platforms that could monitor the cellular activity at the time and location of activation are needed. However, to do so, several research questions have been addressed in this project. For instance, is it possible that the development of such platforms is achieved only by means of microfabrication? Can the transparency and conductivity of the device be achieved by using one material, for instance, graphene? And finally, how can the active components be embedded with a small, flexible, potentially graphene-based implant?

Therefore, the goal of this project is to develop by means of microfabrication, a fully implantable, graphene-based and active implant with soft and flexible encapsulation, for spinal cord applications that could be used both for optical stimulation and electrical recording at the same time. The envisioned design of the implant is shown in Fig. 4.

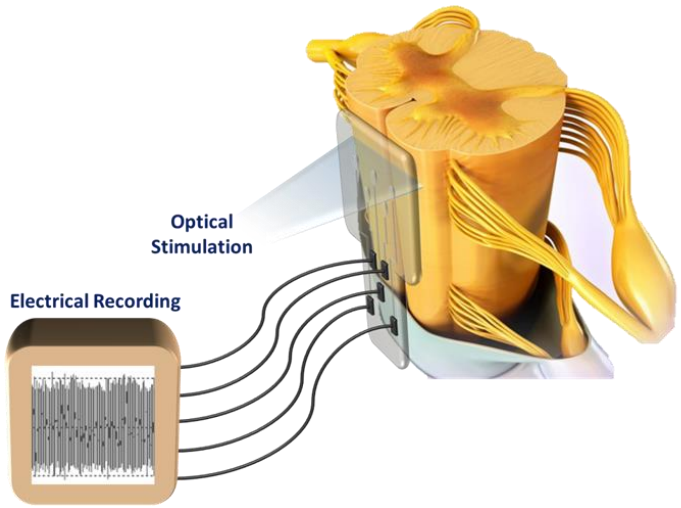

Fig. 4. Envisioned representation of the optically transparent, flexible and active implant for simultaneous spinal cord stimulation and recording in different energy domains.

1. 5. Outline of the subsequent chapters of the thesis

Answering the research questions that define the objective of the project requires thorough investigation of the state of the art.

Therefore, in Chapter 2, a description and critical analysis of different solutions and implementations found in literature are presented.

Based on what has been reported, choices have been made in terms of materials and approaches that should be followed for this project. Such that, Chapter 3 presents a detailed description of the materials used, design considerations and more important the process flow developed for the fabrication of the final envisioned devices. Moreover, Chapter 3 also illustrates the characterization methods used for the evaluation of materials and performances of the fabricated prototypes.

In Chapter 4, the results obtained from the fabrication process as well as from the measurement and characterization of the devices are presented and discussed in detail.

Finally, in Chapter 5, a series of conclusions has been drawn together with a set of future recommendations that could be implemented in order to get a better understanding of the capabilities of the reported devices.

2. State of the art

2. 1. Stimulation of the spinal cord neuronal circuitry

For patients suffering from SCIs, the most important aspect is to regain functionality of their body. To this end, research into the topic of epidural spinal cord stimulation has been initiated as it has been proven to promote restoration of motor functions in patients affected by SCI.

Initially, ESCS was used for treating chronic pain, later expanding its use due to a series of unexpected but very promising results in a patient suffering from multiple sclerosis [17].

Another way to stimulate the spinal cord would be the intraspinal stimulation in which the electrodes, in the form of microwires, are placed inside the spinal cord, penetrating it in order to reach its grey matter and thus the desired area subjected to stimulation [18]. Despite being a potentially more selective and accurate type of stimulation, this method is much more invasive compared to ESCS, since the implantation of the microwires could lead to irreversible tissue damage and thus it is not preferred.

Although it has been shown both in animals and human patients that by electrically stimulating the spinal cord, rhythmic motor movements can be elicited, due to the presence of CPGs [12] or by enhancing the excitability of the spinal cord and therefore reactivating some of the spinal neural networks [19], [20], the ultimate goal of this treatment plan is to restore locomotion. To this end, more recent clinical studies have been conducted in patients suffering from complete SCIs and it has been noticed by Harkema et al., in 2011 that if combined with training paradigms, ESCS is even more beneficial. At the end of the clinical trial, patients were able to stand and perform small voluntary motor movements. Few years later, in 2014, Angeli et al., using the RestoreAdvanced stimulator from Medtronic, showed that following a verbal command, patients could initiate voluntary oscillations between flexion and extension, in their lower limbs, with ESCS present and multiple training paradigms prior to implantation and stimulation [21]. Yet, regardless of all the promising results, the exact mechanism behind the ESCS and its effects are still unclear. Perhaps, using other means of stimulation that could increase the selectivity of the activation site, mapped with the immediate response of the biological tissue or with the observed movements, could lead to a better understanding of the neural circuitry inside the spinal cord.

As illustrated in Chapter 1, one way to achieve better understanding of the mechanisms occurring at the site of stimulation, while stimulating the biological tissue is by means of optogenetics.

Initially, optogenetics has been used for brain applications and different types of probes have been developed depending on the application and its associated requirements. For example, in order to excite single neurons or small neuronal populations, in 2011, LeChasseur et al., developed a microprobe that allowed for both optical stimulation, using an optical fibre and electrical recordings. One of the advantages held by this probe is the small feature size of the implanted tip (~10 μm in diameter). However, it is not a fully implantable system, thus additional external parts are needed for a complete setup [22]. A similar implantable needle probe was developed in 2012 for single-site modulation using, in this case, an array of μLEDs which could potentially provide more stable light emission [23].

As animal testing is of great importance when developing medical devices, it is crucial to have tailored prototypes that could be used in order to obtain accurate experimental results. To this end, different implantable active probes for optogenetic modulation and electrical recording have been developed, where within mm-sized areas, several optical sources could be integrated, together with different other features such as electrical recording or temperature sensing [24]. However, all these probes are targeting brain applications although optogenetics has been shown promising results in spinal cord applications as well, as illustrated by Alilain et al., in 2008. Here, the authors showed that restoration of breathing, following a severe induced-SCI is possible if spinal neurons are optogenetically stimulated [25]. In 2010, Hagglund et al., found out that rhythmic motor output can be initiated when selective activation of neurons in the lumbar regions of mice is employed using blue light [26].

However, due to the complexity of the locomotor system, including different types of tissue that might hinder light transmission or flexibility of the spinal region that could impede proper delivery of light to the desired location, there are some variations in terms of the devices that could potentially be used. For instance, if peripheral nerves are targeted, the most common approach is the use of cuff electrodes that can be wrapped around the nerve and stimulate or modulate the tissue locally [14]. However, if the spinal cord itself has to be evaluated, optogenetic-compatible epidural implants are desired as the electrodes or light-emitting sources can be in direct contact with the tissue subjected to evaluation.

2. 2. Flexible passive and active implants for spinal cord applications

Apart from the complexity of the locomotor system, the spinal cord and neural tissue in general, shows significant mechanical mismatch with the stiff neural implants. Therefore, effort has been put into the design and fabrication of flexible and soft spinal cord implants that could provide long term stability and biocompatibility. Moreover, pairs of electrodes are ideally replaced by microelectrode arrays (MEAs) to investigate or stimulate different areas of the neural tissue. Several such flexible, polymeric-based implants have been reported and investigated in the past years. One example of such implant has been developed and reported by Gad et al., in 2013. In this work, a platinum (Pt) MEA has been developed and encapsulated in a flexible parylene-based material [27]. More recently, Minev et al., in 2015, reported the electronic dura mater or e-dura implant. This consists of an array of stretchable gold interconnects, soft platinum-silicone composite electrodes and soft silicone encapsulation. The stretchability of the complete implant is present due to both the high flexibility of the encapsulation and the microcracked layer of gold present for the interconnects [28].

Yet, these implants, due to the lack of embedded active components, cannot constitute a complete system. They still need to be in contact with the outside world such that either stimulation or recording can be delivered or analyzed. However, for a complete implantable system, with in-situ recording or stimulation capabilities, the active components that are currently bulky and occupy a big amount of area, can be integrated with the passive array of electrodes using application specific integrated circuits (ASICs). In the past years, researchers have been investigating methods to integrate active components or even bare dice on a passive electrode array structure to bring it towards a complete and active implantable system. To this end, passive implants with some additional components have been developed, as presented by Stieglitz et al., in 2005 [29]. Moreover, bare dice have been bonded on a polydimethylsiloxane (PDMS) encapsulated gold (Au) passive MEA to prove the potential of the technology used. However, the bare die in this case was bonded towards the end of the passive implant, on an area that was not supposed to be implanted inside the epidural space of the subject under test [30]. In 2015, Giagka et al., reported a fully implantable, smart and flexible spinal cord stimulator consisting of platinum-iridium (PtIr) tracks and electrodes, three dedicated small and very thin (100 μm) ASICs and PDMS encapsulation [31].

Nonetheless, all the aforementioned implants consist of opaque metal-based electrodes and tracks, making them suitable for electrical epidural spinal cord stimulation or recording, but not for simultaneous optical stimulation and electrical recording. Therefore, the need of developing tailored tools that could monitor the behaviour of the neural tissue at the exact time and location of activation is still unmet.

2. 3. Transparent and conductive materials for the electrode arrays

In optogenetic-related applications, the most important aspect is light transmission, as light is the only source of activation for the biological tissue. Since there is high interest in developing neural implants that could potentially be used for optical stimulation simultaneously with electrical recording, the ultimate goal is to have a fully transparent prototype. Not only the encapsulation has to comply with this requirement but also the MEAs. Moreover, since electrical recording needs to be performed, the material used for the development of MEAs has to be both optically transparent and conductive. This restricts even more the range of possible candidates.

In 2011, Ledochowitsch et al., reported a transparent electrocorticography (ECoG) array of electrodes for simultaneous optical stimulation and electrical recordings using indium-tin oxide (ITO) as a transparent and conductive material for the array [32]. However, ITO is known to be a brittle material, thus not suitable for flexible implants and with a transparency highly dependent on the process [28].

Poly(3,4-ethylenedioxythiophene) (PEDOT) and graphene are two other possible candidates for a flexible, optogenetic-compatible implantable device. The first one is a conductive polymer, highly transparent (T>90%) but with an elastic modulus in the range of GPa [33]. Processing PEDOT is relatively easy, the layers are spin-coated and later etched using a reactive ion etching (RIE) process, being able to obtain layers with a thickness of 100 to 300 nm.

The second listed material, graphene, a carbon-based material, with a transparency of 97.7% and a carrier mobility up to 10000 cm^2/Vs, for a monolayer structure [34] can be uniformly deposited using a chemical vapour deposition (CVD) process. Compared to PEDOT, graphene layers are very thin, 0.335 nm for a monolayer [35]. Therefore, if thin structures, yet mechanically stable and highly flexible, are needed while still maintaining high levels of conductivity, multi-layer structures can be developed [36]. Graphene is represented as a hexagonal arrangement of sp^2 hybridized carbon atoms, each of them forming 3 σ-bonds and 1 π-bond with the neighbouring atoms. The σ-bonds play an important role in the mechanical stability of the material, while the π-bonds, forming the π-band, allow electrons to move freely, a phenomenon known as surface conduction of graphene [37].

Processing graphene can be done in various ways, either by means of mechanical exfoliation, due to the weak Van der Waals forces existent in between graphene layers, as shown by Novoselov et al., in 2004 [38], or, as mentioned previously by CVD processes.

In CVD processes used for graphene growth, a catalyst material on top of which the graphene layer can be deposited is needed. Various metals such as Cooper (Cu), Nickel (Ni) or Molybdenum (Mo) have been used.

In general terms, a CVD process consists of the catalyst exposure to high temperatures, ranging from 800 to 1200 °C in vacuum. Next, gas containing carbon atoms, such as methane (CH_4) is introduced inside the chamber, causing the carbon atoms to be absorbed by the metal catalyst. Then, the temperature drops rapidly, causing the carbon atoms to be pushed from the bulk of the metal to its surface, thus creating a layer of graphene on top of the catalyst, a method known as precipitation [39]. Apart from precipitation, which occurs during the cooling down stage, in a CVD process, graphene can be formed on the catalyst surface at growth temperatures, a mechanism known as isothermal growth [40]. Nonetheless, the process parameters have to be adjusted in accordance to the metal used. For instance, using Ni for graphene growth might lead to problems if the Ni surface is a polycrystalline one. Due to the grain boundaries present, the graphene layer on top might not be uniform. Moreover, carbon solubility is much higher for Ni substrates (0.28 weight % at 1000 °C) compared to Cu (0.006 weight % at 1000 °C). Therefore, Cu has been considered to be a better catalyst for graphene growth. However, among all, Mo seems to be an attractive candidate, offering the possibility of growing thin and uniform layers of graphene due to its extremely low carbon solubility (0.0026 weight % at 1000 °C), thus creating a self-limiting growth process [41]. Moreover, the thermal expansion coefficient (CTE) of Mo, a material property that indicates the degree of expansion upon heating, is much closer to the one of silicon (Si) than to the one of Cu or Ni, hence, Mo is less prone to wrinkle creation during graphene growth [42].

Apart from developing high quality, thin and uniform graphene structures, another advantage of the CVD process is the fact that the metal catalyst can be patterned prior to graphene growth, thus creating graphene structures over desired areas only.

In some cases, graphene has to be integrated with other components or transferred onto other structures. The most common method for transferring graphene is by using polymers, usually poly-methyl methacrylate (PMMA) that can later be removed in solvents like acetone. After completing the growth process, a layer of PMMA is deposited on top. Then, the metal catalyst underneath graphene undergoes a wet etching step for its removal. In the end, the graphene layer, now on a PMMA substrate is placed over the desired area and the polymer on top is removed [39].

However, wet etching steps and mechanical-based transferring methods, in which force is applied could damage the graphene structure, which is not desired especially when used in the development of MEAs for implantable devices. Therefore, alternatives such as transfer-free graphene methods have been investigated and successfully reported by Vollebregt et al., in 2016 [43].

Apart from owning good mechanical, electrical and optical properties, graphene is a good candidate for biomedical applications also due to the fact that it can easily be doped with different materials, thus offering the possibility of developing various biosensors [44].

Regarding the biocompatibility aspect of graphene, there are several studies revealing different and mainly contradictory results. This is partly because, very often graphitic materials are generalized to graphene although there are fundamental differences among them. In a recent review, published by Liao et al., in 2018, it has been shown that CVD graphene provides high quality layers with low level of impurities, thus making it biocompatible with several cell lines. However, reduced graphene oxide (rGO) has indicated signs of cytotoxicity, in a study performed by Syama et al., in 2016, due to the high oxygen concentration [45]. Therefore, depending on the process steps involved in the development of graphene structures, dedicated biocompatibility tests have to be conducted for better understanding.

Considered as a potential candidate for optogenetic-compatible neural implants, graphene-based passive implants have been developed by Park et al., in 2014. The electrodes were made of four layers of graphene, sandwiched between two layers of Parylene-C. The cyclic voltammetry (CV) evaluation indicated comparable results with gold electrodes indicating that graphene can successfully be used for neural applications. Moreover, it has been shown that by using optical monitoring, while electrically stimulating the tissue, provides better insight into the behaviour of the neural tissue subjected to stimulation [46], [47].

However, this implant was developed for brain applications. To the best of our knowledge, neither passive, nor active graphene-based flexible implants for spinal cord applications have been developed to date.

2. 4. Flexible encapsulation for spinal cord implants

Many implantable devices consist of hermetic encapsulation of the active components, generally using titanium (Ti) cases. Although moisture and water vapour cannot reach the active components, thus protecting the implant from the surrounding harsh environment, the final system becomes bulky, stiff and relatively big. To

overcome this, non-hermetic soft, polymeric-based encapsulation is being thoroughly investigated in the field of neural implants, and the most commonly used are PDMS, polyimide and parylene-C [48].

Polyimide is a commercially available type of polymer which can be used in biomedical applications as an insulating or passivation material that can prevent moisture absorption, corrosion and ion transport to the electrical circuitry [48]. However, in 2010, Hiebl et al., presented an *in-vivo* assesment of a polyimide coated cuff electrode placed around the sciatic nerves of rats. The histological analysis results illustrated that after 28 days post implantation, although the electrode-tissue contact was still sufficient to record biologic signals, the formation of fibrous tissue surrounding the implant indicated that the biocompatibility might be affected due to the polyimide insulation layer [49]. Moreover, polyimide typically presents a yellow color [48], thus reducing the optical transparency required for optogenetic-compatible implants.

Parylene, is a group of semicrystalline polymers found in the thermoplast category. Typically, the deposition process consists of a chemical vapour-based deposition, resulting in relatively thin layers (hundreds of nm) of parylene. Among all types, the most common used in biomedical applications is Parylene-C [48]. In 2007, Hsu et al., conducted long-term *in-vivo* experiments for Parylene-C and showed that for more than 100 days, the encapsulation films could still provide hermetic protection as well as long-term stability at temperatures of 37 °C [50]. More recently, in 2013, a comparative study between Parylene-C and PDMS was conducted by Lee et al., on 54 male Sprague-Dawley rats subjects divided into three groups. The control group consisted of subjects that were implanted with uncoated lead coins and the other two experimental groups consisted on subjects that were implanted with lead coins coated either with PDMS or Parylene-C. The implantation site for all three groups was the dorsal subcutaneous tissue. The results reported, demonstrate that after 12 weeks of implantation the inflammatory cell density of PDMS, although decreasing over time, was still higher compared to Parylene-C coated samples. Moreover, infiltration of macrophages around the implantation site was comparably higher for PDMS than for Parylene-C, thus showing that Parylene-C presents better biocompatibility both in acute and chronic phases [51].

However, as illustrated by Scholten et al., in 2015, PDMS tends to be the best candidate for spinal cord applications due to its relatively low elastic modulus, as illustrated in Fig. 4 [52].

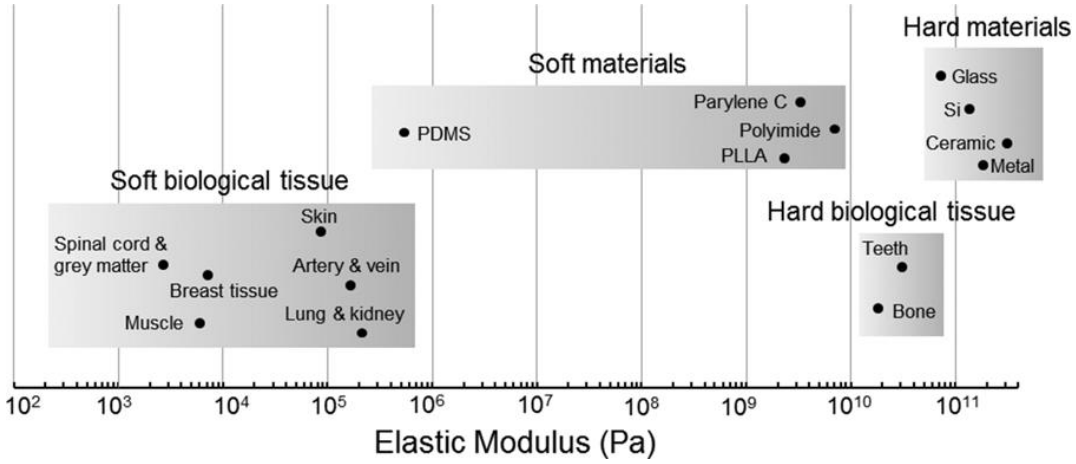

Fig. 5. Classification of different materials with respect to their elastic modulus [52].

To confirm the potential of PDMS for spinal cord applications, Minev et al., in 2015 performed an experiment in which they tested the long-term biointegration of soft implants encapsulated in PDMS, compared to more stiff implants, encapsulated in polyimide. Both types of implants were implanted in healthy rat subjects and significant motor deficits were noticed 2 weeks post implantation, in rats implanted with the polyimide-based samples. The spinal cords were explanted and evaluated 6 weeks post implantation and the results showed moderate to extreme compression of the spinal cord for the areas under the stiff implant. In parallel, a spinal cord model was manufactured and evaluated with both stiff and soft implants. The results were similar to the *in vivo* experiments in the sense that the stiff implant induced significant compression and flattening of the model, whereas the soft, PDMS-based implant did not alter its shape [28]. Therefore, due to the fact that it resembles best the mechanical properties of the anatomical structures, there is an increased interest in using PDMS encapsulation layers for spinal cord applications. Moreover, it is also suitable for optogenetic-compatible applications due to the increase light transmittance within the visible light spectra (T=95%) [53].

Regardless of it being the best candidate so far for spinal cord applications, PDMS, similar to Parylene-C has a relatively low glass transition temperature, usually in the range of 120 up to 150 °C [54]. However, in practice, for temperatures above 90 °C, cracks already start forming. Therefore, thermal limitations have to be taken into account while using PDMS in a microfabrication process.

3. Materials and methods

As previously described throughout the *Introduction* and *State of the art* chapters of this thesis, in order to achieve the desired goal of having an active, flexible spinal cord implant that could be used in optogenetic-related applications, the selection of the materials used is crucial. Therefore, it is of great importance to understand the requirements of the project. First of all, the implantation site for the final prototype is the spinal cord and thus, the materials have to be soft enough not to induce damage or compression of the spinal cord during and after implantation. To meet this goal, as shown in section *2. 4. Flexible encapsulation for spinal cord implants*, the most suitable material is PDMS. Thus, for this thesis, PDMS will constitute the encapsulation of the final structures. Moreover, the spinal cord is subjected to different types and degrees of movements. Therefore, another stringent requirement is in terms of flexibility. The final implant should be flexible enough, yet mechanically stable in order to achieve high performances even when bent. Furthermore, as optogenetics is involved, the final structure has to be highly transparent so that light can pass through and reach the target location for stimulation. To this end, due to the advantages presented in section *2. 3. Transparent and conductive materials for the electrode arrays*, graphene has been chosen as a material for the tracks, electrodes and test pads. However, since the final implant has to be connected to the outside world for data analysis purposes, wires have to be bonded on the available test pads. Thus, in order to ease the assembly process, a metal layer will cover the graphene test pads. It should be noted that for the envisioned design of the implant, the area comprising the test pads will not be implanted inside the epidural space, hence, the risk of compressing the spinal cord or damaging the metal layer on the test pads due to movements, is significantly reduced.

The final envisioned structure of the implant (Fig. 6) will consist of a graphene layer sandwiched between two layers of PDMS as soft and flexible encapsulation. The metal test pads and chips will be placed outside the implantation area to avoid any further damage of the implant and spinal cord.

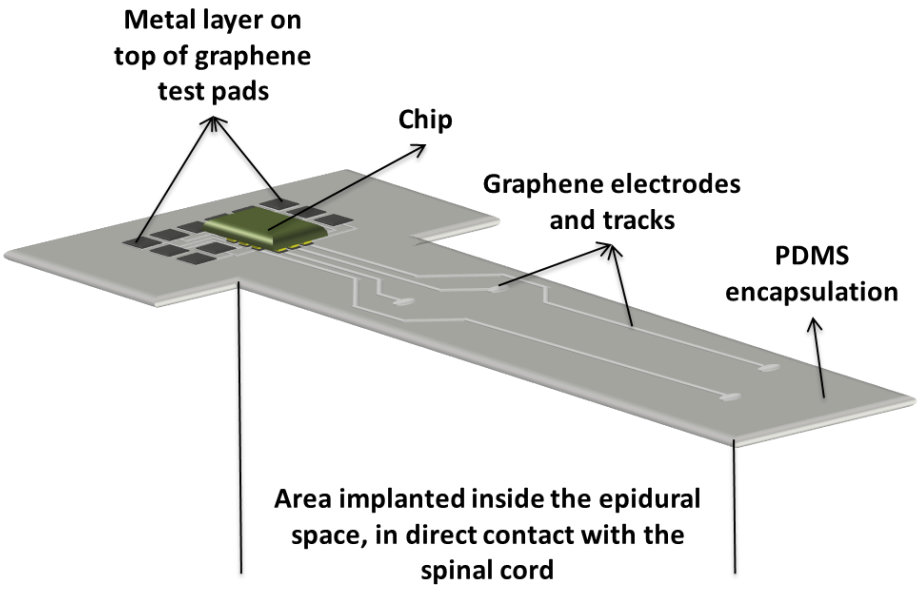

Fig. 6. Envisioned structure together with the final materials that will be comprised in the spinal cord implant.

An important aspect that needs to be mentioned is the fact that for the development of the spinal cord implants, microfabrication processes are used. As the prototypes, will eventually be used also for animal experiments, in order to fully evaluate their performance and interaction with the biological environment, specific requirements in terms of dimensions have been imposed. Therefore, microfabrication, not only ensures scalability and reproducibility of the process but is also able to provide the micron-sized structures needed for this project. To this end, Si wafers will be used throughout the microfabrication processes as a substrate for the development of the spinal cord implants. In Fig. 7, a schematic representation of the design together with the required dimensions is illustrated.

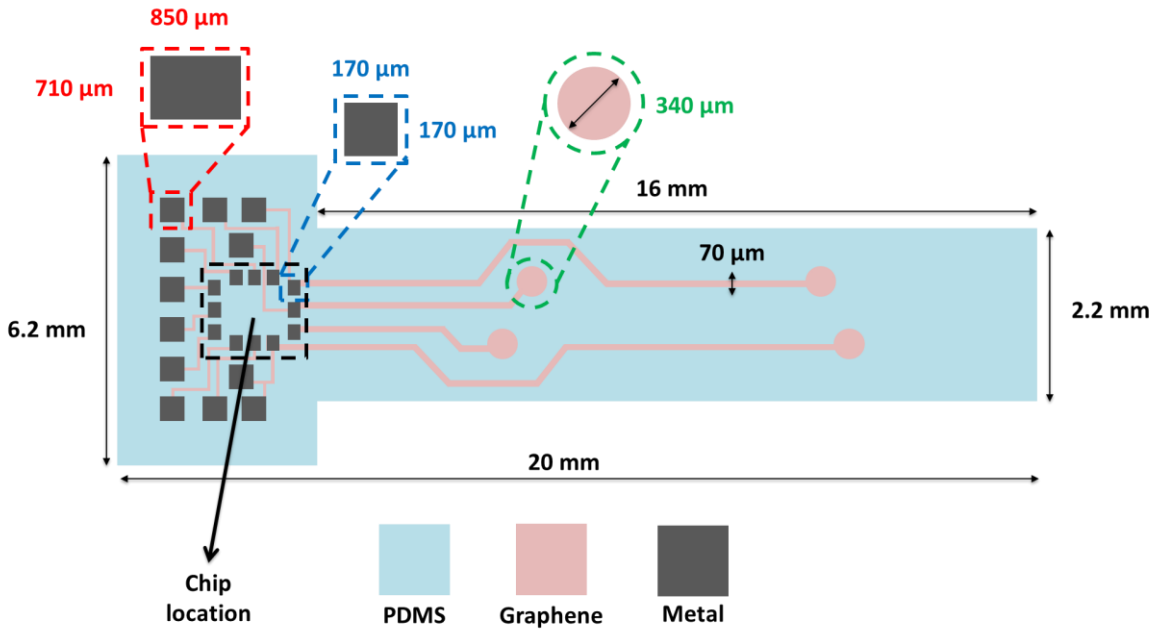

Fig. 7. Schematic representation of the design together with the dimensions used.

3. 1. Development of flexible, graphene-based, passive, spinal cord implants

Microfabrication is generally used to ensure scalability and reproducibility of the process while developing accurate micron-size structures, thus making it of great interest in the field of neural implants. In this section, the process flow for the wafer-level development of a novel, flexible and passive spinal cord implant with optogenetic compatibility is described. To accomplish this, three different aspects have to be evaluated: the wafer-level development of the structure, the encapsulation of it and the release of the final implant from the original rigid substrate. All microfabrication process steps took place inside Else Kooi Laboratory (EKL) from TU Delft.

3. 1. 1. Wafer-level development of a passive spinal cord implant structure

As mentioned previously, a wafer-level approach was chosen for this project. Therefore, the starting material for the microfabrication process is a standard, 4-inch (~10 cm), double-sided polished Si (<100> orientation) wafer with a thickness of 500 µm. All structures defining the implants were created on the frontside of the wafer while the backside was used for later suspension processes. Therefore, 6 µm of tetraethyl orthosilicate (TEOS) precursor-based oxide were deposited on both sides of the wafer by means of a plasma-enhanced chemical vapour deposition (PECVD) process at 350 °C, using a Novellus Concept One tool. For the backside layer of oxide, the thickness was of great importance as later in the process, specific areas of the Si wafer have to be etched through and thus a sufficiently thick hard mask is required. In order to cancel the induced stress from the backside layer of oxide, the same thickness was deposited on the frontside of the wafer as shown in Fig. 8.

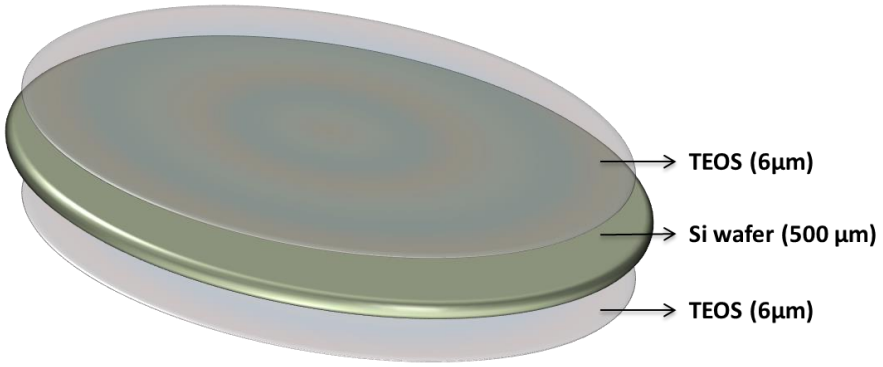

Fig. 8. Frontside and backside PECVD TEOS oxide (6 µm) deposition on a 4-inch Si wafer with a thickness of 500 µm.

The optogenetic compatibility requirement of the project is fulfilled by developing transparent, graphene-based electrodes and tracks. Since uniform and high quality layers of graphene are needed, a chemical vapour deposition (CVD) process, using a Mo catalyst was chosen for graphene growth. Using CVD processes for graphene synthesis, gives the opportunity of developing graphene layers only over desired areas, since the catalyst used can be patterned before graphene growth. Depending on the metal catalyst used and the CVD process parameters, multi-layered graphene structures are prone to be developed. However, this constitutes an advantage for the current project due to the misalignment of the graphene grain boundaries within the layers, thus providing more mechanical stability of the entire structure.

For the current project, Mo was chosen as a catalyst, due to the advantages mentioned in section *2. 3. Transparent and conductive materials for the electrode arrays* of this thesis. Therefore, layer of 50 nm of Mo was sputtered at 50 °C, using Trikon Σigma tool, on top of the 6 µm of oxide previously deposited on the frontside of the wafer. After Mo deposition, lithography steps were employed in order to define the final design of the electrode array and tracks. For this, 2.1 µm of positive SPR3012 photoresist (PR) were spin-coated on top of Mo and baked at 95 °C using the EVG120 Coater-Developer tool. Next, the PR layer was exposed to ultraviolet (UV) light, using the BE2325-GRAPHENE bright-field chromium mask in the EVG420 Contact Aligner tool. After exposure, the PR was developed using Shipley MF322 developer inside EVG120 Coater-Developer. Etching of the metal layer was then performed at 25 °C using Trikon Ωmega 201 tool. Next, a CVD process for graphene growth, at temperatures of about 915 °C, using Aixtron BlackMagic tool was employed. Growing graphene on a Mo catalyst layer is a method inspired from Vollebregt et. al., [43]. The described steps are illustrated in Fig. 9.

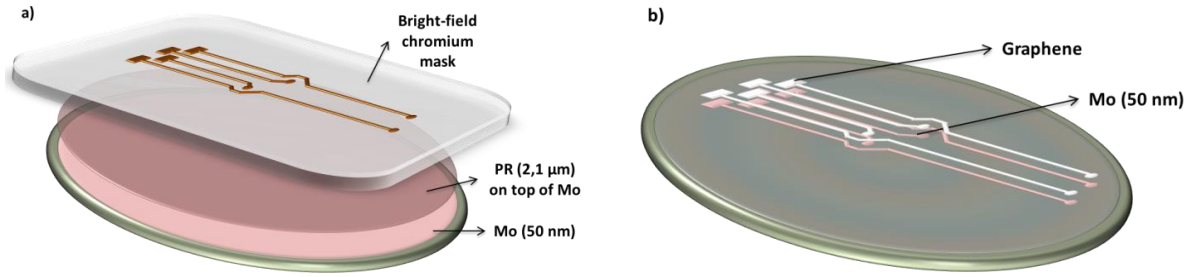

Fig. 9. Graphene growth process using a metal catalyst. In a), Mo (50 nm) deposition and patterning. In b), graphene growth.

A cross-section representation for the complete process flow used in the development of graphene-based passive structures on a Si wafer is illustrated in Fig. 10.

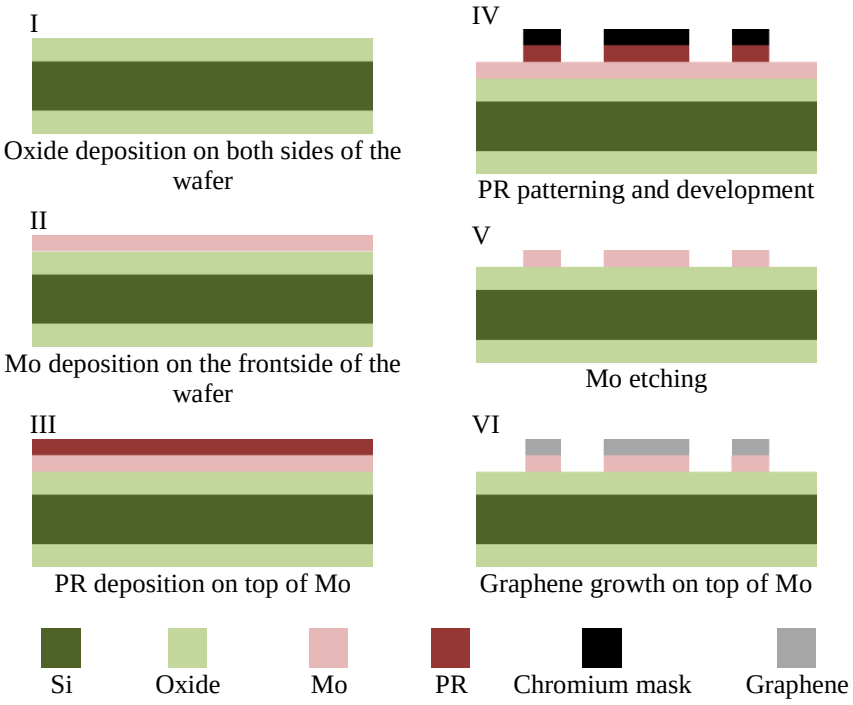

Fig. 10. Process flow for the development of passive graphene-based structures on a Si wafer.

3. 1. 2. Encapsulation of the passive structure

After having the passive structure defined on a wafer-level, encapsulation and transfer process steps have to be employed such that later, the graphene-based passive implant can be removed from the wafer and further characterized. For the complete characterization of such an implant, electrode openings, together with access points for the test pads have to be defined. The flexible, polymeric-based encapsulation layer will be uniformly spin-coated over the wafer and later, the electrodes and test pads will be opened. To avoid damaging the graphene layer while etching the polymer on top, a metal layer has to be deposited over the areas that have to be protected. Since for further electrical characterization of the device, wires have to be soldered on the test pads, a layer of aluminium (Al) is needed but based on literature, Al has been proven to have poor adhesion to graphene [55]. Therefore, an intermediate layer between graphene and Al is needed and as Ti shows a reduced contact resistance to graphene, it has been chosen to improve the adhesion of the structure [56], [57]. Thus, a stack of metal layers composed of 100 nm of titanium (Ti) and 675 nm of Al is sputtered at 50 °C on top of the existent graphene layer using Trikon Σigma tool.

Next, another set of photolithographic steps is employed to define the metal areas that have to be kept on top of graphene. To do so, 3.1 µm of positive PR are spin-coated on top of the metal stack, later being patterned using the BE2325-METAL bright-field chromium mask. Etching of the metal is, in this case, performed using wet etchants, more specifically, using 0.55 % hydrofluoric acid (HF) solutions. It should be noted that the metal catalyst on top of which graphene has been grown, is still present at this stage and should only be removed before applying the final encapsulation layer, to ensure graphene stability throughout the process steps. Hence, the etchant used to remove the unwanted metal layer that is on top of graphene should be selective to Mo. The expected etch rate for the Al and Ti stack in 0.55 % HF ~55 nm/ min, respectively. Therefore, approximately 15 min are enough to etch the complete stack of metals. To prevent the PR layer from peeling off during the etching process, due to moisture that could accumulate at the interface between the PR layer and the metal underneath, an extra baking step at 115 °C for ~30 min was employed after patterning. The aforementioned process steps are synthesized in Fig. 11.

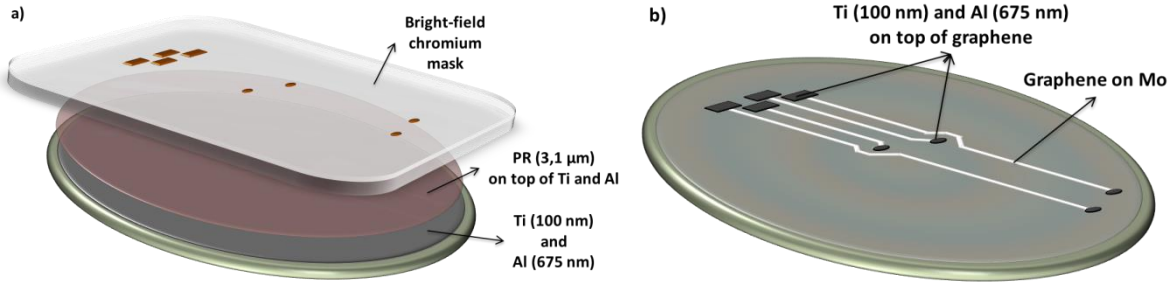

Fig. 11. Metal sputtering on top of graphene to protect the layer during following process steps. In a), Ti (100 nm) and Al (675 nm) deposition and patterning. In b), the metal layer etched from the unwanted areas.

Having the patterned metal layer on top of graphene, the first layer of polymeric-based encapsulation has to be applied. To this end, 50 µm of Sylgard 184 polydimethylsiloxane (PDMS) were spin-coated and cured at 90 °C for one hour. Next, the openings for the electrodes and test pads have to be created using a dry-etching process step. To do so, first, 500 nm of Al are sputtered on top of PDMS and later patterned using photolithographic steps and a dark-field chromium mask (BE2325-PDMS). This metal layer represents the hard mask for PDMS etching and it also provides extra mechanical support for the passive implant during the later steps needed to release the structure from the wafer. Therefore, after creating the openings in PDMS, this metal layer was not removed. A visual representation of these process steps is shown in Fig. 12.

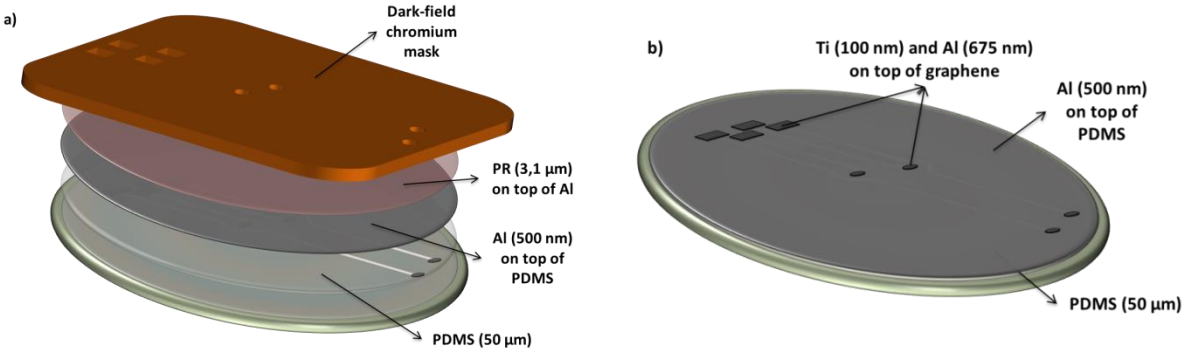

Fig. 12. First polymeric-based (PDMS) encapsulation layer applied on top of the structure. In a), the spin-coating of 50 µm of PDMS is shown. On top, 500 nm of Al are sputtered and patterned to later create the openings in PDMS. In b), the structure after performing the etching steps is represented. The protective metal layer (Ti and Al) is now exposed.

In Fig. 13, a representative cross-section for the process steps used in the encapsulation of the graphene-based passive structures is illustrated.

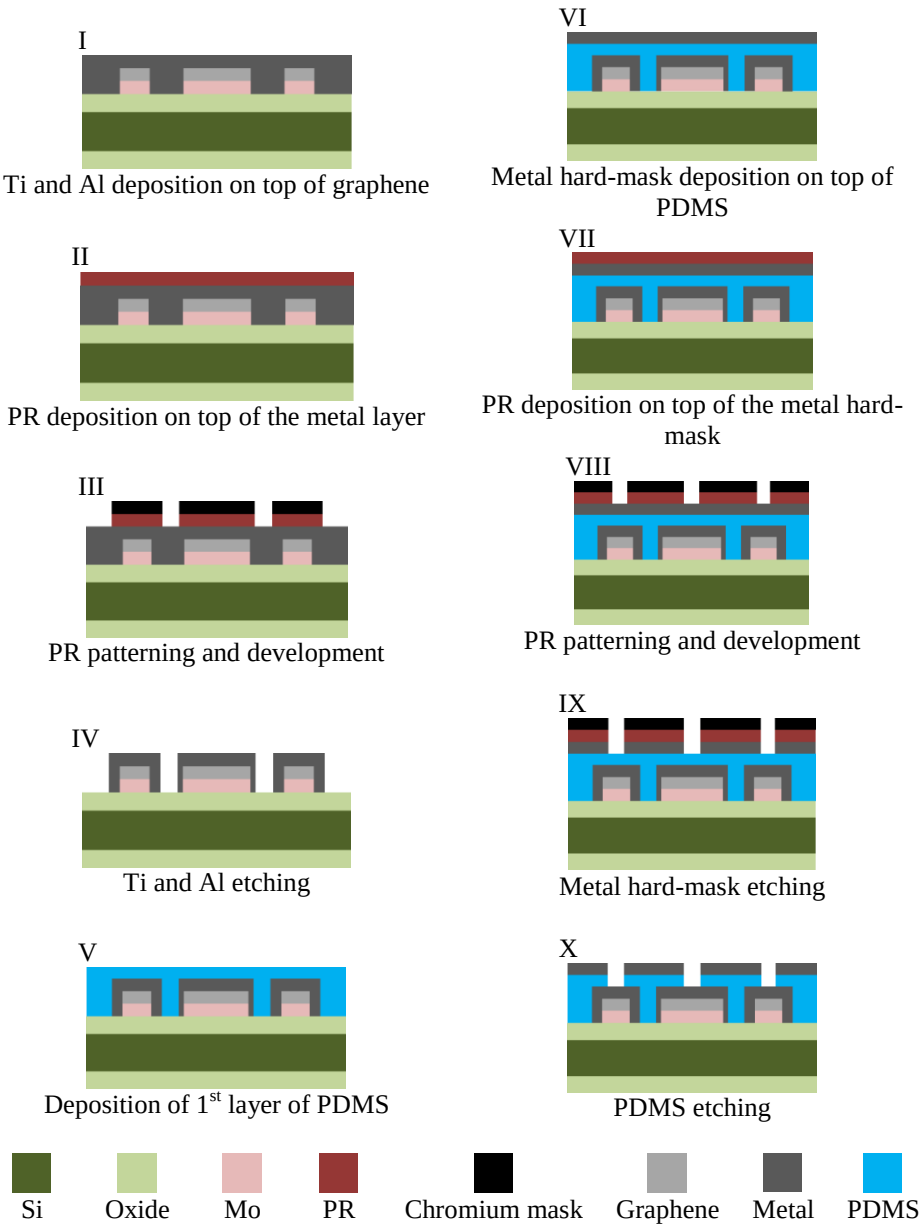

Fig. 13. Process flow for the encapsulation of passive graphene-based structures.

3. 1. 3. Release of the final passive implant from the Si rigid substrate

Having the complete structure defined and already encapsulated with the first layer of PDMS but still on a rigid substrate, does not imply that the final passive implant has been developed. To this end, the structure has to either be removed or partially released from the Si wafer such that the second layer of encapsulation could be applied. Furthermore, electrical, mechanical, *in-vitro* and, potentially, *in-vivo* characterization of the implant has to be conducted, thus no rigid substrates should be present.

3. 1. 3. 1. Transfer approach

One approach would be the complete transfer of the graphene-on-PDMS structure from the original wafer onto a target wafer, previously coated with a layer of PR for bonding purposes. The transferring approach requires the usage of wet etching methods, such as phosphoric etch solution (PES) or hydrogen peroxide (H_2O_2) etchants, for Mo removal and then spin-coat the final encapsulation layer and manually cut out the implant. Since the percentage of Mo area is small compared to the Si wafer surface and completely encapsulated in PDMS, the etchant would have no access points to reach the target layer. Therefore, first, the oxide layer has to be removed using buffered hydrofluoric acid (BHF) 7:1.

Similar to Mo, the access points for BHF are relatively few, being present only at the outermost ring of the Si wafer, thus the etchant cannot easily reach the target material. To circumvent this, more access points have to be created before developing the structure on the frontside of the wafer, as illustrated in Fig. 14. Hence, after depositing the 2 layers of PECVD oxide on both sides of the wafer, the backside oxide was patterned and etched using a 10 x 10 mm die size wafer-stepper mask with round-shaped structures having diameters ranging from 3 µm up to 150 µm. The dry etching process was employed using Drytek 384T plasma etcher from EKL. With the oxide layer patterned, openings in the Si layer had to be created such that later the etchant could reach the frontside oxide layer. To do so, a deep reactive ion etching (DRIE) process was performed to fully go through the Si layer in an anisotropic manner, thus creating high aspect ratio through-Si vias (TSV). In this approach, the frontside structures were developed on top of multiple oxide membranes.

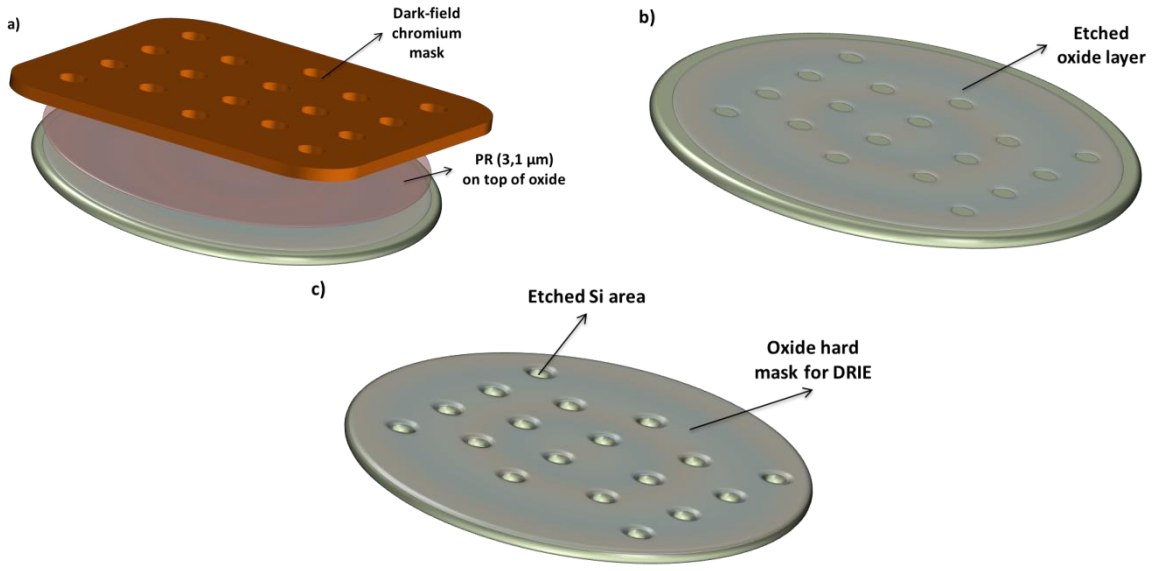

Fig. 14. Backside preparation of the Si wafer before structure development on the frontside. In a), photolithography steps are shown. In b), the backside oxide after plasma etching is illustrated. In c), the wafer after DRIE process steps.

The cross-section in Fig. 15, illustrates the microfabrication process steps needed for the first approach used for transferring the complete passive structure onto a target wafer in order to apply the final layer of PDMS encapsulation.

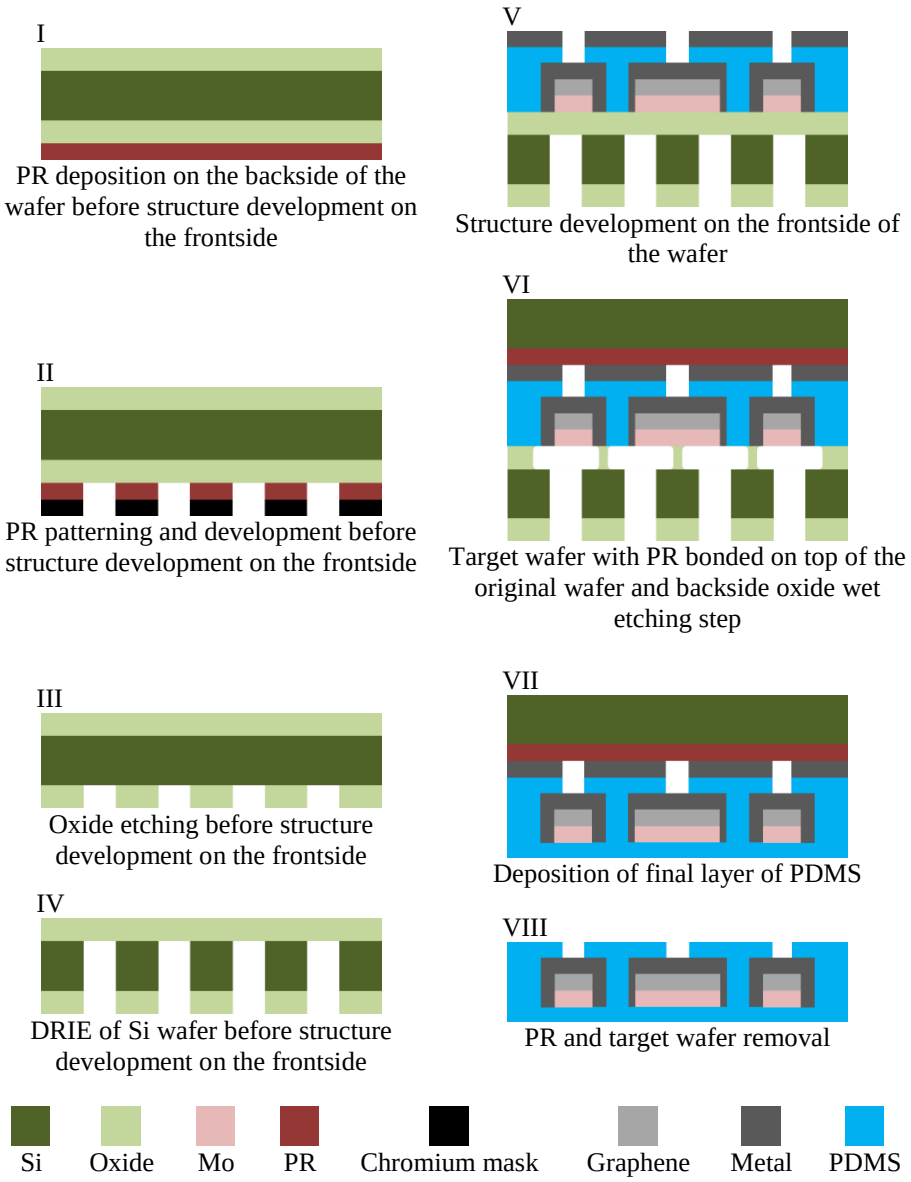

Fig. 15. Process flow for transferring the passive graphene-based structure onto a target wafer and applying the final layer of PDMS encapsulation.

3. 1. 3. 2. Flex-to-rigid approach

Taking into account that later in the process, graphene will be grown at temperatures above 900 °C, the oxide membranes could break due to the induced high thermal stress. Moreover, to avoid any degradation of the graphene and PDMS layers, the amount of wet process steps should be reduced as much as possible. Therefore, a second approach, inspired by the flex-to-rigid (F2R) method [58], was investigated. This consists of a DRIE process, on the backside of the wafer, for the suspension of each implant area, performed after the complete development and encapsulation of the frontside structures. To be able to perform the DRIE process, the backside oxide has to be prepared beforehand. Thus, after depositing both, front- and backside oxide layers, photolithography, using a dark-field chromium mask (BE2325-DRIE), is employed, followed by a dry-etching step for the backside oxide, as shown in Fig. 16.

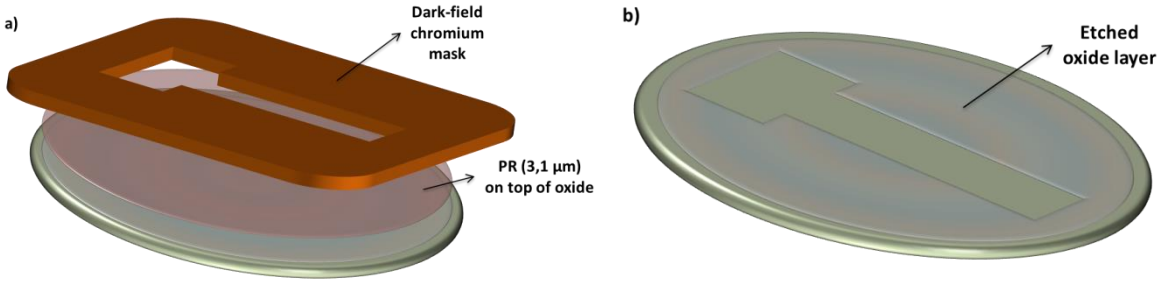

Fig. 16. Backside preparation for future DRIE steps. In a), photolithography steps are shown. In b), the backside oxide after plasma etching is illustrated.

After developing the structures on the frontside of the wafer, DRIE steps can be performed for their suspension. The stopping layer for this process is the oxide on the frontside of the wafer which will later be removed either in BHF 7:1 or employing a dry etching step. The etch rate of PECVD oxide in BHF is 150 nm/ min, thus, a total calculated etching time of 40 min is needed for the complete removal of the oxide. Next, the Mo layer underneath graphene would be removed in H_2O_2, step followed by the spin-coating of the second layer of PDMS encapsulation.

Since one of the aforementioned process steps requires the use of BHF which also etches Ti and Al, the frontside of the wafer has to further be protected, either by using a dedicated holder or by a thick PR layer to avoid having a free-standing layer of graphene, where the electrodes and test pads are, that would likely break during PDMS spin-coating, due to the high spin speeds employed in this step. Therefore, after performing the Bosch process (DRIE), ~16 µm of PR are spray-coated on the frontside of the wafer. Spray-coating is employed due to its better step coverage compared to spin-coating, when high topography is present. In case dry etching methods are employed for the removal of the oxide layer, spray-coating PR on the frontside is no longer needed. Fig. 17 and Fig. 18, illustrate the process steps required for suspending the passive implant structure.

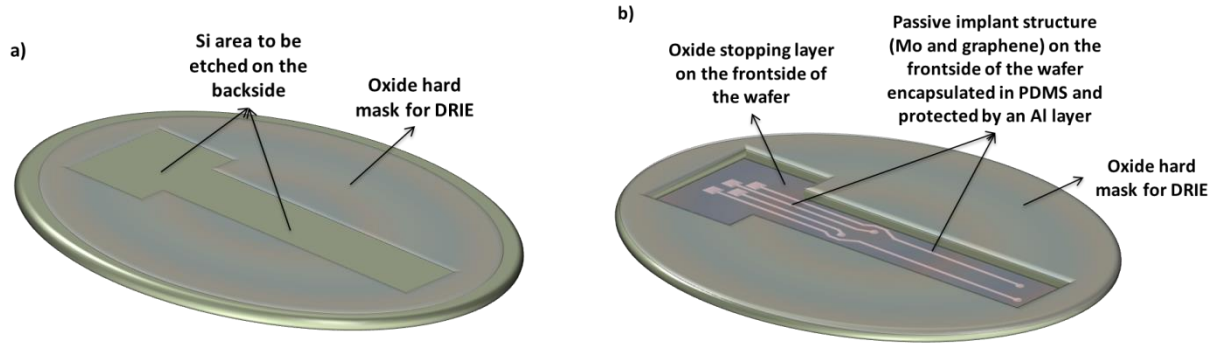

Fig. 17. Bosch process (DRIE) performed from the backside of the wafer. In a), the wafer before DRIE. In b), the wafer after DRIE process steps. The oxide stopping layer on the frontside of the wafer is still present and the passive implant structure can be seen through its transparency.

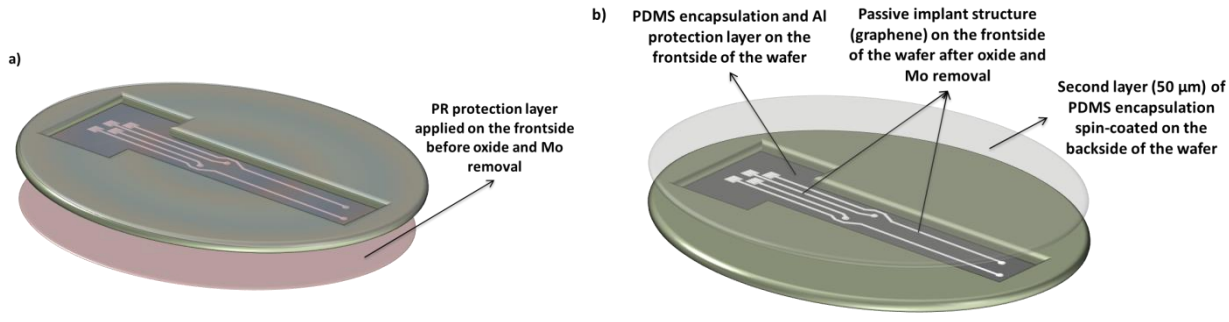

Fig. 18. Oxide and Mo layers removal together with second layer of PDMS encapsulation. In a), the frontside of the wafer is protected by a layer of PR before immersion in BHF and peroxide. In b), the second layer of PDMS is spin-coated on the backside of the wafer after the removal of the oxide and Mo layers.

Having the passive implant completely encapsulated in PDMS, the protection layers on the frontside of the wafer can be removed. For PR removal, acetone is used while for the Al layer underneath, a BHF wet etching step is locally employed since the metal layer on top of the test pads has to remain for further soldering of

external wires for electrical characterization. The last step performed is the manual removal of the implants from the wafer, using a metal blade. In Fig. 19, the last process steps needed to develop the flexible, graphene-based, passive implant are shown.

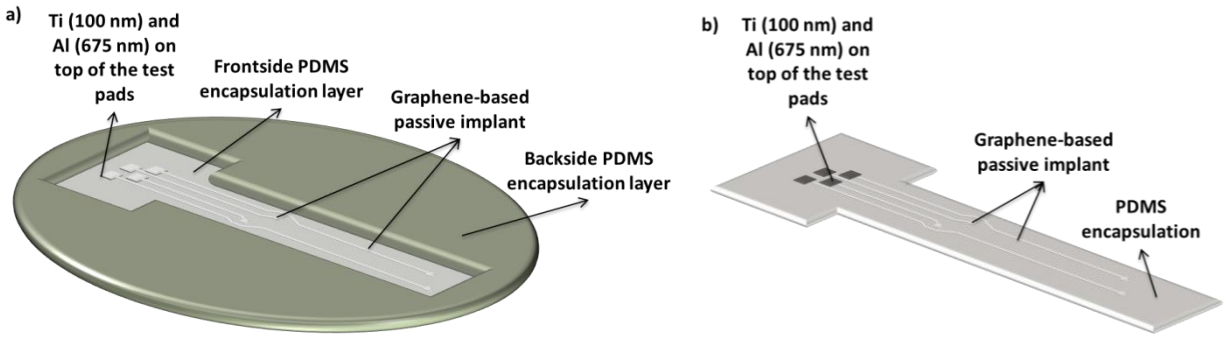

Fig. 19. PR and metal layers removal. In a), the graphene-based passive implant on a wafer-level. In b), the passive implant removed from the wafer. Note that on top of the test pads, the metal layer is not removed.

The process flow for the second approach used for the release of the final passive structure from the rigid Si substrate is illustrated by the cross-section in Fig. 20.

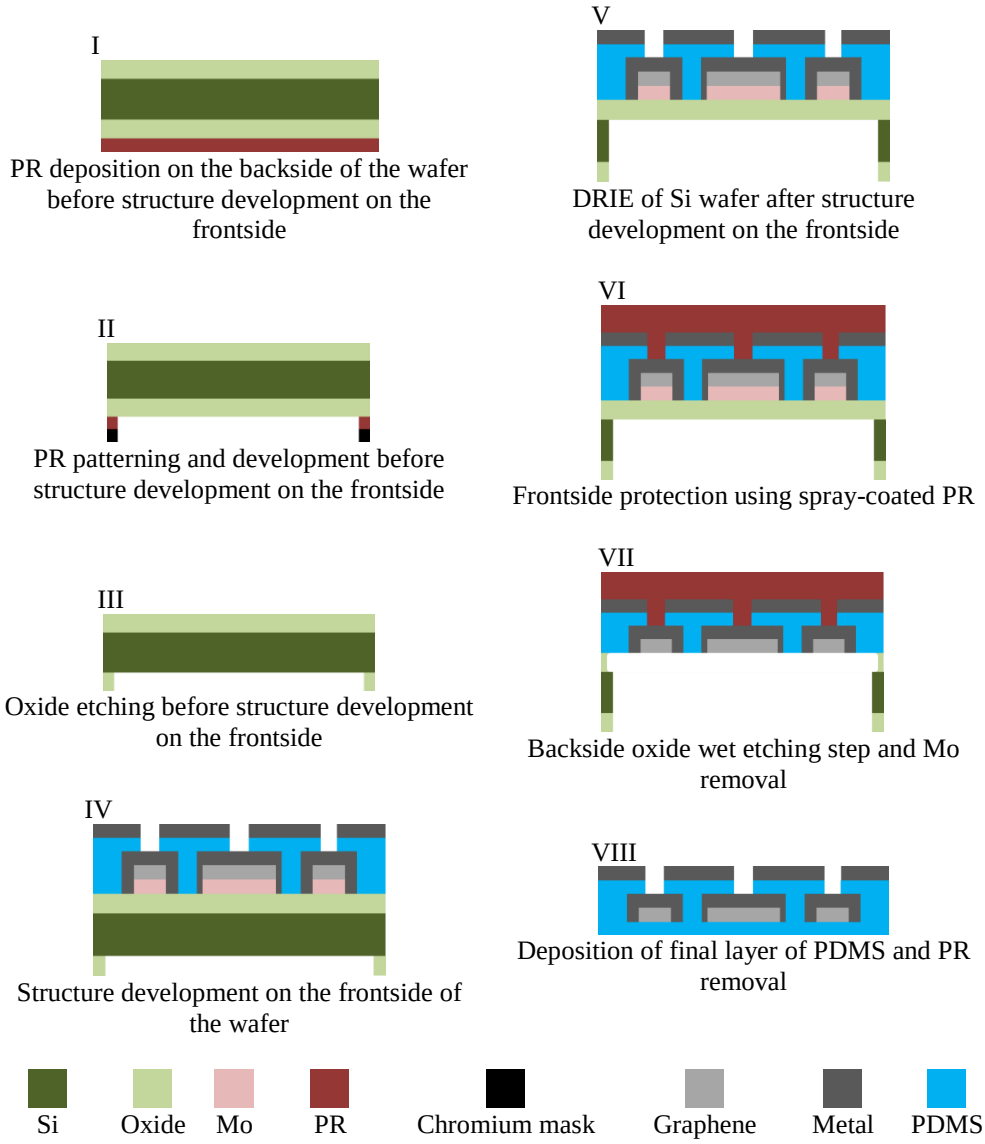

Fig. 20. Process flow for releasing the passive graphene-based structure from the rigid Si substrate and applying the final layer of PDMS encapsulation.

3. 2. From passive to active spinal cord implants

Having just a passive, transparent and flexible implant limits the *in-vivo* experiments to the so-called acute experiments which are conducted over short periods of time. This is because the passive implant has to be connected to the outside electronic system to record the evoked response of the cells and thus the subject under test has limited freedom of movement and is possibly exposed to higher levels of stress. Long-term evaluation of the stimulated area is of great interest due to the plasticity effect that appears in the spinal cord. However, this requires the use of smart, active implants.

Active implants for spinal cord applications, currently available on the market, consist of several components, as mentioned in section *1. 2. Epidural spinal cord stimulation (ESCS)* of this thesis, which make them bulky and stiff.

Ideally, in order to have a smart implant, active components have to be embedded with the electrodes such that signal processing of the recorded signals can be performed in-situ. Embedding the active components with the electrode array implies having them in the form of application specific integrated circuits (ASICs) and bonded on top of the array. Therefore, bonding techniques have to be explored, together with several other process steps, such that from a passive device, to obtain a fully integrated, compact and active implant.

The process steps remain unchanged until the first layer of PDMS has to be applied. Before performing this step, the dummy chips, developed for testing, have to be bonded on the graphene-based substrate. Since the final device will be a flexible implant, flip-chip bonding techniques were employed at this stage, to ensure that the bonds created will not be damaged during handling and torsion, as could happen if wire-bonding techniques were used. Therefore, dummy chips, with gold (Au) stud bumps manually placed on their pads, were bonded using thermocompression flip-chip bonding techniques at Fraunhofer Institute for Reliability and Microintegration IZM, Berlin.

As an underfill material but also to ensure the bonding stability during future process steps, a non-conductive adhesive (NCA), Epotek 303-2FL was manually applied on the substrate before bonding. For degasing purposes, the adhesive was pre-heated at 90 °C for 30 seconds and then chips were bonded using a thermocompression cycle of 60 seconds at 250 °C with ~19 MPa of pressure. It has to be noted that the metal layer, used to protect the electrodes and test pads, in case of the passive implant is used here also as an interface for the bonding process. Therefore, the Ti (100nm) and Al (675 nm) stack of metals appears in this case on top of the electrodes and test pads for protection. On the other hand, it also serves as a substrate for soldering and bonding purposes. Fig. 21 illustrates the flip-chip bonding process steps together with the electrode array structure designed for active implants.

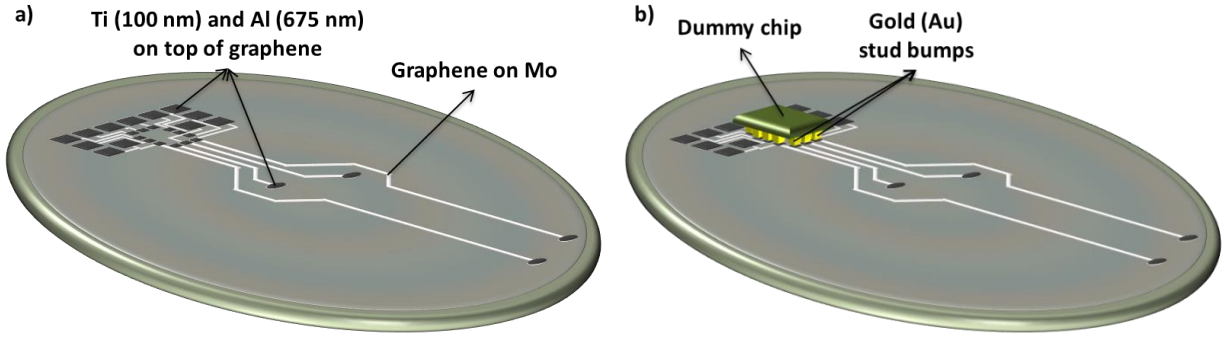

Fig. 21. Dummy chips bonded on the graphene-based substrate using a thermocompression flip-chip bonding technique with NCA. In a), the graphene-based substrate with a metal layer interface. In b), the dummy chip bonded on the substrate.

Once the dummy chips are bonded to the substrate, the first layer of PDMS encapsulation can be spin-coated on top and all the other process steps from the development of the passive implant can be followed. In Fig. 22, the final representation for the active device is illustrated.

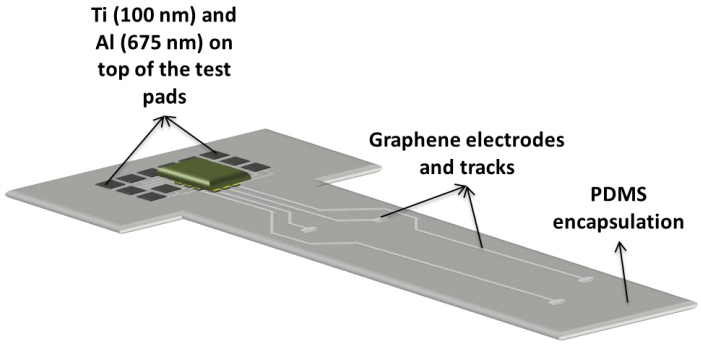

Fig. 22. Final active implant structure after being cut out from the Si wafer.

In Fig. 23, a cross-section of the most important process steps required to develop an active implant from the previously described passive structure is presented.

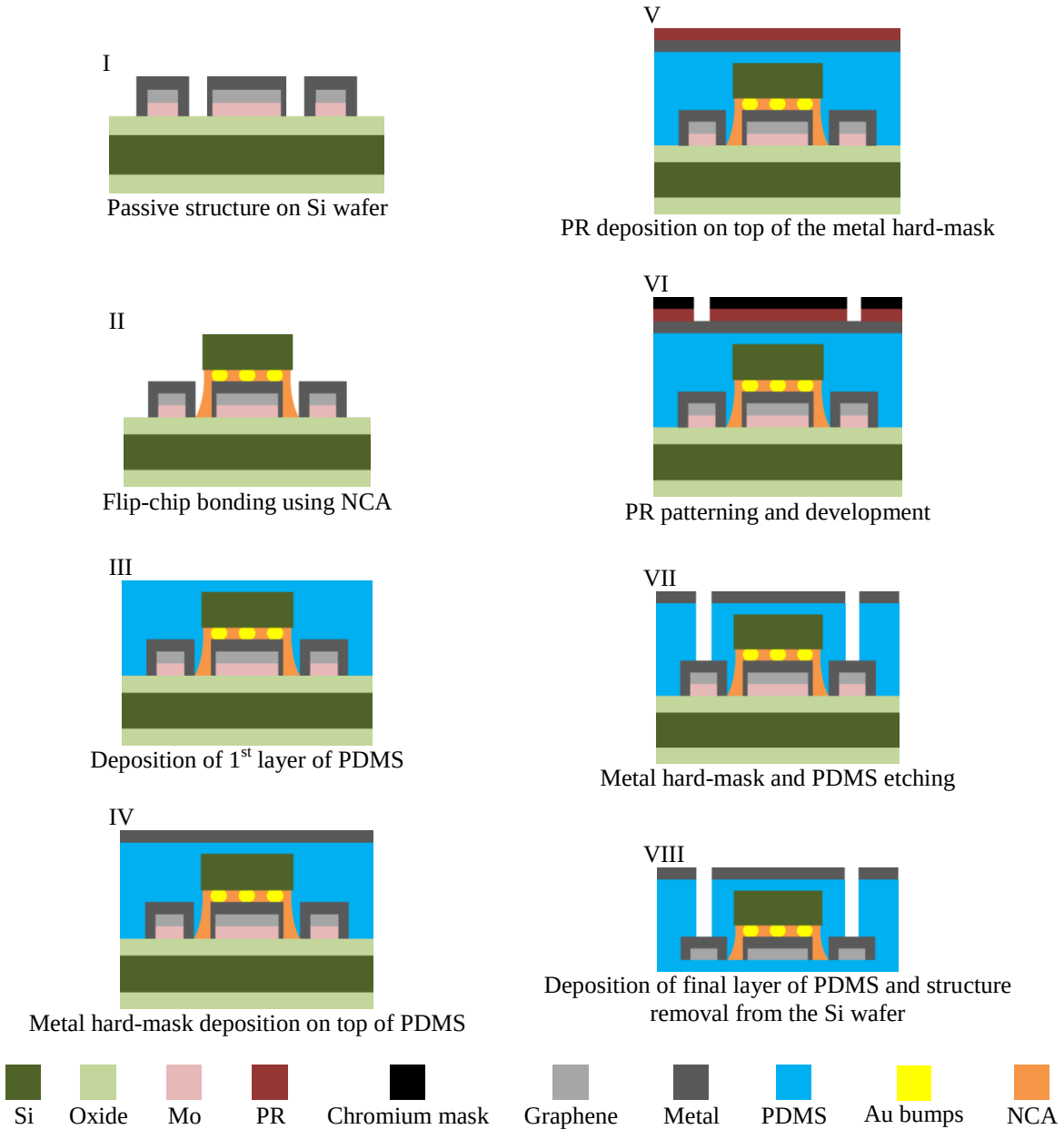

Fig. 23. Process flow for the development of graphene-based active structures on a Si wafer.

3. 2. 1. Fabrication of dedicated test (dummy) chips

For this project, the dedicated dummy chips used in the evaluation of the flip-chip bonding process were also fabricated. The starting material consists of Si wafers with different thicknesses (300 µm and 500 µm) to investigate how this aspect affects the uniformity of the encapsulation layer. Next, the wafers are oxidized, using a wet oxidation process at 1000 °C for about 42 minutes such that later the metal layer can be deposited and patterned on top. The final thickness of the oxide layer is ~300nm, as shown in Fig. 24.

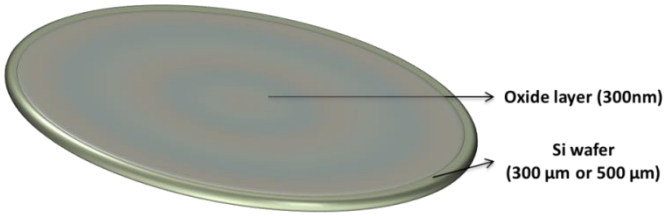

Fig. 24. Frontside wet oxidation (300 nm) deposition on a 4-inch Si wafer with a thickness of either 300 µm or 500 µm.

Next, the metal layer that will define the interconnections present inside the dummy chips is sputtered at 350 °C, using Trikon Σigma tool and later patterned using a set of photolithographic steps. The metal used in this case is Al with 1% of Si and its final thickness will be 1475 nm. To define the final structure of the metal layer, 2.1 µm of positive PR were spin-coated on top, baked at 95°C using the EVG120 Coater-Developer tool, exposed to UV light using the BE2325-IC-METAL bright-field chromium mask and, finally, developed. The metal layer that is no longer protected by the PR will be etched at 25 °C using Trikon Ωmega tool. The microfabrication process steps, previously described, are illustrated in Fig. 25.

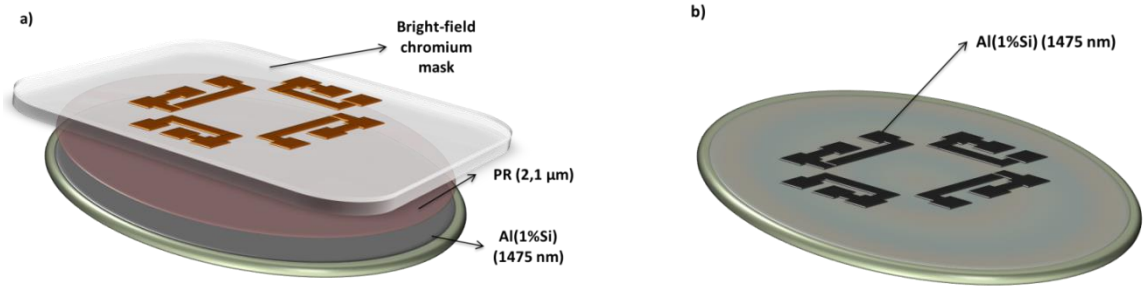

Fig. 25. Metal sputtering and patterning in order to define the dummy chip interconnections. In a), Al(1%Si) (1475 nm) deposition and patterning. In b), the metal layer etched from the unwanted areas.

Having the metallization layer defined on the Si wafer, the final passivation of the dummy chips has to be deposited and all contact openings have to be created such that later, Au stud bumps can be placed on the pads. For the passivation layer, 800 nm of PECVD oxide were deposited at 400 °C and patterned. The thickness of the oxide has been chosen such that it covers properly the metal layer underneath. After deposition, another set of photolithographic steps were employed to define the contact opening areas. To this end, 2.1 µm of positive PR were spin-coated on top, baked at 95°C and exposed to UV light using the BE2325-IC-CO dark-field chromium mask. Finally, the oxide that is no longer protected by the PR will be etched using Drytek 384T plasma etcher tool. A visual representation of the aforementioned process steps is illustrated in Fig. 26.

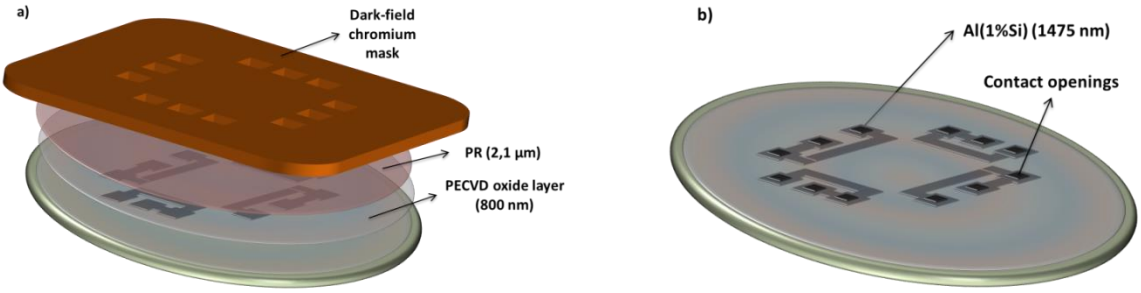

Fig. 26. Creation of contact openings. In a), oxide deposition and patterning. In b), the oxide layer etched from the unwanted areas.

Finally, before dicing the dummy chips from the Si wafer, stud bumps have to be created such that later, flip-chip bonding processes can be employed. To do so, a manual wire-bonder was used and the bumps were created

using a gold-palladium (AuPd) wire with a diameter of 25 µm, while the substrate was constantly kept at 60 °C. For each contact opening, one AuPd stud bump was placed, as shown in Fig. 27.

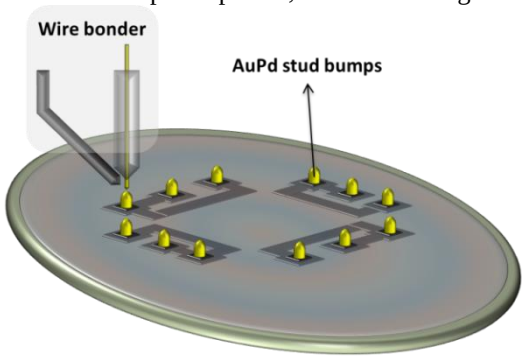

Fig. 27. Manual creation of the AuPd stud bumps using a wire bonder tool.

In Fig. 28, the cross-section of the aforementioned process steps needed to create the dummy chips is illustrated.

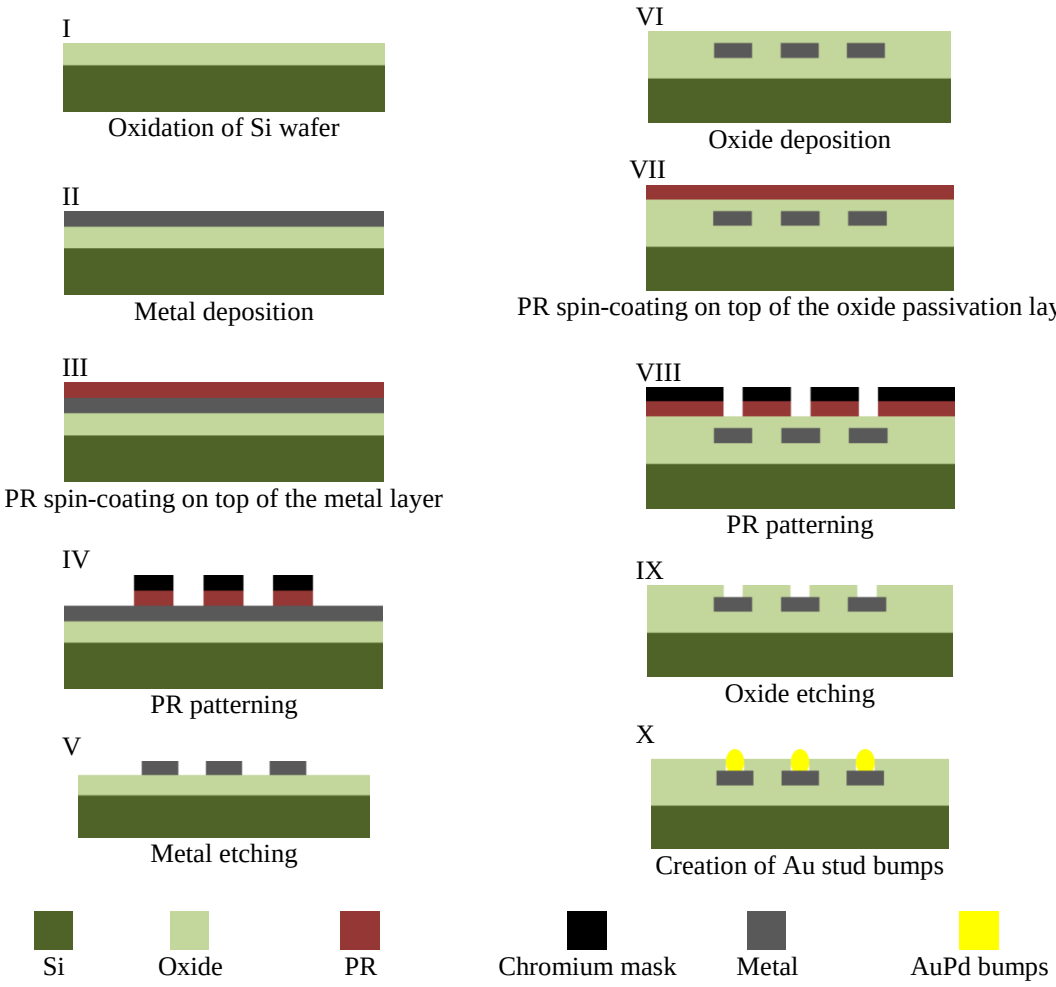

Fig. 28. Process flow for the development of dummy chips on a Si wafer.

3. 3. Characterization methods for the spinal cord implants

The development of spinal cord implants is defined, not only by the microfabrication process involved but also by the characterization of the materials used and of the final structure. Therefore, several evaluation methods have been employed throughout the process and will be discussed in the following sections of this subchapter.

3. 3. 1. Raman spectroscopy

For this project, one of the most important materials is graphene as it is being used to develop the transparent, non-metallic array of electrodes. Taking into account that the microfabrication process is relatively extensive and it involves many post-processing steps after graphene synthesis, it is of great importance to evaluate the graphene layer after each critical step. To this end, Raman spectroscopy was employed. This method can provide, among others, information about the presence of graphene, number of layers and number of defects present on the grown layer.

For graphene and graphitic materials, three peaks are of great importance and apart from indicating the presence of graphene on different catalysts, each of them provides insight into the characteristics of the material. These three peaks are: the D peak, present at ~1330 cm^{-1}, G peak at ~1590 cm^{-1} and 2D peak at ~2660 cm^{-1} respectively. The D peak or disorder-induced band, indicates if defects in the graphene layers are present. As the presence of defects in carbon-based materials leads to pronounced phenomena, Raman spectroscopy is thus a very sensitive method for the characterization of graphene structures [59]. In order to estimate the number of defects, the ratio between the intensity of the D peak and G peak (I_D/I_G) is calculated and evaluated (the greater the ratio, the more defects are present in the synthesized graphene layer). These defects, generally originate from the growth process [43].

The second peak observed on a Raman spectrum for graphene is the G peak which is strongly related to the C-C bonds forming the graphene lattice. Although graphene is considered to be a 2D, flat material, it usually consists of more than one layer and thus modifications in the C-C bonds might appear. The G band is usually very sensitive to modifications due to strain, caused either by the interaction of graphene with the substrate material or with other graphene layers and therefore it can be used to determine any modification that might appear on the relatively flat graphene structure that is being evaluated [59].

The last peak appearing on the spectra is the 2D peak, representing an overtone and being highly related to the number of graphene layers present in the structure. In order to estimate if there is a graphene monolayer or a stack of layers present, the ratio between the intensity of 2D and G peak (I_{2D}/I_G) has to be evaluated. This ratio is generally greater than 1 for a monolayer graphene and less than one for multilayers [60]. From the width of the 2D peak it can also be estimated, up to 4, 5, how many graphene layers are present [59].

3. 3. 2. Electrical measurements

In order to evaluate the conductivity of graphene but also the flip-chip bonding process on graphene-based substrates, electrical measurements were employed. For graphene evaluation, 2-point measurements were used and the structures were evaluated after different fabrication steps. First, the conductivity of graphene was measured, after graphene growth. Since in this case, the catalyst underneath graphene is still present, a different value, compared to a graphene-only track will eventually be observed. Moreover, since for 2-point measurements, there is less control over the contact resistances, originating from the probes, the accuracy of the result may be influenced.

For the evaluation of the flip-chip bonding processes, however, 4-point measurements were also employed, in order to reduce the influence of the contact resistances over the measurement but also because individual evaluation of the stud bumps had to be conducted. The daisy chain used for this evaluation is presented in Fig. 29.

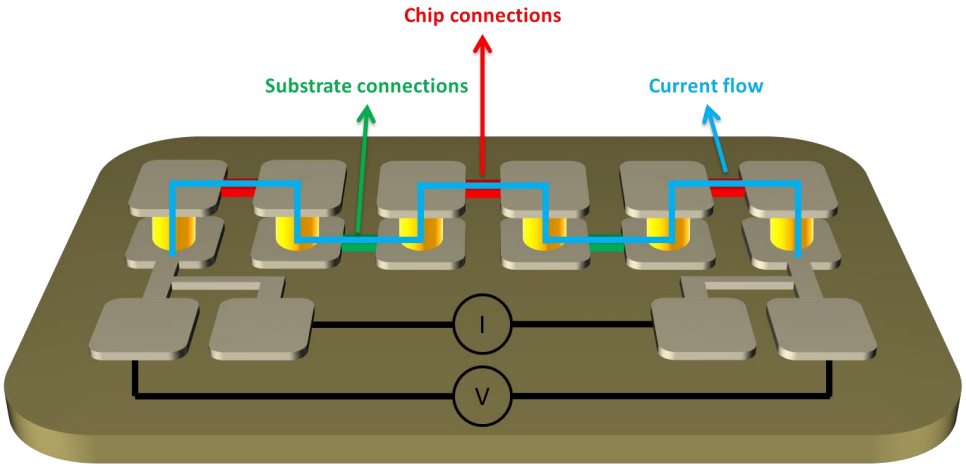

Fig. 29. "Daisy-chain" topology together with a four-point evaluation of it.

3. 3. 3. Optical transmittance

Estimating the number of graphene layers is of great importance especially for this application because the transparency of the final implant is a critical aspect when it comes to *in-vivo* validation of optogenetic compatible implants. Since from the Raman spectra, an exact number cannot be calculated, optical transmittance measurements have to be employed. This evaluation consists of passing light with different wavelengths, usually from the visible spectrum (400 nm to 700 nm), through the sample and measuring the level of transmittance rate ($(\%\boldsymbol{T_{measured}}$). From that, the level of absorbance rate ($(\%\boldsymbol{A_{measured}}$) can be calculated. For monolayer graphene structures, it has been reported in the literature that the absorbance rate is 2.3 % ($\%\boldsymbol{A_{monolayer}}$) [34]. Having these specifications, the exact number of graphene layers can be calculated using the formula below:

$$N_{layer} = \frac{\%A_{measured}}{\%A_{monolayer}} \qquad (1)$$

3. 3. 4. Bending tests

The mechanical stability of the fabricated spinal cord implants is of great importance due to the implantation site for the prototypes during *in-vivo* experiments. Since the implants are potentially subjected to different degrees and types of movements, bending tests have to be performed in order to evaluate which are the potential failure causes for the structures. To this end, metal bars with diameters ranging from 3 mm to 8 mm were used. The implants were electrically measured before the evaluation and after each bending procedure and the results were compared. The measurements were performed using a two-point measurement setup. The voltage imposed ranged from -5 V to 5 V and the current through the tracks was measured. From that, the resistance was calculated and compared to the control value.

3. 3. 5. Electrochemical impedance spectroscopy (EIS)

For the graphene electrodes, separate evaluation methods have to be employed in order to characterize the behaviour of the electrodes under specific conditions but also to investigate their capabilities in terms of the charge that can be stored and safely delivered to the tissue. To this end, first, electrochemical impedance spectroscopy (EIS) was employed. This technique is used to measure the impedance values and phase shift of a system with respect to a specific range of frequencies. To achieve this, the equivalent circuit illustrated in Fig. 30 is used to model the electrical characteristics of the electrode-electrolyte interface, where E_{hc} is the half-cell potential, or the potential that appears when the electrodes are immersed inside the saline solution without any voltage applied across them. This re-arrangement of charges across the interface forms a capacitive double layer between the saline surrounding the metal and the rest of the solution, thus creating a voltage difference. R_{el} and C_{el} are the contributions of the electrode and R_s is the resistance of the electrolyte. Usually the measurements are performed using 3 electrodes. The first one, the working electrode or the electrode under measurement, second, the return electrode (Pt electrode), relatively big in size, therefore presenting very low impedance values and thus not being the dominant one during the measurements and also the reference electrode, silver/silver chloride, (Ag/AgCl).

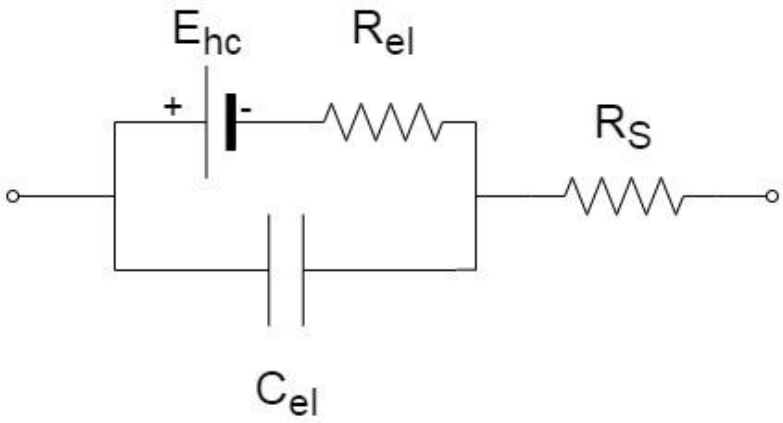

Fig. 30. Equivalent electric circuit for modelling the electrode-electrolyte interface during an EIS measurement. Modified based on [61].

During the measurement, a small AC voltage with a frequency that is varied from 1 Hz up to 100 kHz is applied over the electrodes. When enough voltage is applied, current starts flowing between the electrodes through the electrolyte interface. Two different reactions might occur. A Faradaic reaction, illustrated by the top branch in Fig. 30 and a non-Faradaic reaction, illustrated by C_{el} in the same figure. In a Faradaic reaction, irreversible processes such as oxidation and reduction occur, thus creating some products that either stay on the electrode surface or diffuse into the electrolyte. In any case, through Faradaic reactions, damage is being made. On the other hand, through non-Faradaic reactions, no electrons are transferred and the charge distribution can be reversed by reversing the direction of the current flow [61]. Bode plots are used to plot the impedance and phase behaviour over frequency. A typical Bode plot for such measurements consists of a capacitive behaviour at low frequencies and a resistive one at high frequencies.

3. 3. 6. Cyclic voltammetry (CV)

Cyclic voltammetry (CV) is the second method used to characterize the electrodes. This method is used to obtain information about the reduction-oxidation processes that might occur at the electrode site and that are considered irreversible electrochemical reactions that lead to damage of the electrode. After performing a CV measurement, the charge storage capacity (CSC) can also be calculated by integrating the area between the two CV lines.

Generally, the test is performed using a 3-electrode setup, one the working electrode, or the electrode under test, one the reference (Ag/AgCl) and a third as a return electrode (Pt). The measurement is done by sweeping the voltage applied to the working electrode while the current is measured between the working and return electrode. The voltage window present between the current peaks that indicate the presence of either reduction or oxidation processes is considered to be the water window, or the voltage range that could be applied without inducing irreversible reactions. In Fig. 31, a typical voltage sweep together with a cyclic voltammogram are illustrated [62].

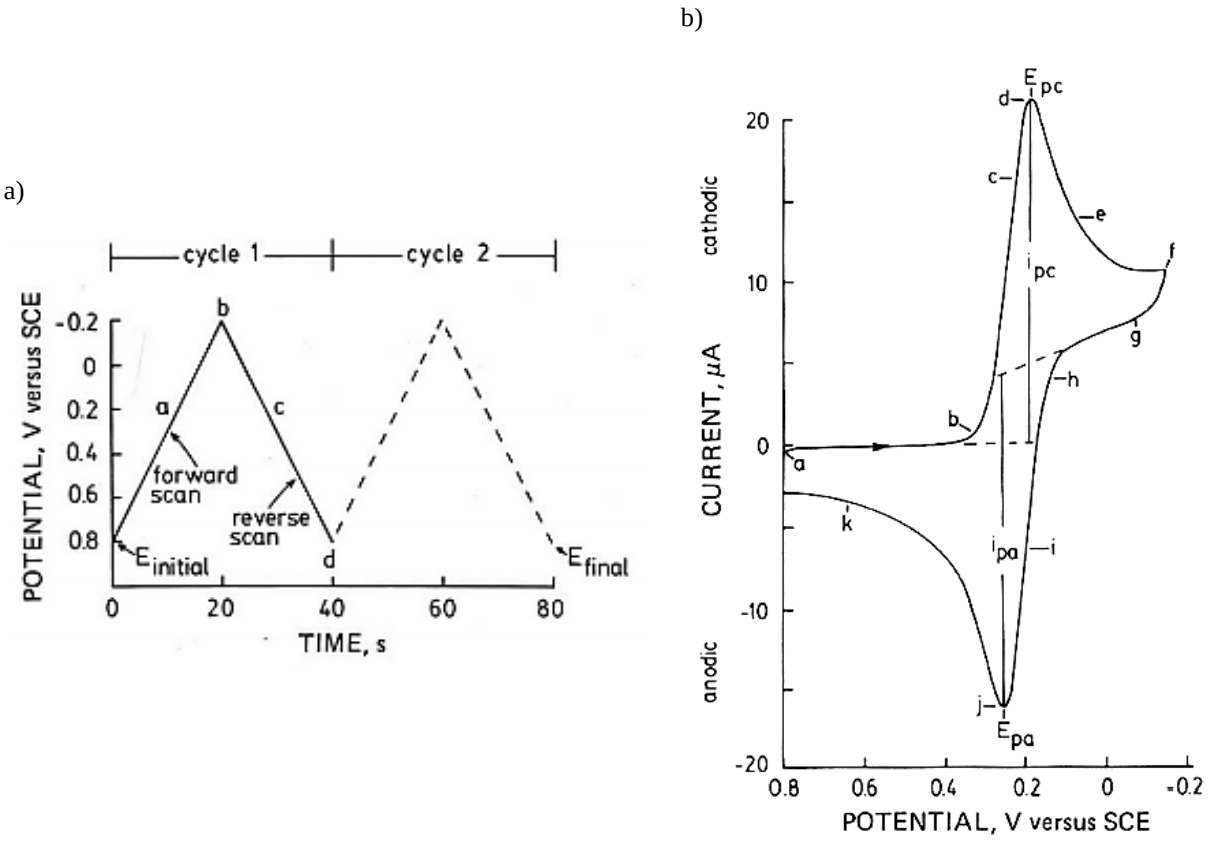

Fig. 31. Typical voltage sweep diagram a), and the associated current plot b), for a CV measurement [62].

3. 4. Design of photolithographic masks

The purpose of this project is to develop a passive, as well as an active graphene-based flexible implant for spinal cord applications that could further be tested both *in-vitro* and *in-vivo*. To develop such implants, several masks have to be designed taking into account microfabrication limitations but also constraints originating from the type of subjects and implantation site for the *in-vivo* experiments. Apart from the spinal cord implants, a passive structure for dorsal root ganglia (DRG) applications has also been developed due to the great interest shown by the neuroscience community in understanding the implication of DRG in the locomotion system. Moreover, for the external characterization of the implants, special structures have been used for bending tests and optical transmittance measurements, structures previously developed by G. K. Wardhana [63]. Therefore, the following sections of the current subchapter will describe in detail the design considerations for each photolithographic mask needed throughout the process.

3. 4. 1. Photolithographic masks used for the development of graphene-based passive spinal cord implants

Regardless of the type of implant, spinal cord applications require specific dimensions that are generally dictated by the type of subjects used for the *in-vivo* experiments. For the current project, these experiments will be conducted in collaboration with the Neuroscience Department of Erasmus Medical Center (ErasmusMC), in The Netherlands, where they use mice as subjects.

The implantation site will be the cavity between the dura mater and the spine, also known as the epidural space (Fig. 32). The gross anatomy of a mouse spine consists of 34 segments: 8 cervical (C1-C8), 13 thoracic (T1-T13), 6 lumbar (L1-L6) and 4 sacral (S1-S4). From these, for spinal cord applications, the most interesting areas to be investigated are the spinal segments located under the vertebral segments T10 to L2.

From the measurements performed in a few subjects at ErasmusMC, the following dimensions have been defined:

- The effective length area of the implant, within which the electrodes and test pads will be placed, should not exceed 1.5 cm, taking into account also some safety margins due to the differences that might appear among subjects;
- The width of the implanted area should be no more than 2 mm due to the limited epidural space available. Note that the area comprising the test pads will not be implanted inside the epidural space, but will be resting on top of a vertebra. Therefore, its width can be up to 6 mm;
- The thickness of the implant should be ~100 µm.

The implantation method used by the neuroscientists consists of several steps. First, a cavity is opened in the spinal vertebrae, to create space for the implant. Next, the implant is gently pulled from its end and placed over the area of interest, as illustrated in Fig. 32. Therefore, at the end of the implant, a dedicated area should be left for implantation purposes. Thus, the final length of the implant will be no more than 2 cm.

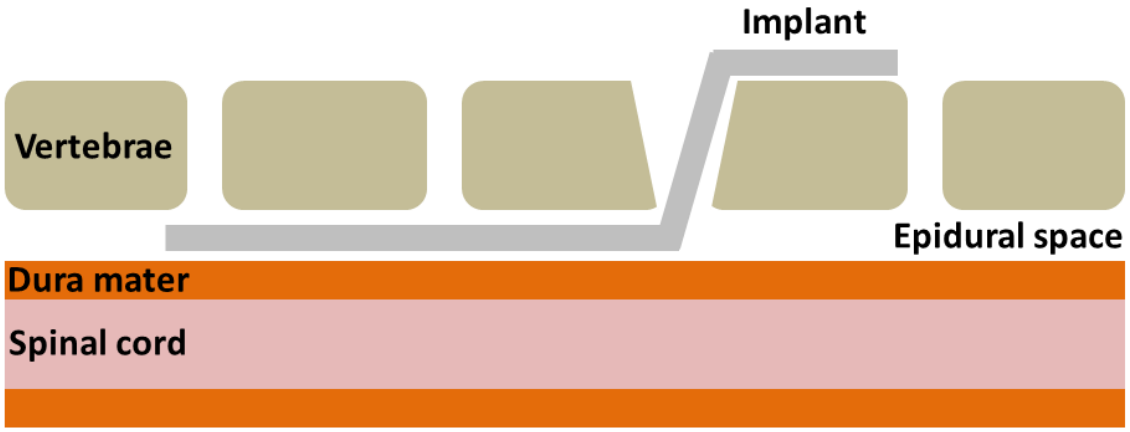

Fig. 32. Schematic representation of the implantation procedure.

Due to the restrictions in terms of available area, a large number of electrodes per implant could not be integrated. Safety margins had to be left at the edges of the implant such that the polymeric layers could encapsulate properly the structures. However, the design has been developed such that it can allow for stimulation and/ or recording of/ from two different spinal segments. Thus, each implant consists of 4 electrodes,

2 for each area of interest, spaced such that they can be in contact with two different spinal segments at the same time.

The table below synthesizes the most important dimensions that had to be taken into account while designing the passive spinal cord implants. It should be noted that some dimensions for the microfabricated implant are slightly bigger than the dimensions received from ErasmusMC. This is due to the fact that some safety margins had to be considered in case of misalignment of masks during the fabrication process but also to be able to cut out the implants from the Si wafer at the end of the process.

Table 2. Dimensions used in the design of a passive spinal cord implant for mice subjects.

Dimensions for a passive spinal cord implant		
	Dimensions measured in mice subjects	**Dimensions of the fabricated implant**
Length of implant	-	2 cm
Width for implanted area	2 mm	2.2 mm
Width for the area comprised of test pads	5-6 mm	6.2 mm
Thickness	100 µm	100 µm
Number of electrodes	-	4
Distance between two areas of electrodes	-	4-5 mm
Electrode opening diameter	-	340 µm

The design of the photolithographic masks was developed using the L-Edit program and for each type of implant four masks had to be created, each of them representing a photolithography process step.

The first mask (BE2325-GRAPHENE), shown in Fig. 33, defines the graphene passive structure for the electrodes, tracks and test pads. Note that where the electrodes and test pads are, a holey graphene layer is present in order to promote better adhesion of the metal layer that will be applied on top of these areas.

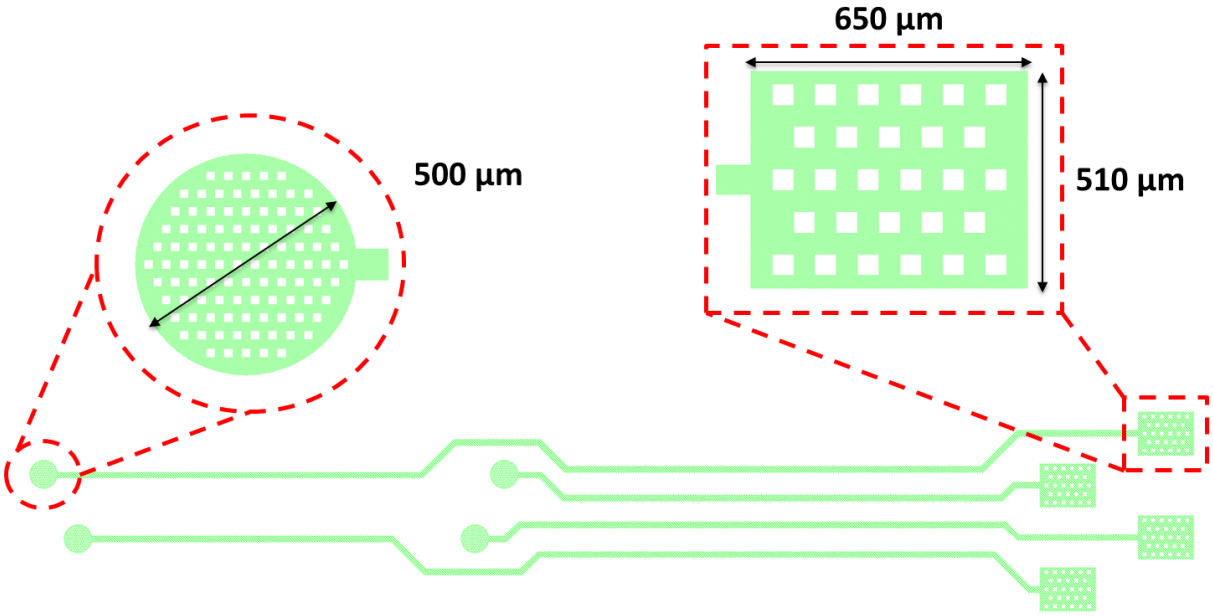

Fig. 33. BE2325-GRAPHENE mask for defining the electrodes, tracks and test pads of a passive spinal cord implant.

The second mask (BE2325-METAL), shown in Fig. 34 represents the metal layer that will be deposited and patterned such that the electrodes and test pads are protected during later process steps. Moreover, the metal present on the test pads will serve as a substrate for later soldering processes.

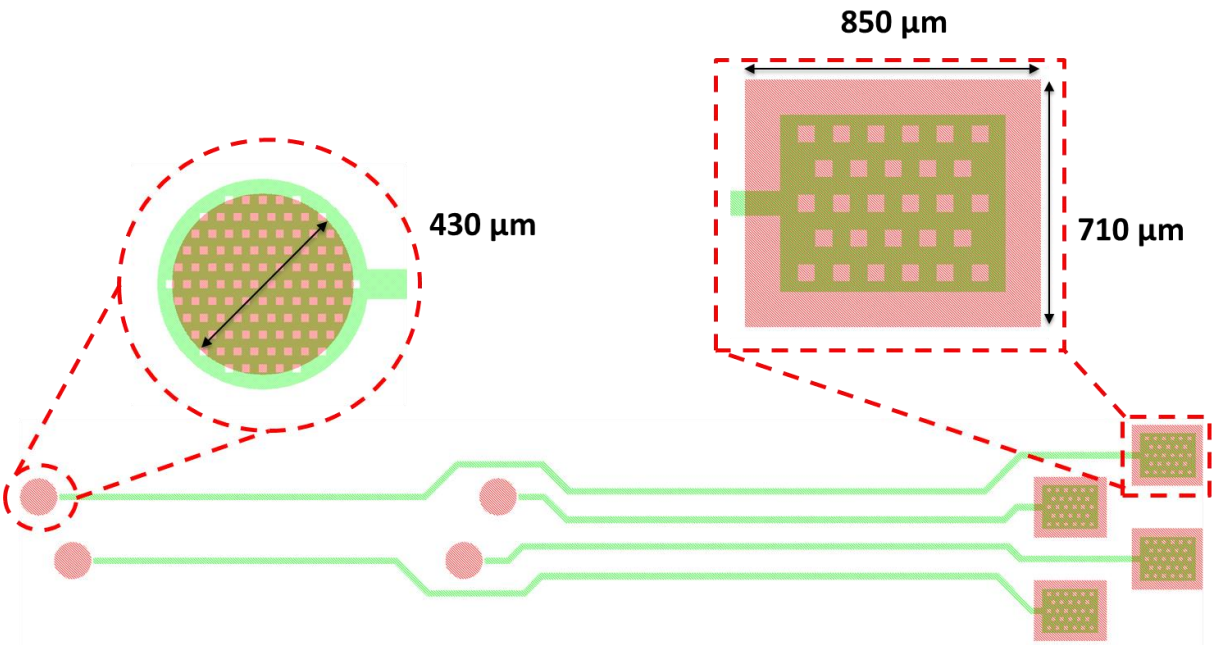

Fig. 34. BE2325-METAL mask for defining the graphene areas that need to be protected in later microfabrication process steps.

It should be noted that for adhesion purposes, on the test pads, the metal layer is slightly bigger than the graphene underneath. For the electrodes, the adhesion needed to keep the metal on top of graphene until the microfabrication process is completed, is ensured by the holey graphene structure. Therefore, the metal layer on top is smaller such that it can easily be removed from graphene when the passive implant is fully developed. Moreover, once the metal is being removed, the graphene electrode area should not be fully exposed but protected, at its outermost ring, by the polymer on top.

The third mask (BE2325-PDMS), illustrated in Fig. 35 will define the openings in the polymeric encapsulation layer of the implant.

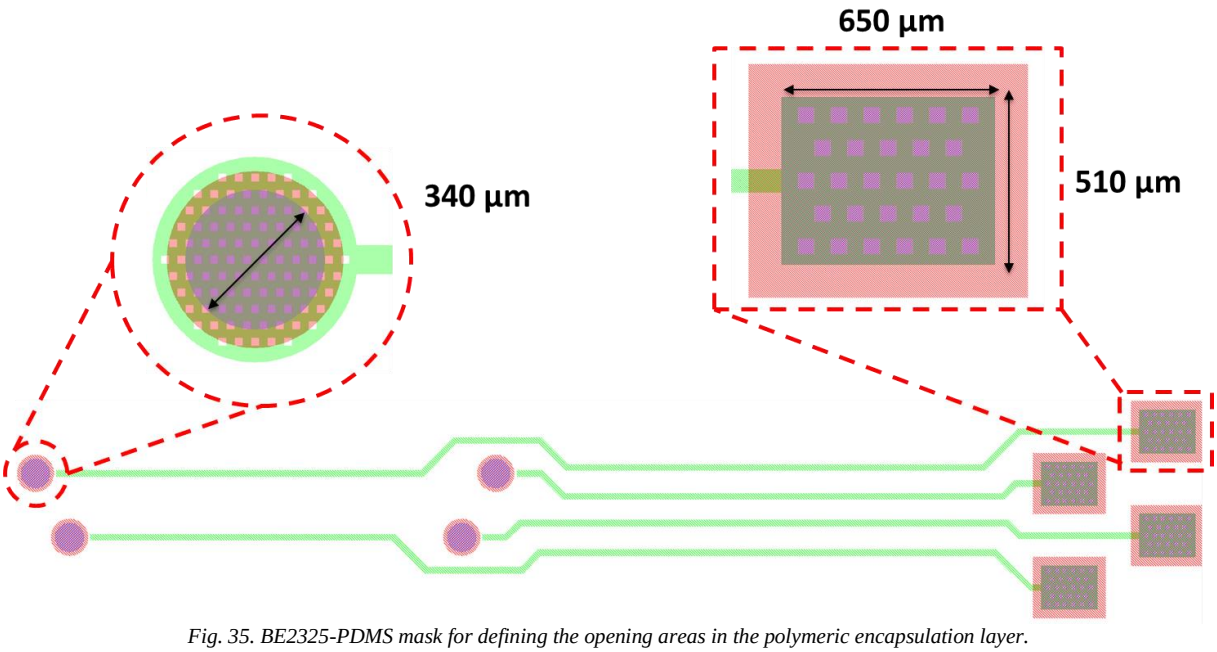

Fig. 35. BE2325-PDMS mask for defining the opening areas in the polymeric encapsulation layer.

The openings in the polymeric encapsulation layer are represented in purple, as shown in the image above. For the test pads, the dimensions of the openings are the same as for the graphene pads, completely covered by the metal layer. However, for the electrodes, the openings are smaller than the metal to avoid damaging the graphene layer in case of misalignment of the mask during the lithography steps.

The last mask (BE2325-DRIE), shown in Fig. 36, will be used to pattern the backside of the wafer in such a way that the complete implant area can be suspended and later released from the original rigid substrate.

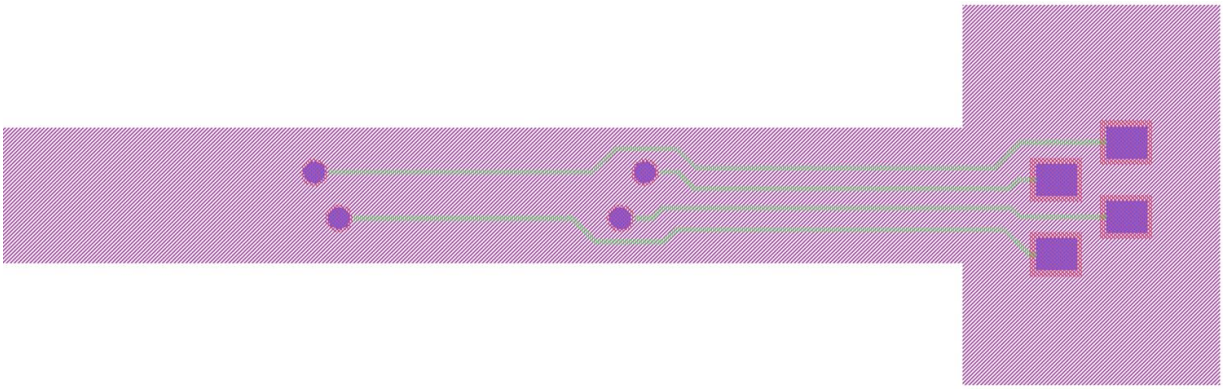

Fig. 36. BE2325-DRIE mask used to pattern the backside of the wafer for further release of the passive spinal cord implant.

3. 4. 2. Photolithographic masks used for the development of graphene-based active spinal cord implants

For the development of active implants, several designs have been investigated. First, a dedicated area for the chips, comprising the active components, had to be designed. Because of the limited epidural space available, but also to avoid compression and extreme bending of the chips, it has been decided to design their location close to the test pads. In this way, the chips, together with the test pads will be resting on top of a rigid vertebra. Second, in order to evaluate the quality of the bonding process, the number of test pads had to be increased. Therefore, for each active implant, 12 test pads will be present. Moreover, dedicated dummy chips, without any active components but with a specific interconnection topology, also known as a "daisy-chain", explained in a previous section of this thesis, had to be designed and fabricated.

Similar to the passive implants, for the development of active, graphene-based structures, four photolithographic masks were used, taking into account the same dimensions listed in Table 2, for a passive implant. One mask was used for defining the graphene layer (BE2325-GRAPHENE), one for patterning the metal layer on top of graphene (BE2325-METAL), one for creating the openings in the polymeric encapsulation (BE2325-PDMS) and one for releasing the complete structure from the backside of the wafer (BE2325-DRIE).

The electrode array structure for the active implant is different from the one used for the passive devices due to the need of creating sufficient space for bonding the ASICs and also developing more test pads that will allow for complete characterization of the bonding process and of the final active device.

One of the challenges of the current project is the integration of active components with the graphene-based structures. For this, flip-chip bonding techniques will be employed. In order to improve the adhesion of metal to graphene but also to investigate how different microfabrication processes influence the final measurement results of the devices, different designs, particularly for the area where the chips will be bonded, have been developed and later evaluated. For the electrodes, no changes have been made in this design phase.

Two major categories of active implants have been envisioned. The first category, shown in Fig. 37, presents graphene and metal layers for the dedicated chip area while for the connections to the test pads and the test pads themselves are metal-based only. The second category, illustrated in Fig. 38, shows that for the dedicated chip area and connections to the test pads, only graphene has been used. The test pads in this case are comprised of both graphene and metal layers. Hence, the resistivity results can be evaluated and correlated to the microfabrication processes. Apart from that, for each of the two aforementioned categories, two different types of graphene layers were designed. One comprises of a holey graphene structure, while in the second case, the graphene layer is not patterned. This allows for proper evaluation of the adhesion aspect. Moreover, it has to be noted that for the second category of active implants, the bonding process will be performed only on graphene substrates. Therefore, no metal layer will be present on top.

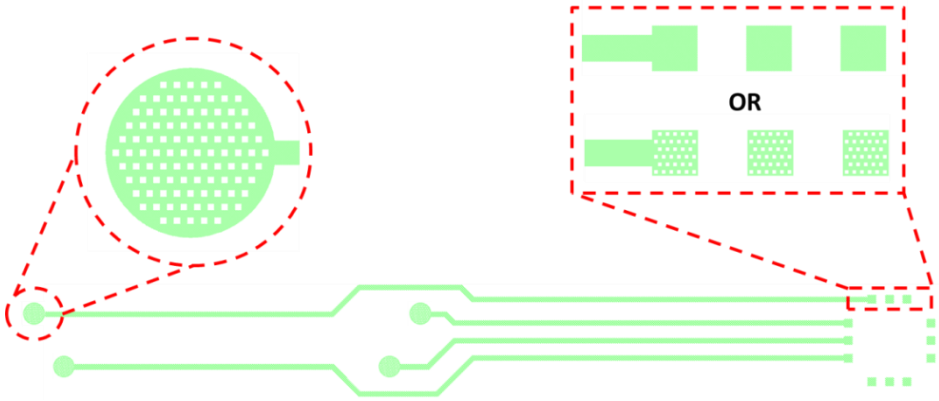

BE2325-GRAPHENE mask for defining the electrodes, tracks and location of the dummy chips for the active spinal cord implant.

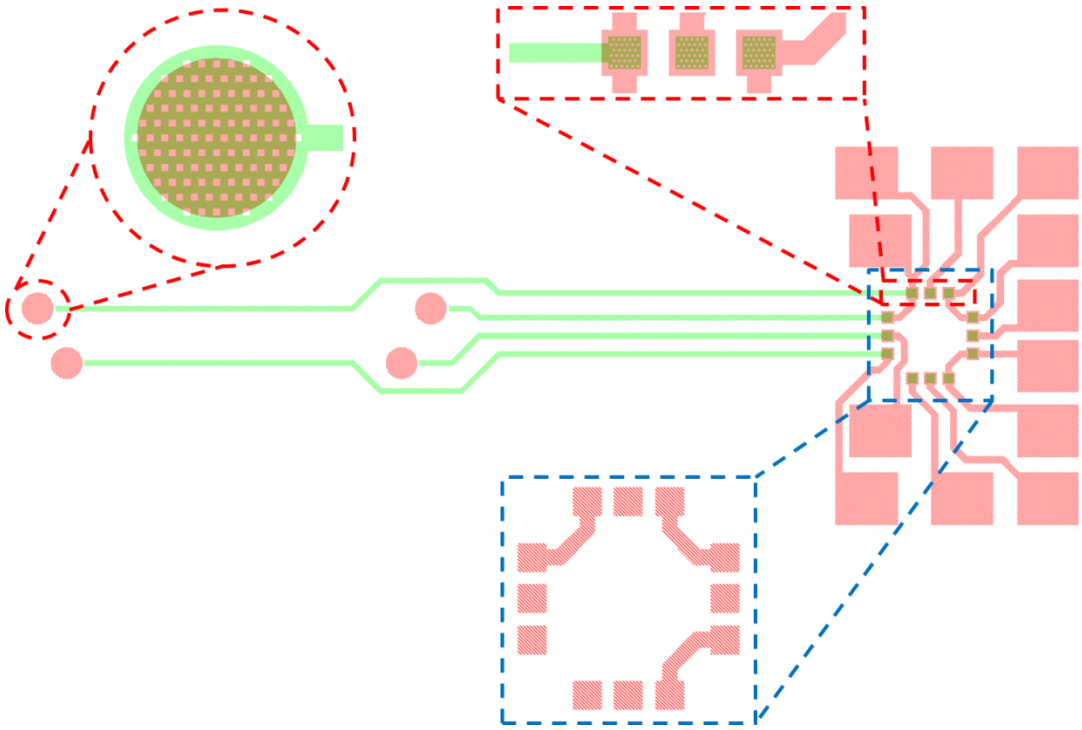

BE2325-METAL mask for defining the test pads and the graphene areas that need to be protected in later microfabrication process steps.

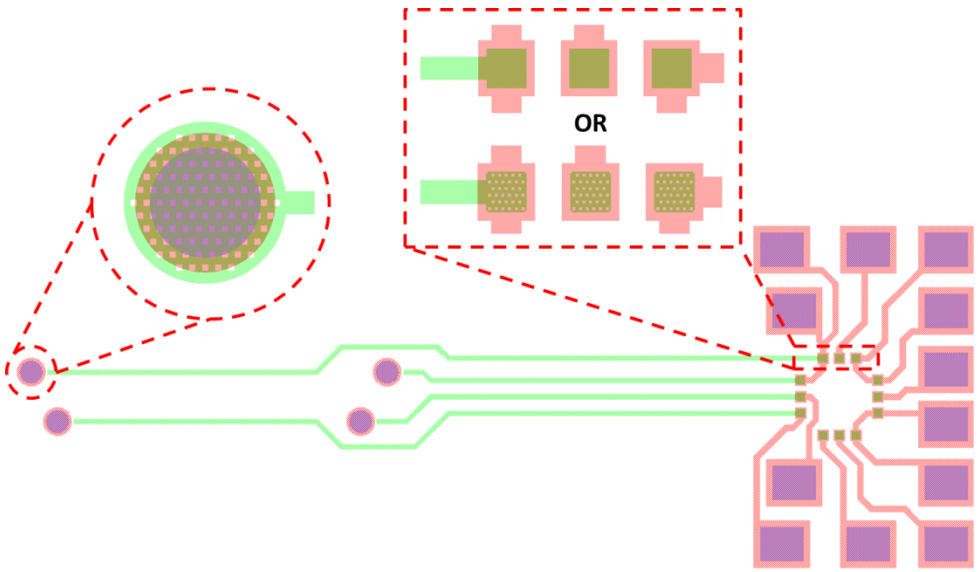

BE2325-PDMS mask for defining the opening areas in the polymeric encapsulation layer only for the electrodes and test pads.

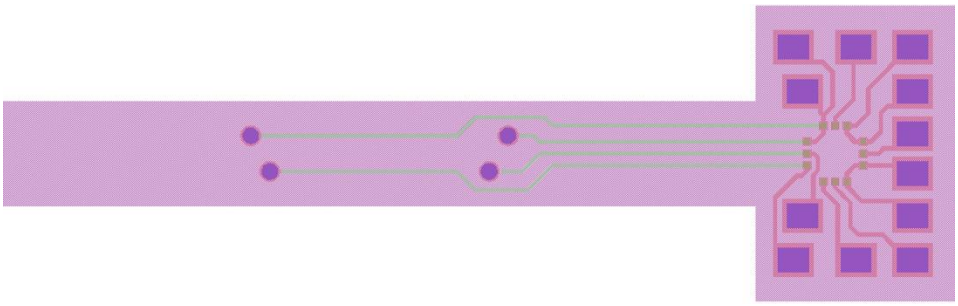

BE2325-DRIE mask used to pattern the backside of the wafer for further release of the active spinal cord implant.

Fig. 37. First category of active spinal cord implants with metal test pads and connections to the graphene layer. The two different types of graphene layers are illustrated.

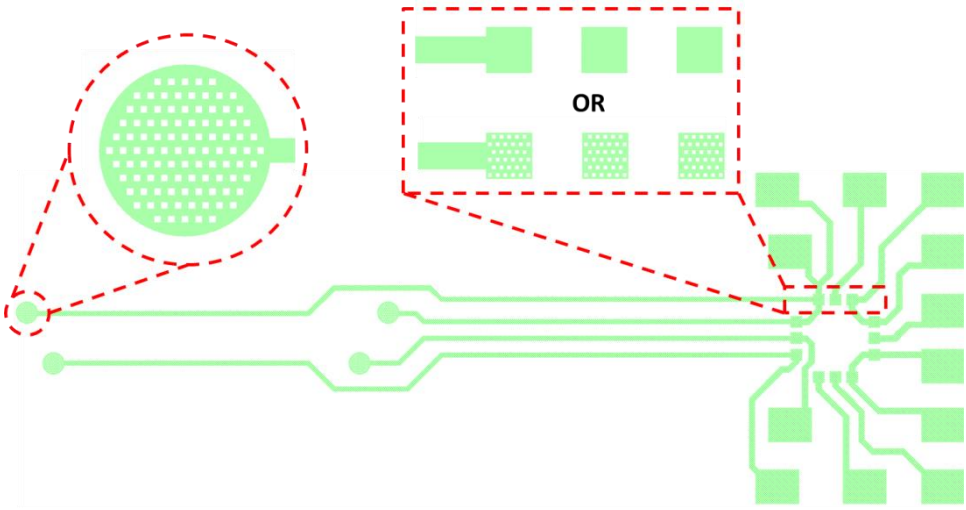

BE2325-GRAPHENE mask for defining the electrodes, tracks, test pads and location of the dummy chips for the active spinal cord implant.

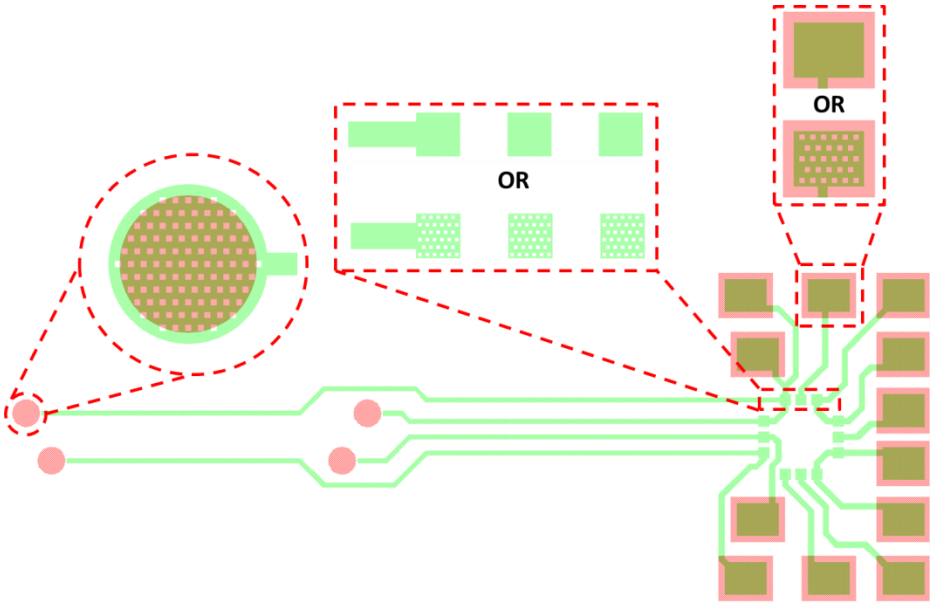

BE2325-METAL mask for the graphene areas that need to be protected in later microfabrication process steps.

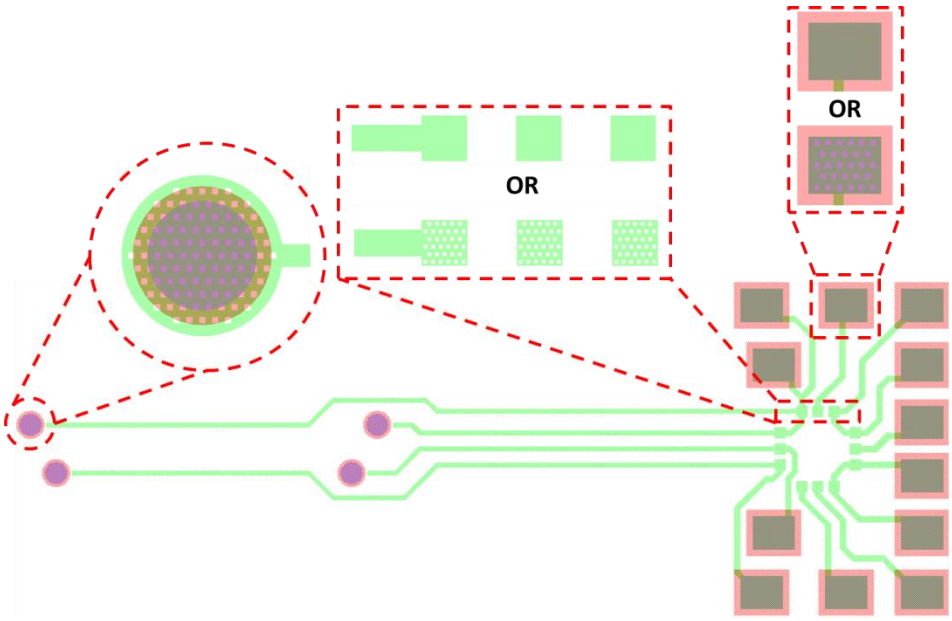

BE2325-PDMS mask for defining the opening areas in the polymeric encapsulation layer only for the electrodes and test pads.

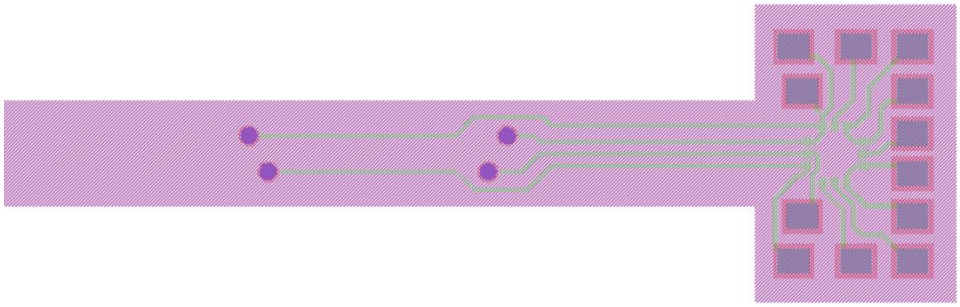

BE2325-DRIE mask used to pattern the backside of the wafer for further release of the implant.

Fig. 38. Second category of active spinal cord implants with the test pads of both metal and graphene. The two different types of graphene layers are illustrated.

As mentioned previously, to evaluate the integration aspect, namely the flip-chip bonding process, dummy chips had to be designed and fabricated. The design, illustrated Fig. 39, had to match the substrate such that a "daisy-chain" could be created and measurements, later, performed. Note that when the chips are flip-chip bonded to the substrate, the depicted design would be mirrored.

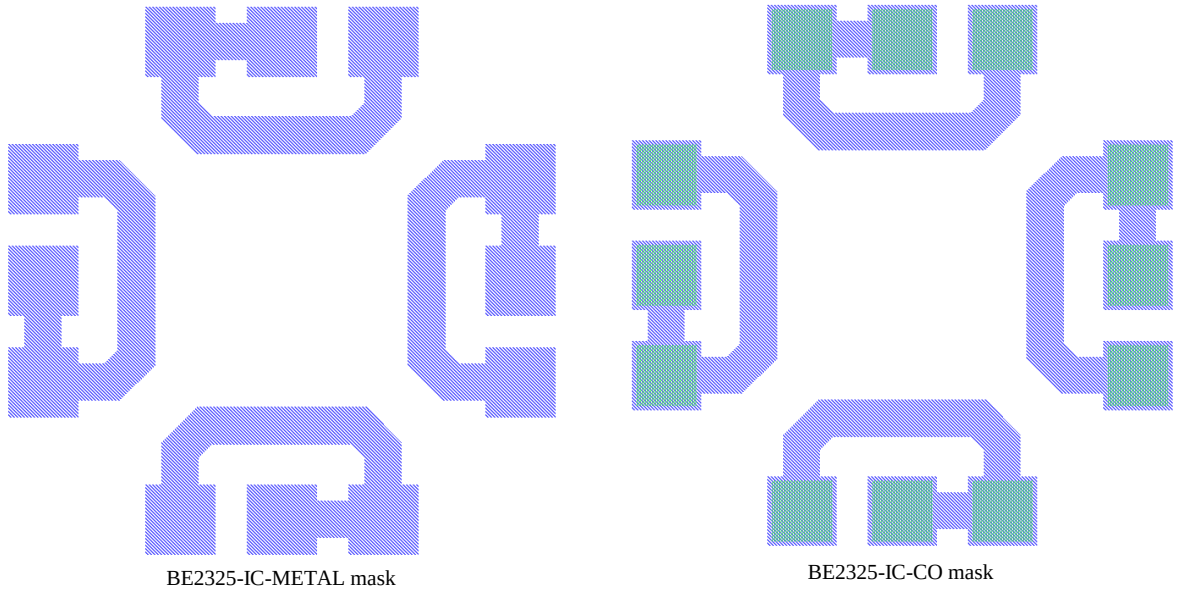

Fig. 39. Dummy chip mask design. On the left, the mask used to pattern the metal layer. On the right, the mask used to create the contact openings in the passivation layer.

3. 4. 3. Photolithographic masks used for the development of graphene-based passive DRG implants

For the first DRG experiments, only a passive implant was developed. Later, if an active implant is needed, the masks can be changed accordingly. Compared to spinal cord implants designed for *in-vivo* experiments in mice, the dimensions of a DRG implant are even smaller. The most critical dimensions that had to be considered in this case, are listed in Table 3.

Table 3. Dimensions used in the design of a passive DRG implant for mice subjects.

Dimensions for a passive DRG implant		
	Dimensions measured in mice subjects	**Dimensions of the fabricated implant**
Length	-	8.5 mm
Width for implanted area	0.6-0.8 mm	0.85 mm
Width for the area comprised of test pads	-	4 mm
Thickness	100 µm	100 µm
Number of electrodes	-	5
Electrode opening diameter	-	130 µm

To develop the DRG implants, similar masks as for the passive and active spinal cord implants were used. The first mask (BE2325-GRAPHENE) will be used during the first microfabrication process steps to define the final graphene structure. It should be noted that for adhesion purposes, at the electrodes and test pads sites, a holey graphene layer was used, as illustrated in Fig. 40.

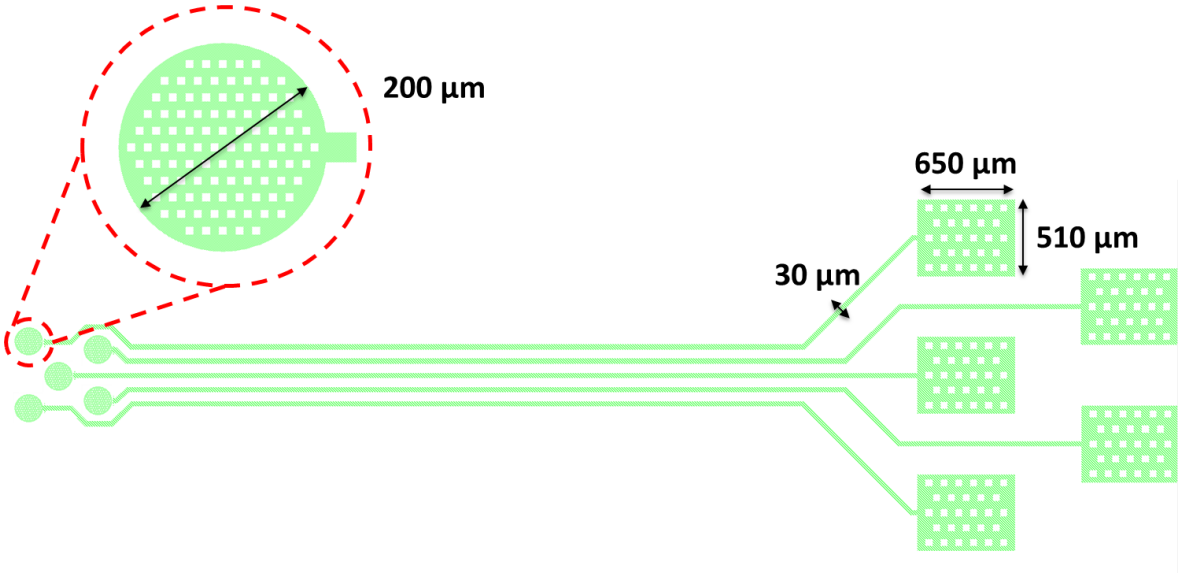

Fig. 40. BE2325-GRAPHENE mask for defining the electrodes, tracks and test pads of a passive DRG implant.

The second mask (BE2325-METAL) is used to pattern the metal layer on top of graphene, as shown in Fig. 41.

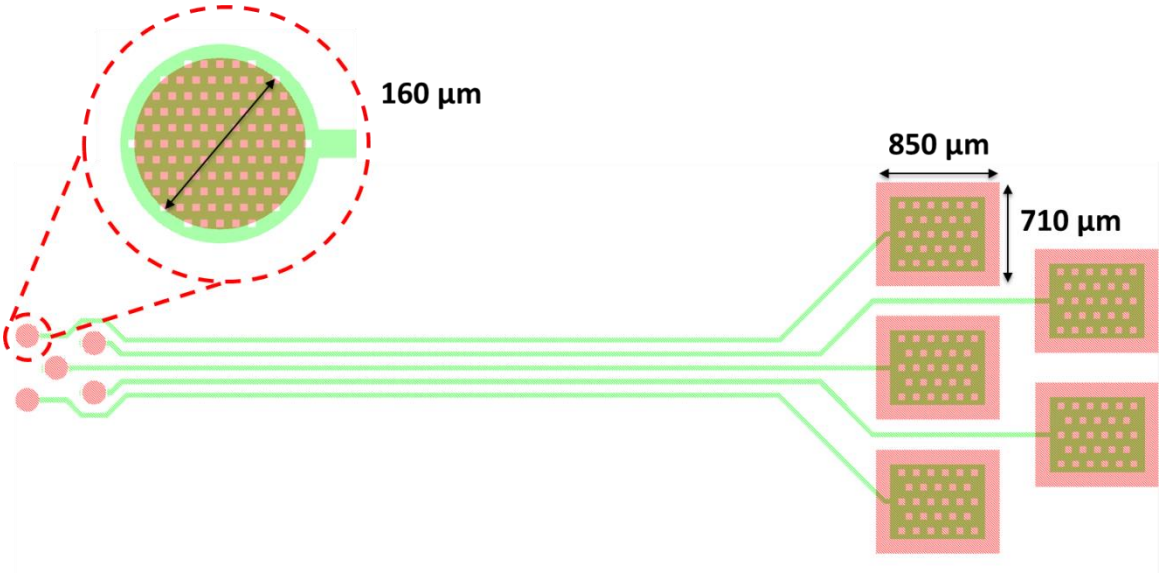

Fig. 41. BE2325-METAL mask for defining the graphene areas that need to be protected in later microfabrication process steps.

The third mask (BE2325-PDMS) defines the openings in the polymeric-based encapsulation for the passive DRG implant. The areas that have to be opened in this case are the electrodes and test pads, the rest of the implant should remain fully encapsulated, as shown in Fig. 42.

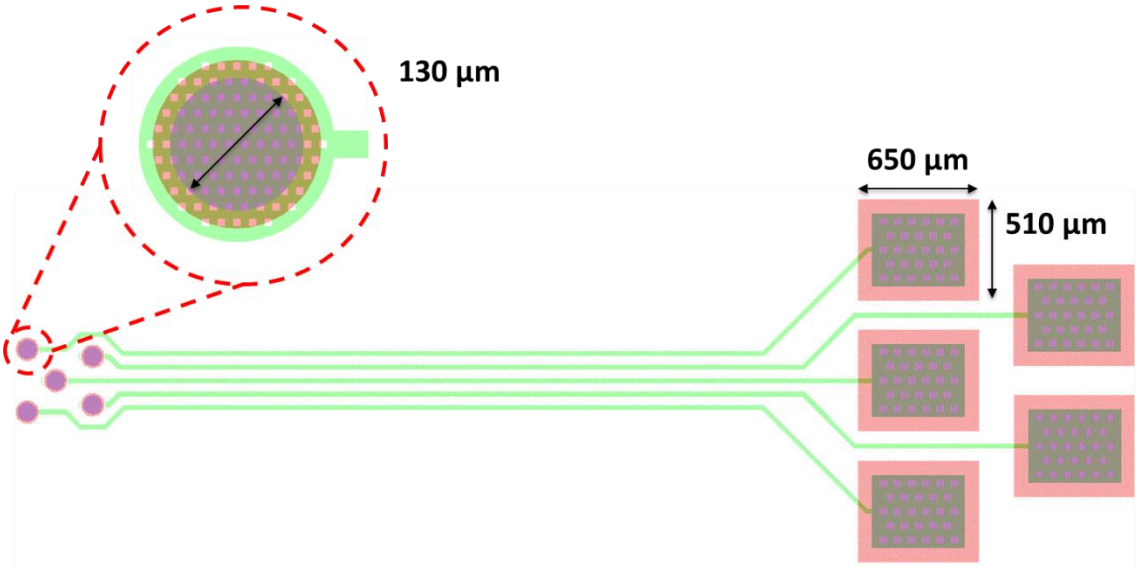

Fig. 42. BE2325-PDMS mask for defining the opening areas in the polymeric encapsulation layer.

Once having the complete passive structure defined and encapsulated in the first layer of polymer, it has to be released and later removed, in its final form, from the rigid substrate. To this end, the fourth mask (BE2325-DRIE) will be used and its design can be seen in Fig. 43.

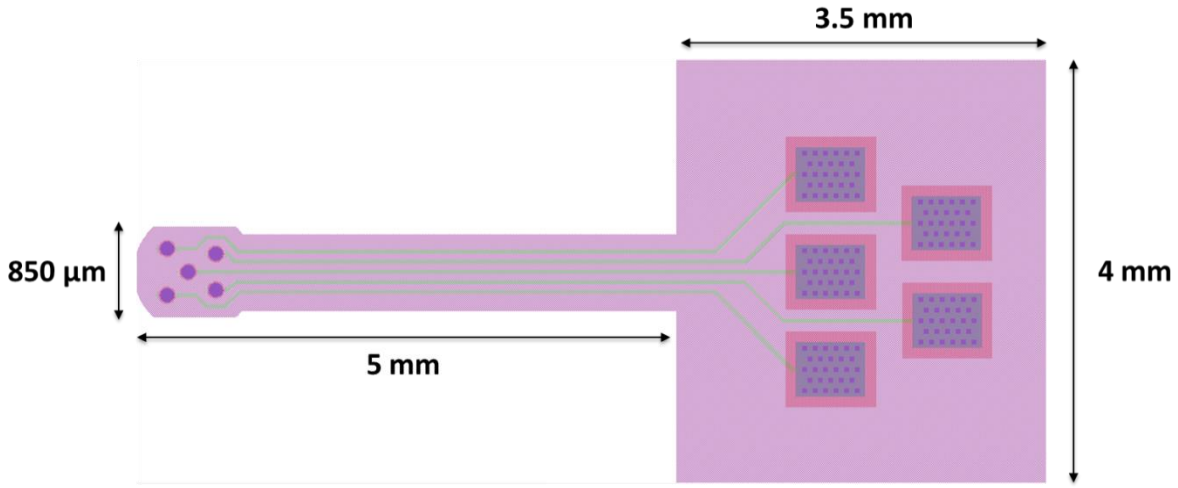

Fig. 43. BE2325-DRIE mask used to pattern the backside of the wafer for further release of the passive DRG implant.

3. 4. 4. Photolithographic masks used for the development of test structures

For the current project, two very important aspects for the graphene-based passive and active implants have to be evaluated. First, how bendable such an implant is and how mechanically stable and strong the graphene layer is. Second, since the implant is desired to be transparent, its optical transparency has to be investigated. To this end, two test structures, previously developed by G. K. Wardhana [63] were used.

In Fig. 44, the four masks for the bending test structures are illustrated. Note that the width of the graphene line is the same as for the graphene tracks used in the actual spinal cord implants.

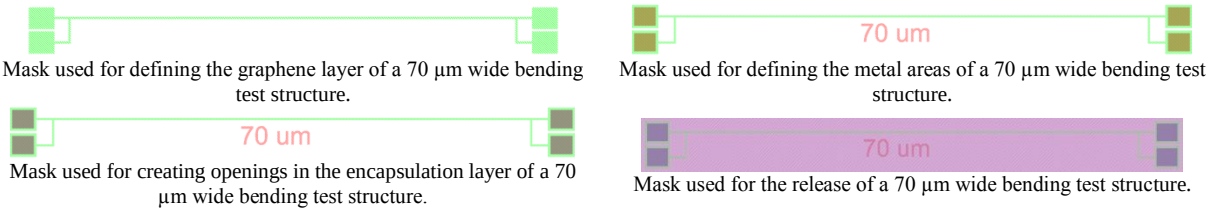

Fig. 44. Masks used to develop bending test structures.

To evaluate the optical transparency of the final implant, two test structures were developed. One will be used to determine the degree of transparency of the polymeric encapsulation only and the other one will evaluate the degree of transparency of a graphene and polymeric encapsulation layer. Both structures are shown in Fig. 45.

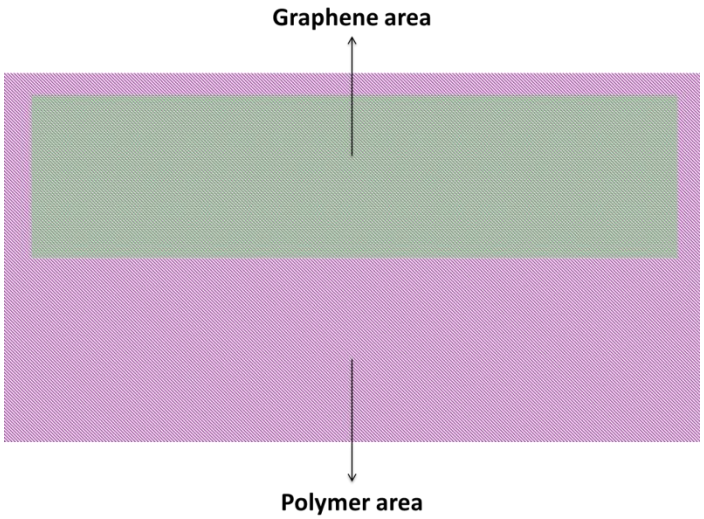

Fig. 45. Masks used to develop optical transmittance test structures.

4. Results and discussion

4. 1. Wafer-level graphene growth

For the development of both passive and active spinal cord implant prototypes, microfabrication was used in order to achieve high reproducibility and scalability of the process. However, for the envisioned structure, due to the limitations imposed by the application and the materials used, evaluation steps and intermediate measurements were needed to ensure high quality of the fabricated structures. As mentioned previously, the graphene-based electrode arrays and tracks were developed on a wafer-level, as shown in Fig. 46. The designs used to validate the process flow are different than the ones presented in Chapter 2, and were designed by G. K. Wardhana [63]. Based on the preliminary results obtained, the masks were optimized in a later stage of the project.

a) b)

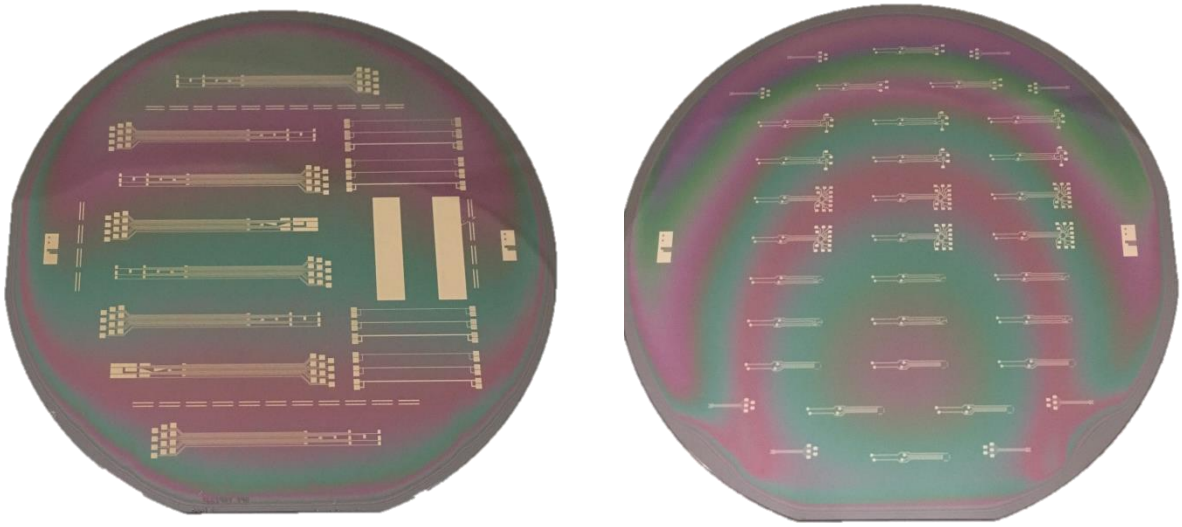

Fig. 46. Wafer-level graphene-based electrode arrays. In a), the initial design used to validate the process. In b), the final designs based on preliminary results and specifications from the neuroscientists.

Before performing any further process steps, the graphene layer, grown on a Mo catalyst had to be evaluated. To this end, Raman spectroscopy was employed to determine the presence of graphene on the metal catalyst and to quantitatively evaluate it.

From literature, it is already known that if graphene is present, the most important peaks should appear at well-defined locations. D peak should be present at ~1330 cm^{-1}, G peak at ~1590 cm^{-1} and 2D at ~2660 cm^{-1} respectively [41]. Thus, from Fig. 47, it can be concluded that after the CVD process, graphene is present on the metal catalyst.

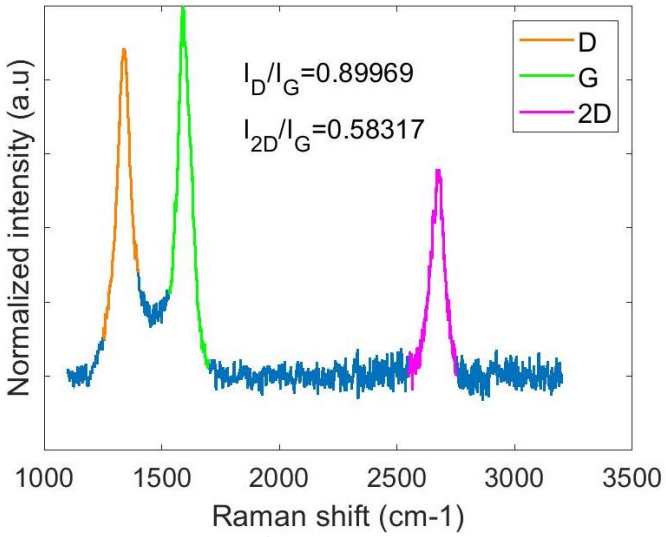

Fig. 47. Raman spectroscopy acquired after CVD growth process using a 633 nm laser.

From the ratio I_{2D}/I_G, inversely proportional to the number of graphene layers present on the substrate and generally greater than 1 for a monolayer, it can be concluded that a multi-layered graphene structure was developed. This ratio usually decreases significantly with the increase in number of layers [60]. The ratio I_D/I_G, on the other hand, estimates the number of defects present in the layer. Thus, the greater the ratio, the more defects can be found. They originate from the growth process and are highly dependent both on the metal catalyst used and on the process conditions. Ideally, if no defects are present, I_D should be equal to zero. Optimization of the graphene quality, however, was not in the scope of this project.

For the current project, having a multi-layered structure is considered to be advantageous due to the misalignment in the grain boundaries found between graphene layers. This increases the mechanical stability of the final structure, an important aspect for flexible implants. However, increasing the number of layers also means reducing the transparency of the structure which is not desired since the final prototypes should be suitable for optogenetic applications. Therefore, an optimum has to be found such that both mechanical stability and optical transparency requirements are met. In order to evaluate the transparency and also to estimate the number of graphene layers present, optical transmittance measurements were employed and the results are presented in one of the following sections of this chapter.

Besides qualitatively analysing the graphene layer, since its purpose is also to serve as a conductor during recording of electrical neural activity, two-point measurement evaluation was employed to determine the conductivity of the grown layer. In Fig. 48, the resistance of a graphene line of 70 µm wide and 1 mm long is shown.

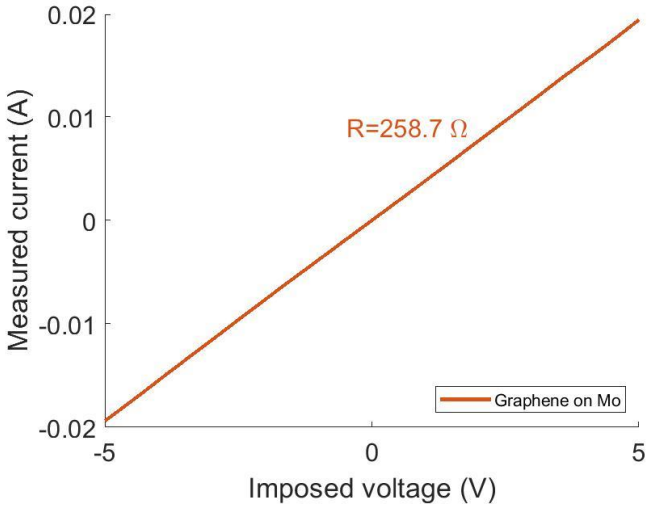

Fig. 48. Two-point electrical evaluation of a graphene line after the CVD process for graphene growth.

It has to be noted that Fig. 48 presents the resistance measured for a parallel configuration of both Mo and graphene since at this point the catalyst was not yet removed from the wafer. Therefore, the final measurements for a graphene-only track might vary with respect to the ones presented here.

4. 2. Encapsulation and suspension of the membranes

As shown previously in Chapter 3, for the current project, two different ways of transferring/releasing the structures from the rigid Si substrate were employed. The first approach that was investigated consisted of the creation of access points at the backside of the wafer and fabrication of the structures on the frontside. More explicitly, this approach imposed the development of graphene-based passive and active implants on oxide membranes, as described in detail in Chapter 3. For the creation of the aforementioned access points, an already available test mask was used to pattern the backside of the wafer. This comprised of circular structures with diameters ranging from 3 µm up to 150 µm.

Growing graphene on oxide membranes was initially tested on Si wafers with different thicknesses (300 µm and 500 µm) as for thinner wafers, more openings, even smaller in diameter could be created in shorter periods of time. This is due to the fact that especially for small and deep structures, the etch rate decreases over time since less ions get in contact with the surface that has to be etched. Moreover, the directionality of the DRIE process is affected, the bottom of the structure becoming more tapered. Therefore, since for 300 µm Si wafers there was less material that had to be etched, smaller structures could be successfully opened. To this end, first the Si wafers were prepared by depositing the oxide hard mask, and DRIE processes were employed to open the through-hole Si vias (TSV) that would later act as access points for the wet chemical etchants. In Fig. 49, both frontside and backside of the wafers are illustrated after performing the DRIE process. It can be observed that for a 300 µm Si wafer, openings with diameters down to 25 µm were successfully created from the backside of the wafer without damaging the oxide layer on the frontside. However, for a 500 µm Si wafer, only openings with diameters down to 60 µm were successfully created.

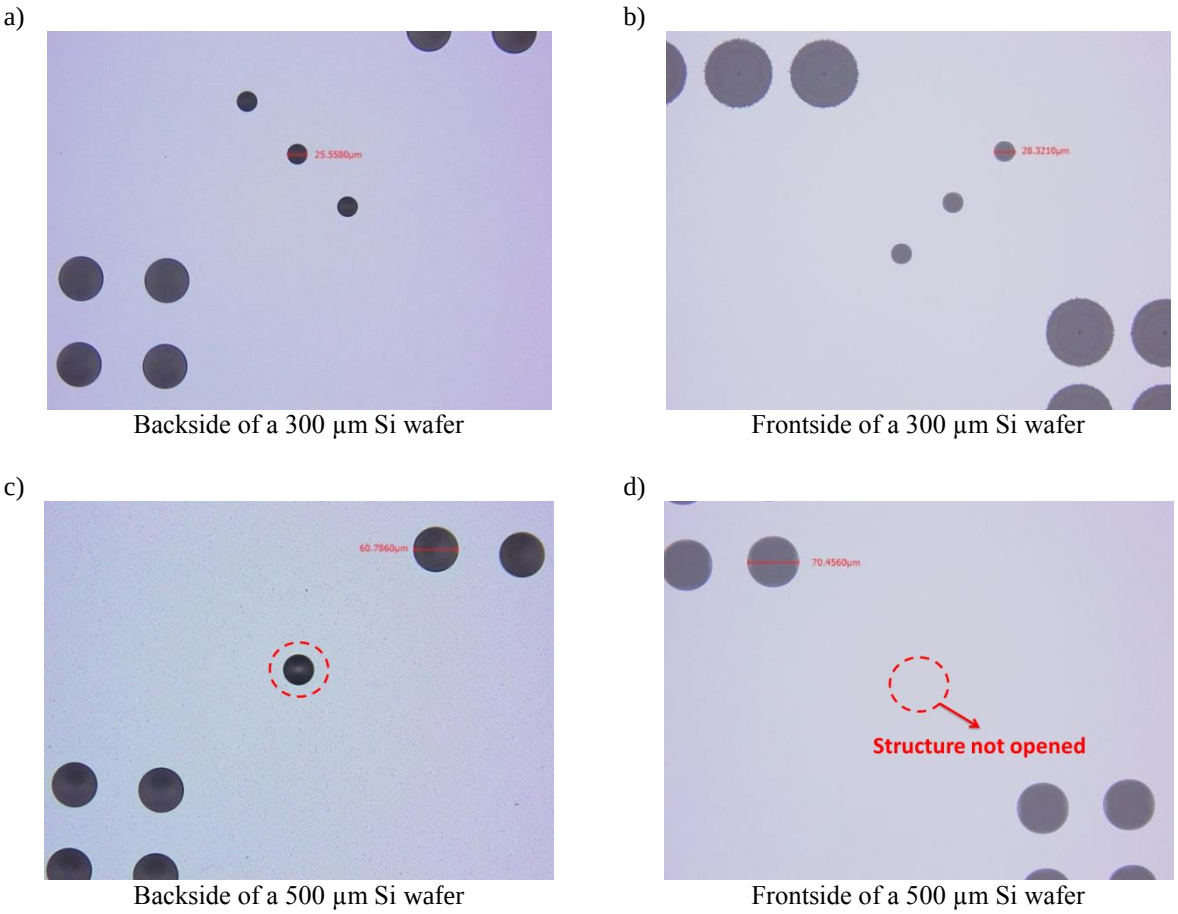

Fig. 49. Microscope images illustrating the minimum diameter of the TSVs for a 300 µm, a) and b), as well as for a 500 µm, c) and d) Si wafer.

Having the oxide membranes, the next step was to deposit and pattern the Mo layer, on top of which graphene could be grown. Moreover the fact that the CVD process for graphene growth requires elevated temperatures (above 900 °C), prompted the hypothesis that the oxide membranes would eventually break, due to the stress induced from the microfabrication steps. However, Fig. 50 illustrates that all oxide membranes survived the graphene growth process.

a) b)

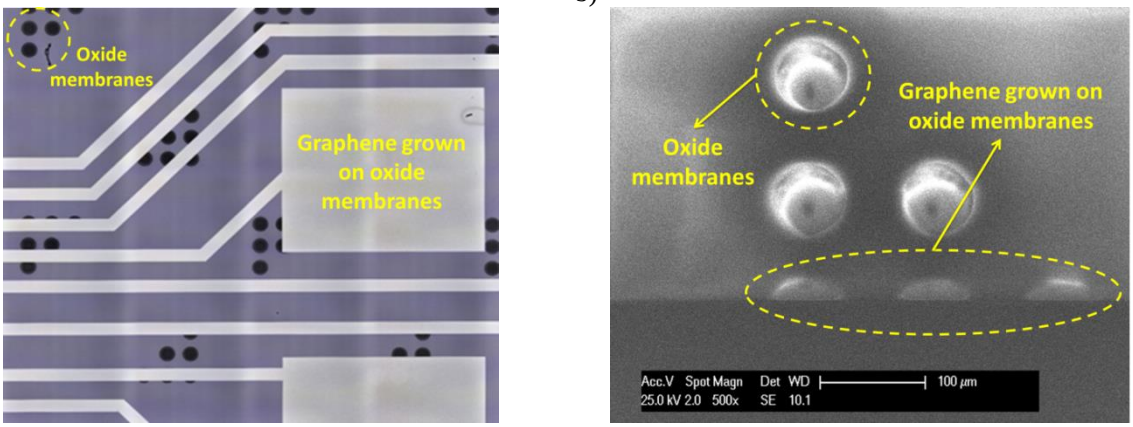

Fig. 50. Microscope (a) and SEM (b) images after graphene growth on oxide membranes with different diameters.

In order to have the implant in its final form, the graphene-based structures had to be transferred and encapsulated in PDMS. To do so, first, a layer of PDMS was spin-coated on top of the wafer and later wet etching steps were employed to remove the remaining oxide and Mo layers underneath graphene.

For oxide etching, BHF 7:1, with an expected etch rate of 150 nm/min was used. The calculated time for the complete removal of the oxide was ~40 minutes. Yet, after 7 hours, no etching of the target layer around the TSV was observed. Therefore, it has been assumed that the DRIE process employed for the TSV resulted in the deposition of a polymer layer inside the cavity, which could not be removed by O_2 plasma treatment.

To overcome this, a second attempt of transferring the structures was employed. First, potassium hydroxide (KOH) etching was performed for 5 hours, between 50°C and 60 °C to widen the TSVs such that BHF could easily reach the oxide layer. However, after these long wet etching steps the structures were highly damaged and in some parts completely removed. Therefore, it was concluded that for the current project, in order for the passive structures to survive, wet transferring methods should be avoided as much as possible. Another reason for avoiding wet process steps is that later in the process, at this step, chips, ideally containing active components, will also be present.

To this end, the second approach presented in Chapter 3 was investigated. This consisted of first, developing the graphene-based structures on top of the wafer and later suspending the complete implant area from the backside of it. Removing the remaining oxide and Mo layers was initially performed using relatively short wet etching steps compared to the previous case (1 hour for oxide etching in BHF and ~5 min in peroxide (H_2O_2)) and in Fig. 51, the first graphene-on-PDMS suspended structures are illustrated.

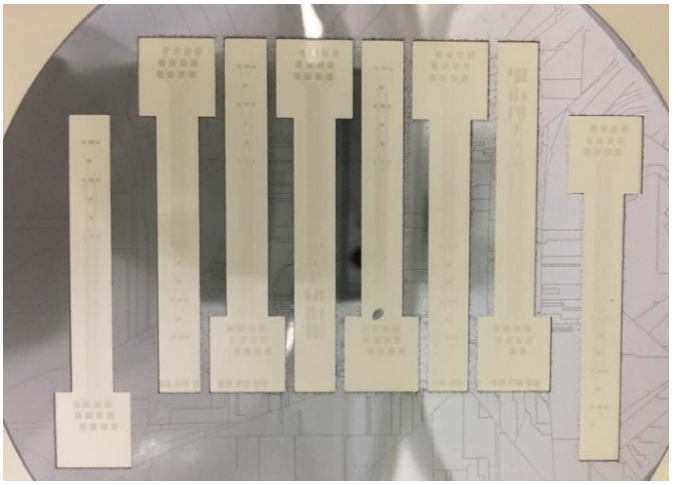

Fig. 51. Photograph of 8 suspended graphene-on-PDMS prototypes. The structures were developed on a 10 cm Si wafer.

After the successful suspension of the implants, Raman spectroscopy was employed to ensure that the graphene layer did not present any critical damage after the microfabrication process. Fig. 52 illustrates the Raman spectra of graphene after suspending the structures. Comparing these results with the ones presented in a previous section of this chapter, namely I_D/I_G=0.89 and I_{2D}/I_G=0.58, it can be concluded that no critical damage was present on the graphene layer after employing all the microfabrication process steps.

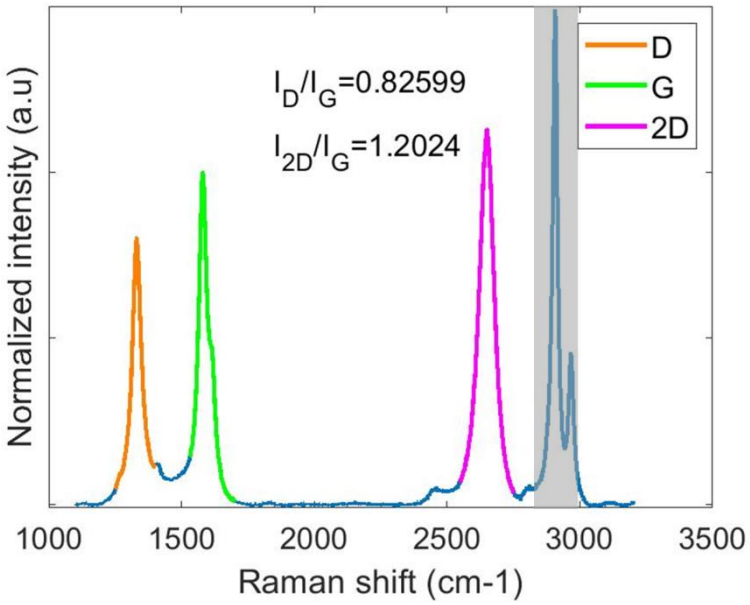

Fig. 52. Raman spectroscopy acquired using a 633 nm laser, after suspending the implants.

The ratio I_D/I_G, now equal to 0.82, is similar to the one previously reported, meaning that the number of defects present in the graphene layer, after post-processing methods employed to suspend the implant structures, remains similar. This result gives a clear indication of the fact that the release method employed for the current project does not influence the quality of the graphene layer. On the other hand, the ratio I_{2D}/I_G, estimating the number of graphene layers, increased compared to the previous measurements. However, from this result it cannot be firmly concluded that less graphene layers are present after suspension. The change observed in the measured values is likely caused by the material present underneath graphene, in this case PDMS, or previously, Mo on top of oxide [64]. Moreover, as single point measurements were performed for each sample, variations in the results might occur also due to the different location that was measured. A significant difference from the previous measurements is represented by the appearance of two new peaks, illustrated in Fig. 52 by the grey area. These indicate the influence of PDMS over the Raman measurement.

Apart from Raman spectroscopy, two-point measurements over a 1 mm long and 70 µm wide graphene line were employed to evaluate the conductivity of it after Mo removal. Fig. 53 illustrates both the structure under test as well as the measured resistive values.

a)

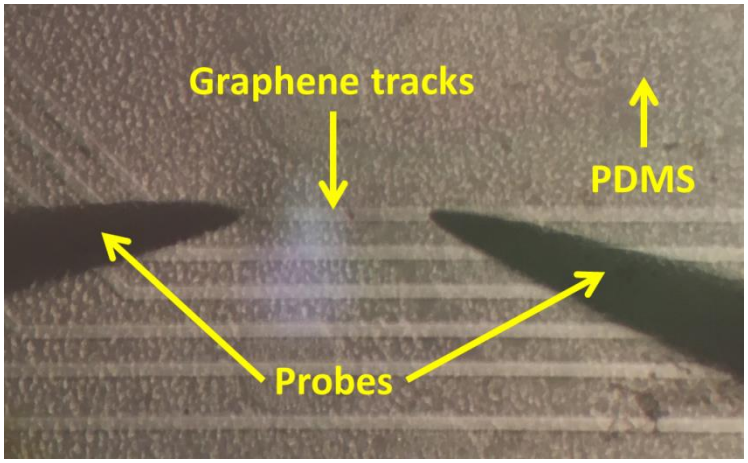

b)

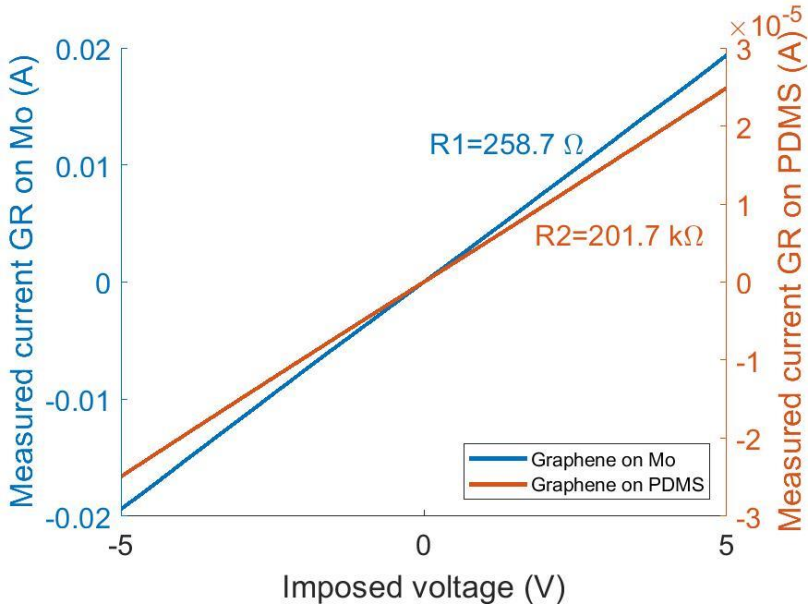

Fig. 53. Two-point measurements after releasing the structures using DRIE and wet etching steps for the oxide and Mo layers. In a), the structure (graphene-on-PDMS) under measurement is illustrated. In b), the resistance values after suspension in comparison to the ones obtained after graphene growth.

A significant difference in the measured resistance value can be seen after suspending the implants and removing the Mo layer underneath graphene. This originates from the fact that after graphene growth, the measured resistance is from a parallel configuration of Mo and graphene, whereas for the suspended structures, only the graphene layer was probed. Therefore, the resistance of Mo is much lower than that of graphene and thus the total parallel resistance was significantly lower. Moreover, since a two-point electrical evaluation was employed, the contact resistance from the probes plays an important role in the final measured value, due to its less controllability. Also, for the suspended implants, a graphene layer was directly probed, without having any metal interface between the probes and the measured layer. This would have been of great use for accurate landing the probes without further damaging of the graphene layer. Ideally, dedicated structures have to be developed for accurate measurement of graphene resistance. However, from these results it can be concluded that despite the extensive microfabrication process, the electrical conductivity of graphene is still present.

Having the structures suspended, the final layer of PDMS encapsulation can be spin-coated and cured in order to have the implant in its final form. However, for the implant to be functional, openings for the electrodes and test pads have to be created in one of the two PDMS layers. To this end, a second iteration of the process was employed, using the optimized redesigned masks.

For the second iteration, before applying the first layer of PDMS encapsulation, a metal interface layer had to be deposited over the graphene-based structures to improve electrical contacts. Patterning was made such that only the electrodes and test pads would have a layer of metal on top. This would also serve as a stopping layer for PDMS etching and thus protecting the graphene layer underneath. Next, the first layer of PDMS was

deposited and prepared for etching of the openings. To this end, a metal hard mask had to be deposited and patterned on top of PDMS, as shown in Fig. 54 a.

a)

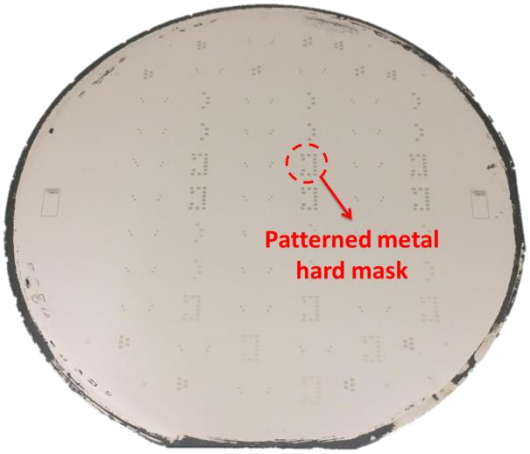

b)

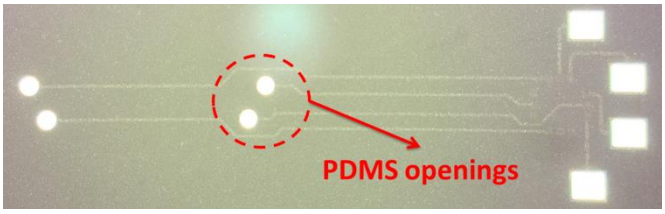

Fig. 54. PDMS openings for the elctrodes and test pads. In a), the patterned hard mask is shown. In b), an implant structure after opening the PDMS layer and landing on the metal stopping layer underneath.

Next, the implants had to be suspended such that later the final layer of polymeric-based encapsulation could be applied. To this end, a DRIE process, as for the first iteration, was employed. Next, a BHF wet etching step for removing the oxide layer from the backside, while protecting the frontside with a photoresist layer was performed. However, apart from oxide, the thin Ti layer is also rapidly etched in BHF solutions. Therefore, once the metal test pads got in contact with the etching solutions, they were completely removed, thus leaving a thin layer of graphene without any mechanical support. To circumvent this and to prevent the breakage of the membranes, dry etching processes were employed for the removal of the oxide layer. The first attempt was to use the same tool as for DRIE of Si. However, the combination of gases available (C_4F_8 + He + CH_4) were not selective to Mo and thus the structures were again damaged. Using a plasma etcher (Alcatel) with soft landing and high selectivity to Mo due to the gases used (CF_4 + SF_6) was employed, as a second attempt and the resulted structures are illustrated in Fig. 55. The disadvantage in this case is the fact that the etching rate is relatively slow, 20 nm/ minute and thus the process is time consuming. One possibility would be to thin the layer using the DRIE tool, down to a few hundreds of nm and then employ a plasma etching with soft landing and high selectivity to completely remove the oxide layer.

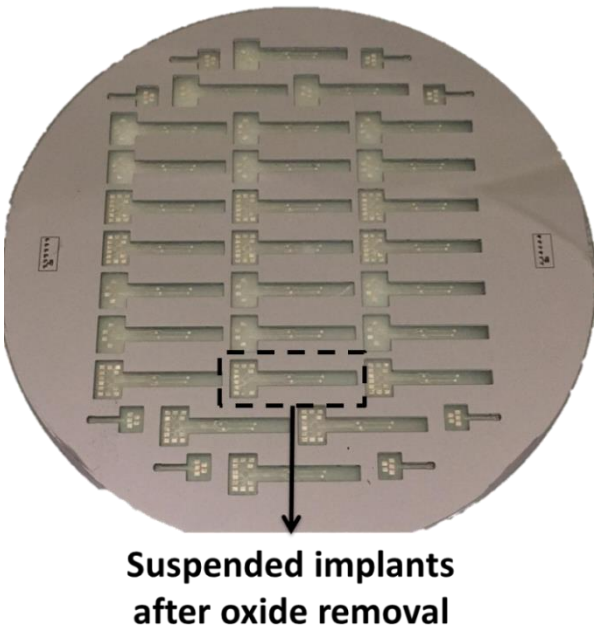

Fig. 55. Suspended implants and oxide removal using dry etching process steps.

Finally, Mo was removed using peroxide solutions for ~5 minutes and the final layer of PDMS encapsulation was spin-coated and cured. The final suspended passive implants are shown in Fig. 56. The same process applies for the development of active implants.

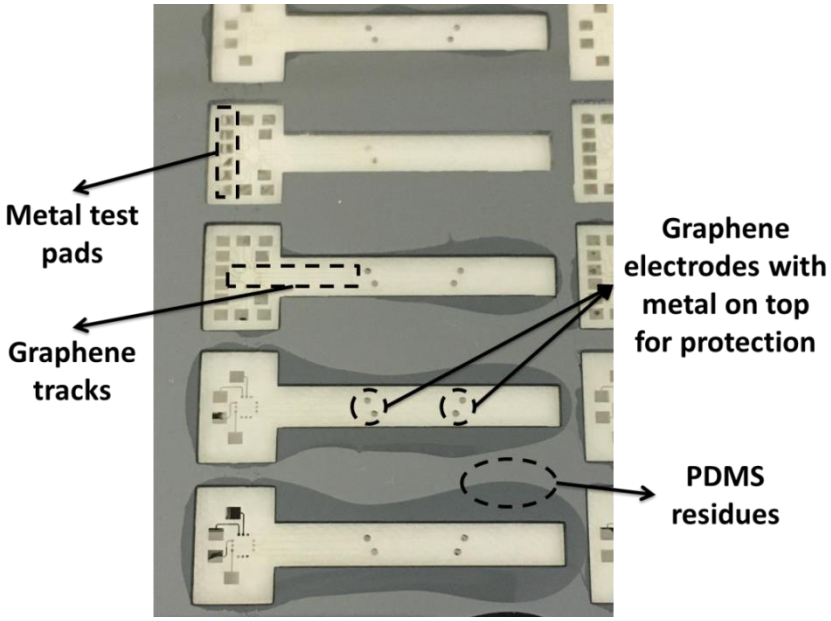

Fig. 56. Suspended implants after Mo removal and second layer of PDMS encapsulation.

Suspending the implants requires, first, a DRIE process performed from the backside of the wafer to remove the Si substrate while landing on the oxide layer on top. This requires having a low-stress material for landing, thus avoiding further damage of the structures once suspended. However, due to the issues regarding the recipe stability of low-stress PECVD oxide, cracks formed during graphene growth processes, thus damaging the structures. Therefore, TEOS, with a compressive stress of hundreds of MPa had to be used instead. Therefore, after DRIE processes, the structures presented some visible damages on the Mo layer and thus also on graphene. For these reasons, the structures could not be electrically measured after their suspension. Only visual inspection and Raman spectroscopy were employed to ensure the presence of graphene after Mo removal (Fig. 57).

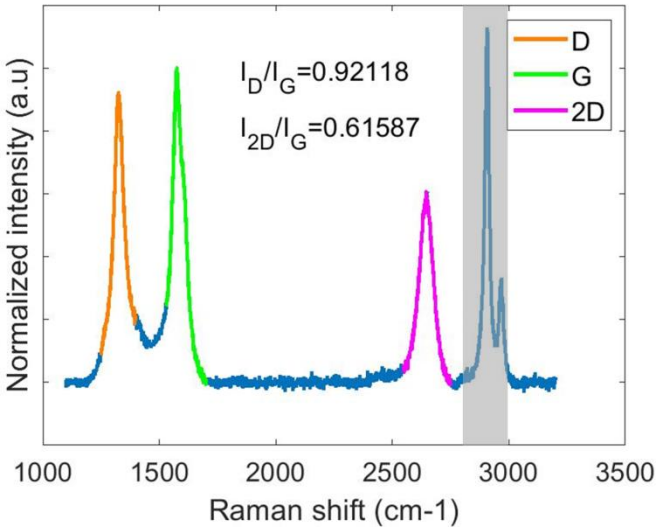

Fig. 57. Raman spectroscopy performed after the suspending the implants and removing the Mo layer. Raman spectroscopy was performed before applying the second layer of encapsulation.

From the Raman spectra it can be observed that the graphene layer presents more defects than before, judging from the I_D/I_G ratio. This is likely due to the plasma etching processes employed to suspend the membranes but also due to the tensile stress induced by the oxide layer. However, Raman spectroscopy provided a good indication that graphene is still present on the first PDMS layer after all layers are removed from below.

4. 3. Flip-chip bonding

Developing an active implant from a passive electrode array requires the integration of active components with the passive structures. To achieve this, system integration of chips with the microfabricated graphene-based electrode array had to be investigated. To this end, flip-chip bonding techniques of dummy chips were employed. The dummy chips, developed on a Si wafer, consist of an Al (1%Si) metal layer in the form of a daisy chain used for later evaluation of the bonding process. On top, the passivation layer with the openings for the contact pads can be found. In the openings, Au stud bumps, with a diameter of 80 µm were manually created, using a manual wire bonder (as shown in Fig. 58) and the chips were then diced and prepared for flip-chip bonding. It has to be noted that in order to validate the process, non-optimal dummy chips (Fig. 59 a) were developed that could match the design on the substrate wafer. Therefore, for the first trial, there were no dedicated structures that could measure the resistance of individual bumps after flip-chip bonding. However, this was taken into account during the redesign process (Fig. 59 b).

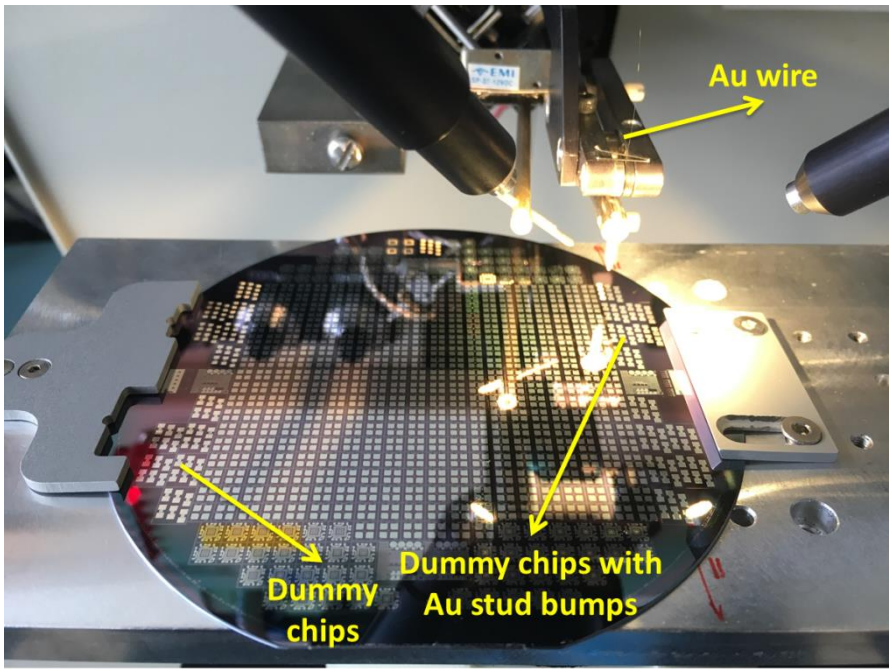

Fig. 58. Au stud bumps creation using a manual wire bonder.

a) b)

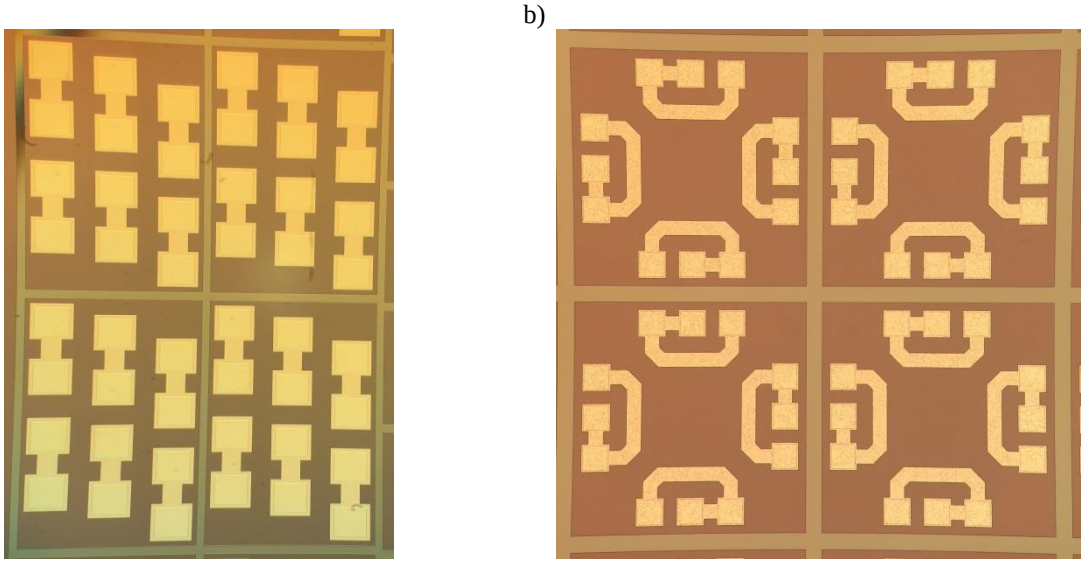

Fig. 59. Microscope photograph of both initial, a) and final, b) designs of the dummy chips used to evaluate the flip-chip bonding processes.

So far, to the best of our knowledge, no such processes on graphene substrates have been reported in the literature. For this thesis, the first attempt was to directly bond the dummy chips on graphene pads without any metal interface between the two. However, since the C-C bonds forming the graphene lattice are very strong, diffusion of Au could potentially occur only at areas where graphene presents defects. Therefore, the bond between Au and graphene might not be strong enough to keep the dummy chip on the substrate. Moreover, since the graphene structure comprises of several layers, coupled by weak Van der Waals forces, it can be assumed that delamination of the Au bumps from graphene is likely to occur. Therefore, a metal interface had to be added on the substrate wafer. For bonding purposes, Al (1%Si) was considered to be the most suitable material. Therefore, a layer of 675 nm of Al (1%Si) were sputtered on top of graphene and later patterned. Since the metal layer was intended to be kept only on the test pads for flip-chip bonding and on the electrodes for protection, dry etching process steps could not be considered an option. This is due to the fact that the wafer is considered contaminated after graphene growth and landing on a contaminated material, after dry etching is forbidden inside the cleanroom. Moreover, since dry etching processes for the metal layer would involve the use of plasma, which degrades the graphene layer, wet etching, using hydrofluoric acid (HF) (0.55 %) had to be employed in order to achieve the final structure for the metal interface. HF, highly used for etching Al metal layers was chosen mostly because it has a very high selectivity to Mo. Therefore, Mo would not be etched during this process step, an important aspect as at this stage, graphene is still on the Mo catalyst.

After metal deposition but especially after employing the wet etching step for Al (1%Si) it has been noticed that there is poor adhesion between it and graphene [55], as shown in Fig. 60.

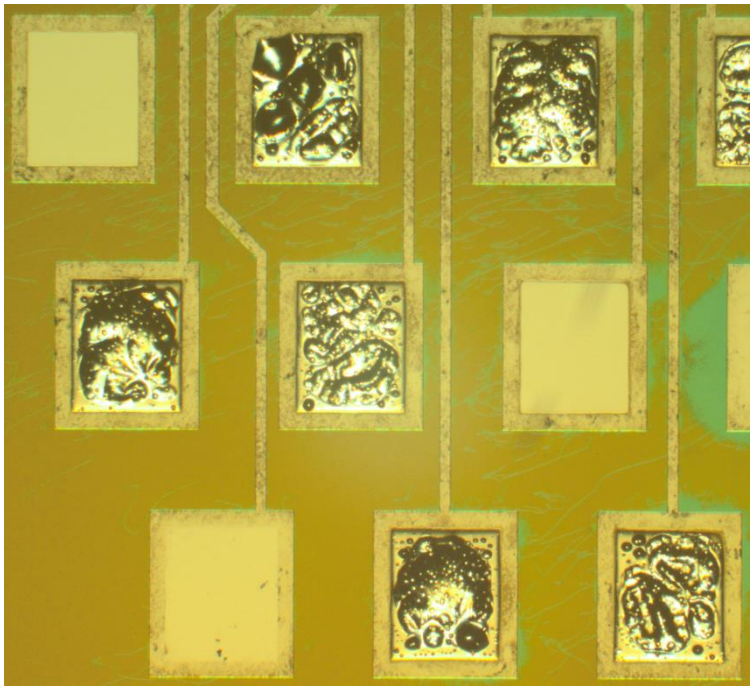

Fig. 60. Delamination of Al from the graphene pads.

To overcome the delamination problem, Ti was chosen to be in direct contact with graphene since it has been proven to have a good contact resistance with it [56], [57]. However, Ti is not a good candidate for bonding purposes and thus, a stack of metal layers (Ti (100nm) and Al (1%Si) (675nm)) was chosen to serve as an interface between the graphene substrate and the Au stud bumps on the dummy chips.

Having a more stable metal interface, flip-chip bonding at Fraunhofer IZM in Berlin was employed and in Fig. 61, the structures, before and after this process step are shown. The chips were bonded using a thermocompression flip-chip bonding technique over a 60 seconds cycle at 250 °C, while applying roughly 19 MPa of pressure per bump (~10 g/ bump). The total force per chip area, used in this case was ~2 kg. As this was the first attempt for flip chip bonding, the parameters were not optimally adjusted for the number of bumps on the pads of the chips.

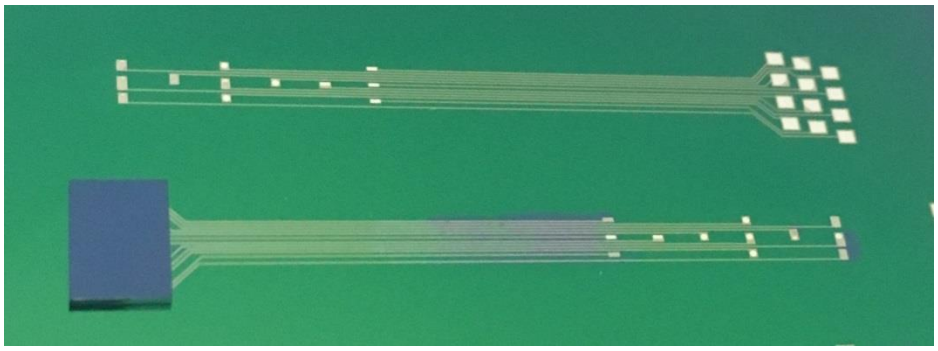

Fig. 61. Graphene-based structures before and after flip-chip bonding.

To evaluate the bonding process, first, computed tomography (CT) scans were employed. This provided more insight into the shape of the Au stud bumps after the process, and as shown in Fig. 62 a, the bumps have a coined-like shape, indicating that contact between the dummy chip and the graphene-metal substrate was made. Apart from this, in Fig. 62 b, two-point measurement results are shown. It should be noted that the resistance, ~8.6 kΩ, is the sum of 2 stud bumps and 2 graphene tracks resistances. This is because, as previously mentioned, for the initial designs, there were no dedicated structures that could be used to evaluate only the stud bumps.

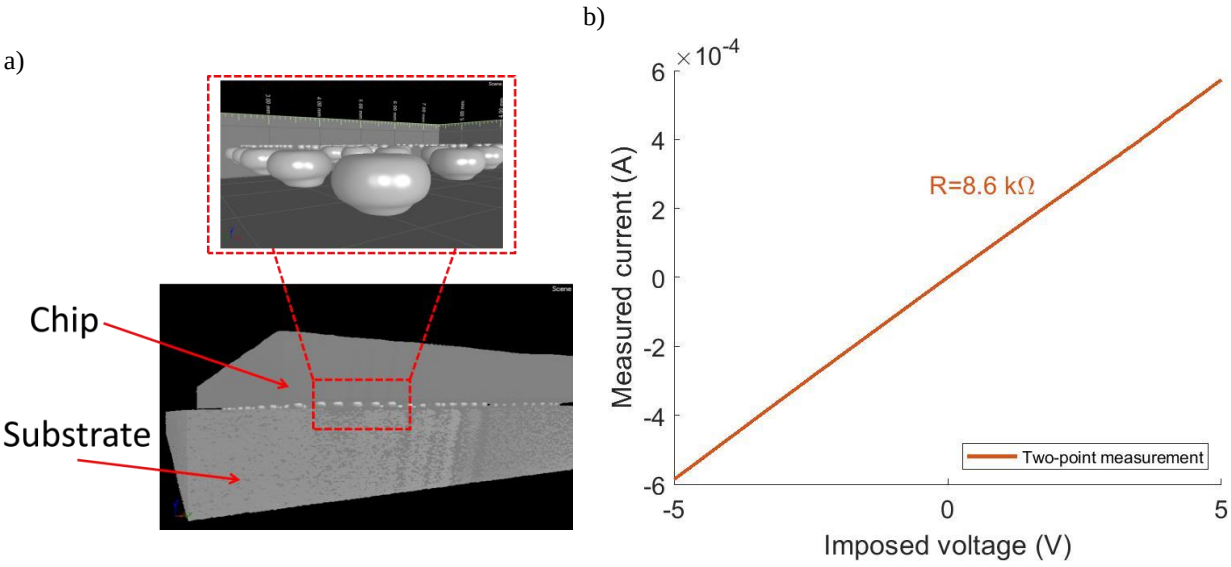

Fig. 62. CT scans and two-point measurement results after the bonding process.

As the process showed promising results, a second attempt of bonding dummy chips directly on a graphene-based substrate, without any metal interface was performed. This time, however, an anisotropic conductive adhesive (ACA) (Toshiba TAP0212E) with nickel (Ni) particles was used to ensure contact between the Au stud bumps and graphene. Before bonding, the adhesive was pre-heated at 90 °C for 30 seconds for degasing purposes and then chips were bonded following the same thermocompression bonding cycle as before. In Fig. 63, the two-point measurement results, similar to the ones obtained previously, are illustrated.

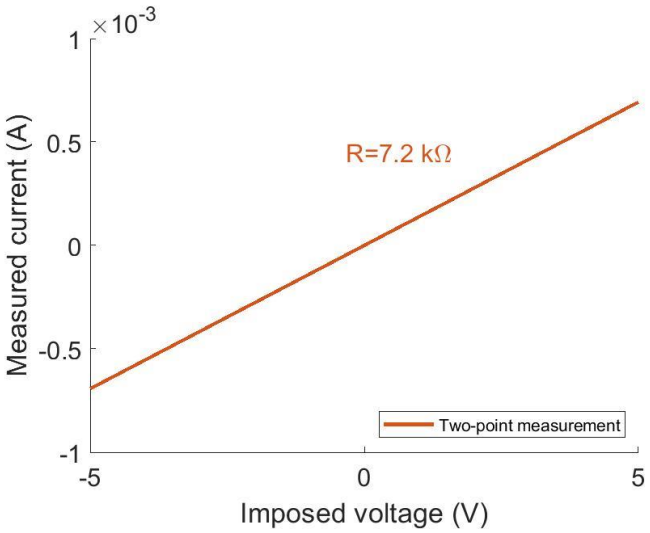

Fig. 63. Two-point measurement results after the ACA bonding process performed on a graphene substrate without metal interface.

These results indicate that ACA adhesive with Ni particles provides better adhesion to graphene than direct Au to graphene bonding, presented as the initial attempt. Therefore, by improving the flip-chip bonding process, connections on graphene-only substrates were also made. However, the chemistry behind this is outside the scope of this thesis.

According to the aforementioned results, but also in accordance to the requirements for the *in-vivo* experiments, it has been decided that the masks have to be redesigned. Moreover, adhesives, either conductive, for graphene substrates, or non-conductive (NCA), for graphene and metal substrates should be used both as an underfill material but also to improve the bonding stability.

After redesigning the masks, the adhesion between graphene and the metal layer on top was visually inspected and the results are shown in Fig. 64. Due to the improved design for the graphene structure but also due to the fact that the metal pads were slightly bigger than the graphene ones, as presented in Chapter 2, the adhesion of Ti and Al (1%Si) and even the adhesion of just Al (1%Si) was perfect as all pads survived the patterning process.

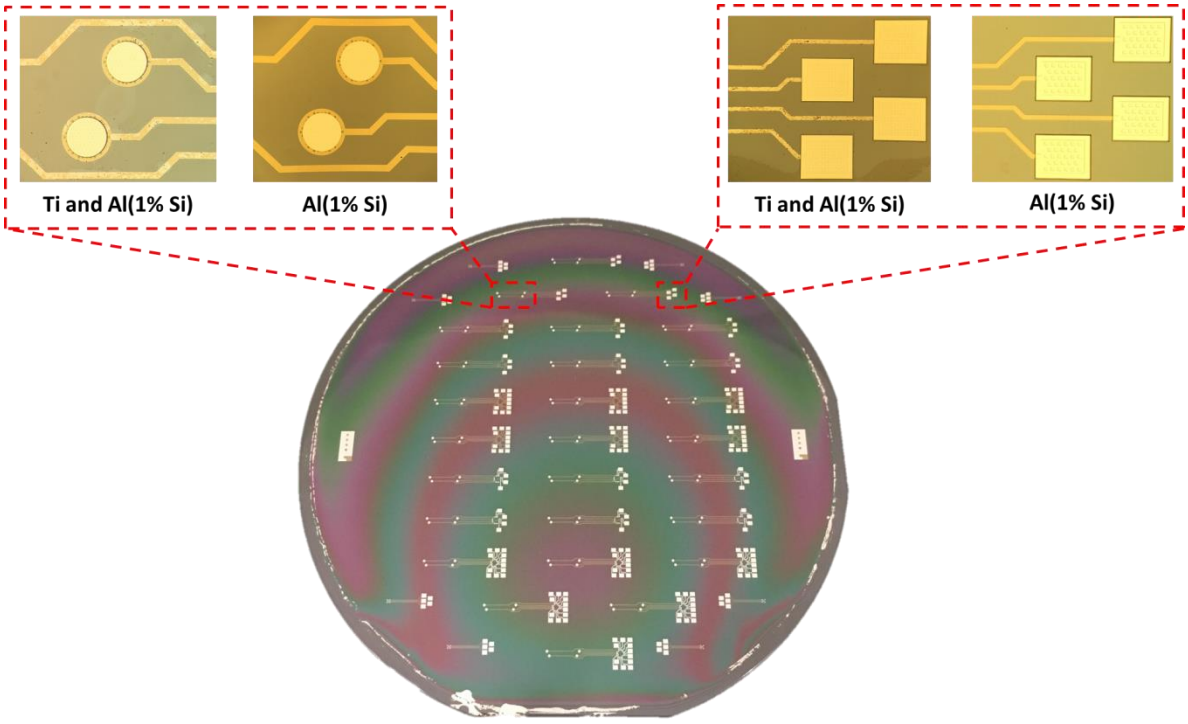

Fig. 64. Redesign of masks and metal interface sputtered and patterned on a graphene substrate.

For the improved graphene-based structures, flip-chip bonding processes, either with NCA or ACA, depending on the structure on top of which the chips were bonded, was employed. The parameters used were according to what has previously been reported in the literature for Au bumps similar in diameter as the ones used for the current project [65]. Therefore, they were relatively different, especially in terms of applied pressure compared to the first flip-chip bonding processes performed. Due to the fact that fewer bumps were created on the surface of the dummy chips, less force per total chip area was needed to perform the bonding process. To this end, 60 g/bump were uses, meaning ~ 117 MPa, leading to a total force of 720 g per chip area.

In Fig. 65, the bonded dummy chips are illustrated. Two types of bonding processes for four different types of substrates were employed as synthesized in Table 4.

Table 4. Flip-chip bonding performed on different substrates.

Flip-chip bonding on redesigned substrates				
SUBSTRATE TYPE	**CONFIGURATION OF TEST PAD**	**CONFIGURATION OF TRACK TOWARDS THE CHIP**	**CONFIGURATION OF BONDED AREA**	**BONDING TYPE**
1	Metal	Metal	Graphene and Metal (substrate) + Au and Metal (from chip)	NCA
2	Metal	Metal	Holey Graphene and Metal (substrate) + Au and Metal (from chip)	NCA
3	Graphene and Metal	Graphene	Graphene (substrate) + Ni particles (adhesive) + Au and Metal (chip)	ACA
4	Holey Graphene and Metal	Graphene	Holey Graphene (substrate) + Ni particles (adhesive) + Au and Metal (chip)	ACA

For the first two rows of bonded chips (Fig. 65), an ACA was used since the bonding was performed directly on a graphene substrate without any metal interface. Moreover, the graphene pads on top of which the chip was bonded, presented either a holey structure, or a full graphene pad, as illustrated in Fig. 38 of Chapter 3. 4. For the rest of the chips, a NCA was used since a metal interface was present between the graphene pads and the Au stud bumps of the chips. In this case, the structure of the graphene-based substrate is as presented in Fig. 37 of Chapter 3. 4.

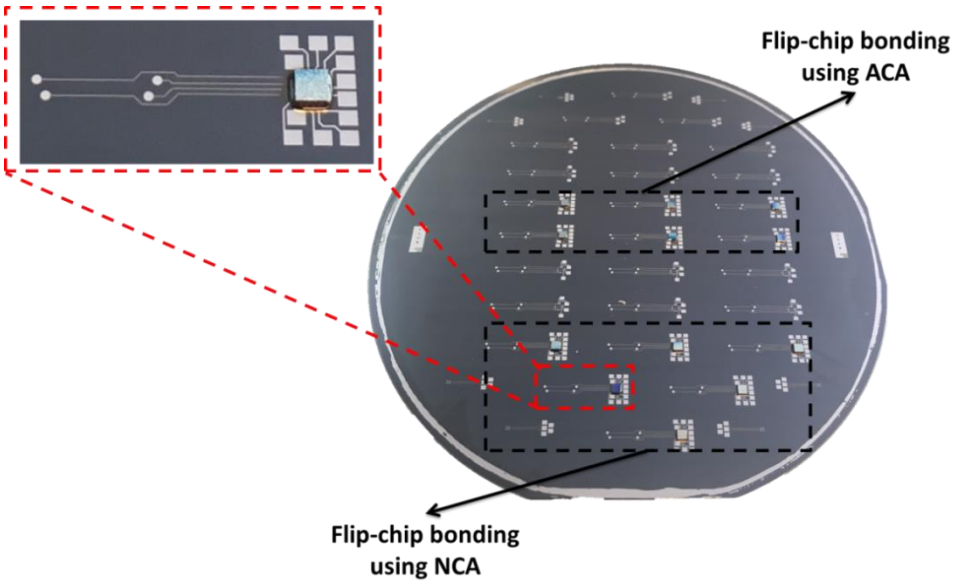

Fig. 65. Flip-chip bonding of redesigned dummy chips using both ACA and NCA adhesives.

Since both the substrate and the chips were redesigned for this second iteration, measurements were needed (Fig. 66) in order to evaluate the bonding process and the influence of different layers and configurations of the substrates.

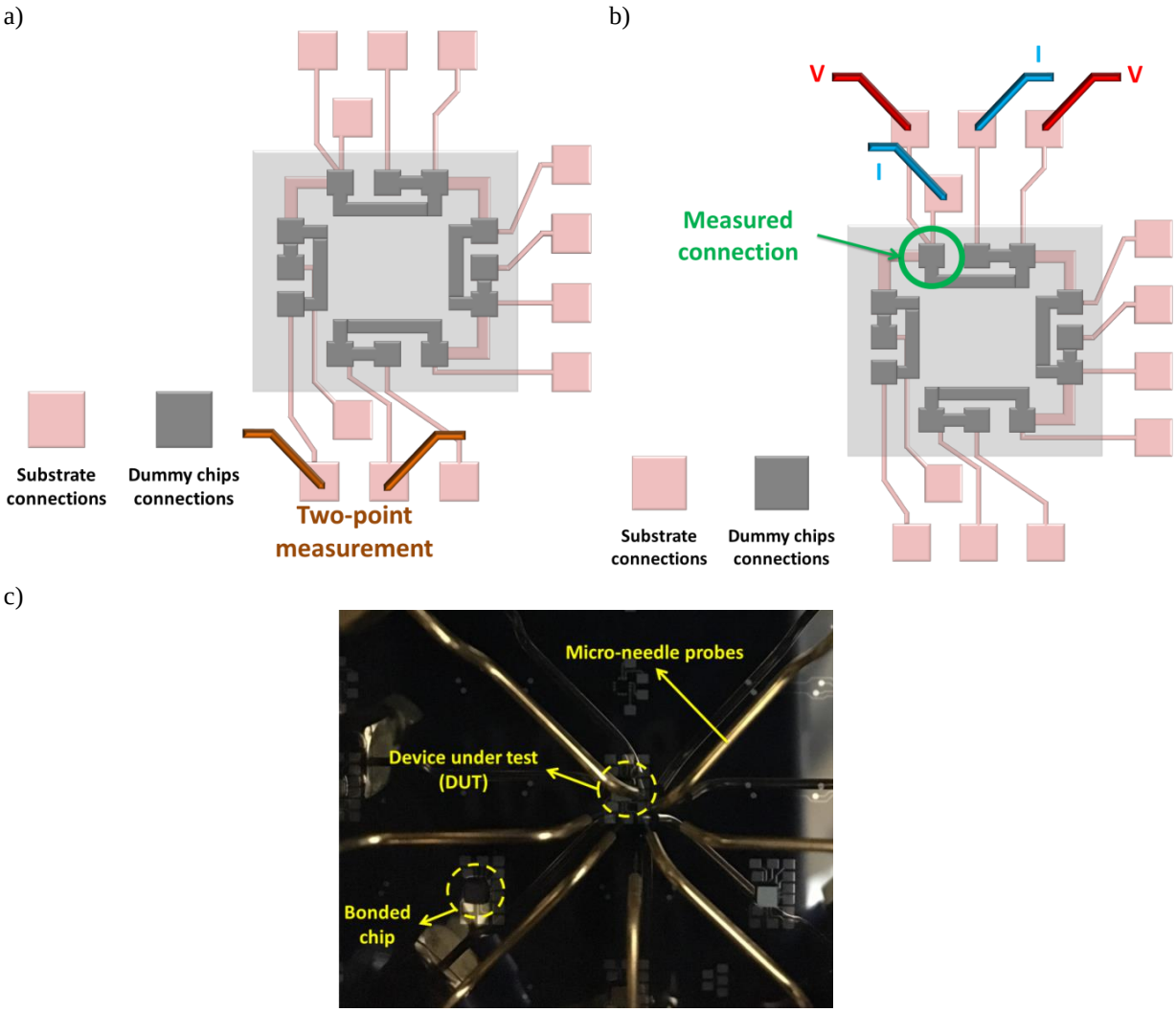

Fig. 66. Two-point a), and four-point measurements b), of the dummy chips after the bonding process. For the illustrated iteration c), both the chips and substrate were redesigned.

First, two-point measurements were employed, in two different locations (one of them shown in Fig. 67), for all 4 chips that were evaluated. The results indicated that all chips were bonded to the substrate. Moreover, from Fig. 68, it can be concluded that apart from the contact resistance, which is difficult to estimate, the materials used influence the results significantly. For the substrate having the test pads and tracks towards the chips out of metal only, the resistance of the complete daisy-chain was in the range of a few ohms. On the other hand, for the graphene and metal test pads and graphene-only tracks, the total resistance of the daisy-chain was significantly increased (~ 350 Ω). It should be noted that for the daisy-chain indicating lower resistance values, the voltage sweep had to be reduced, in order to accurately perform the measurements.

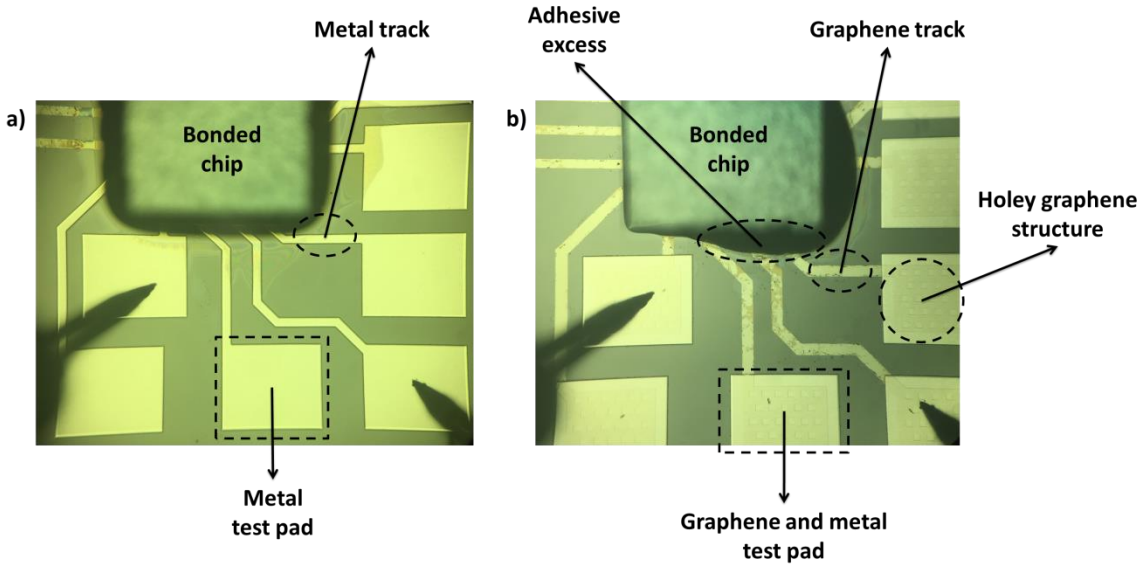

Fig. 67. Two-point measurement of the dummy chips after the bonding process. In a), the metal test pads and tracks are shown. In b), the graphene and metal test pads, together with the graphene-only tracks are illustrated.

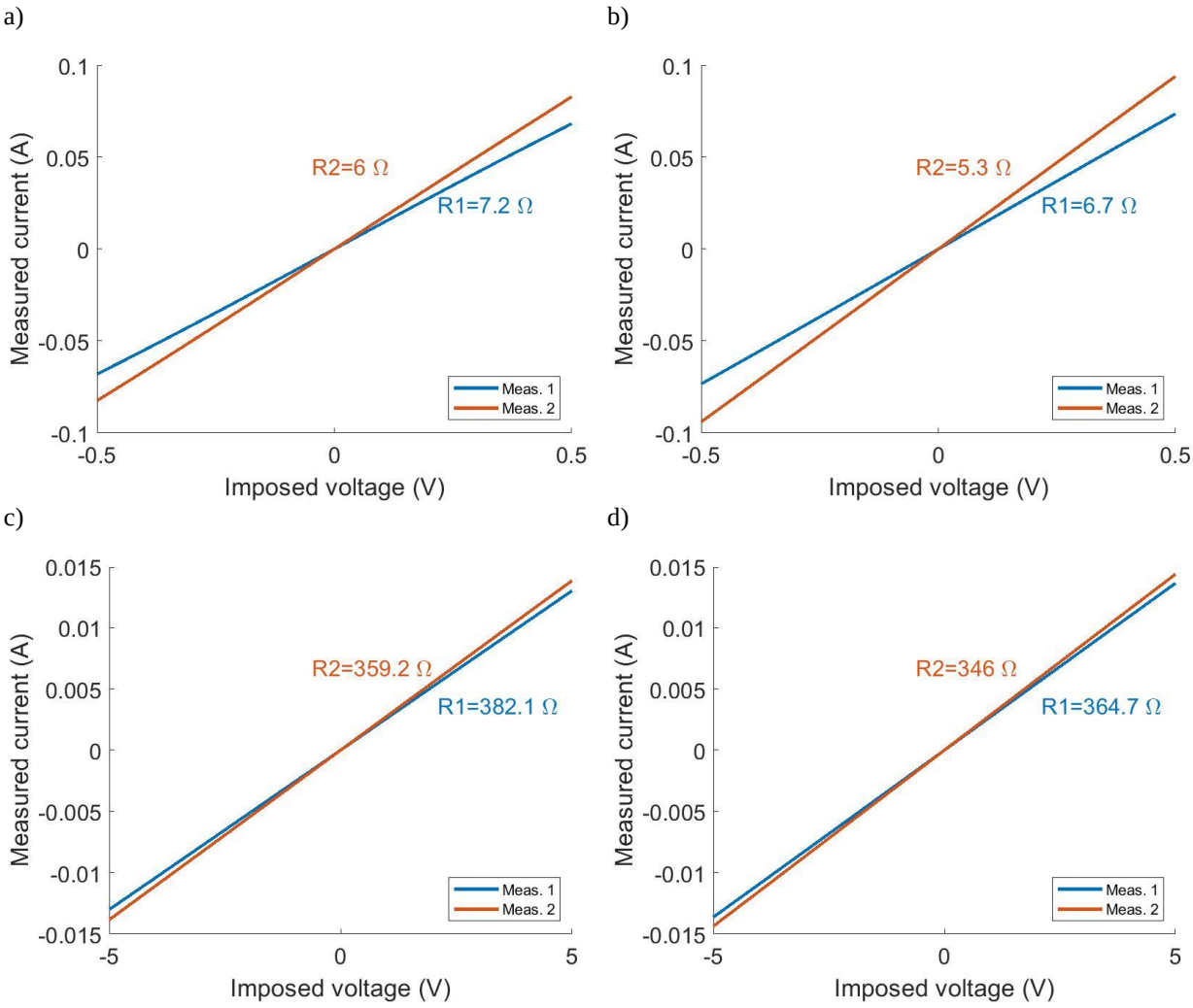

Fig. 68. Two-point measurements of dummy chips after the bonding process. In a) and b), the substrate structure consisted of metal-based test pads and tracks towards the chip. In c) and d) the substrate consisted of graphene and metal test pads and graphene-only tracks towards the bonded chip.

From the two-point measurement results of the second iteration, compared to the initial one, it can be concluded that having dedicated structures and designs that can allow for proper evaluation of the daisy-chain after the bonding process, is essential. As assumed in the beginning of this subchapter, the graphene tracks included in the initial two-point measurements (from the bonded chip to the electrodes, where the probing was done), had a lot of influence on the results, and thus, when these are not being taken into account, the resistance drops significantly. Another important aspect that can be concluded from the second set of measurements is that having metal-only test pads and tracks (from the bonded chip to the test pads), reduces the resistance even further. However, in order to evaluate in more depth the resistance of individual stud bumps, without any influence from the contact resistances of the probes, four-point measurements had to be employed (Fig. 69).

This, together with the daisy-chain topology of the current designs, gave the possibility to individually characterize 5 different Au stud bumps (illustrated by "Meas. x" in each plot). The major differences among the 5 bonds that could be evaluated were the location of those and the length of their connections to the test pads. Since these connections were relatively narrow (70 μm), differences in the measured values can be observed.

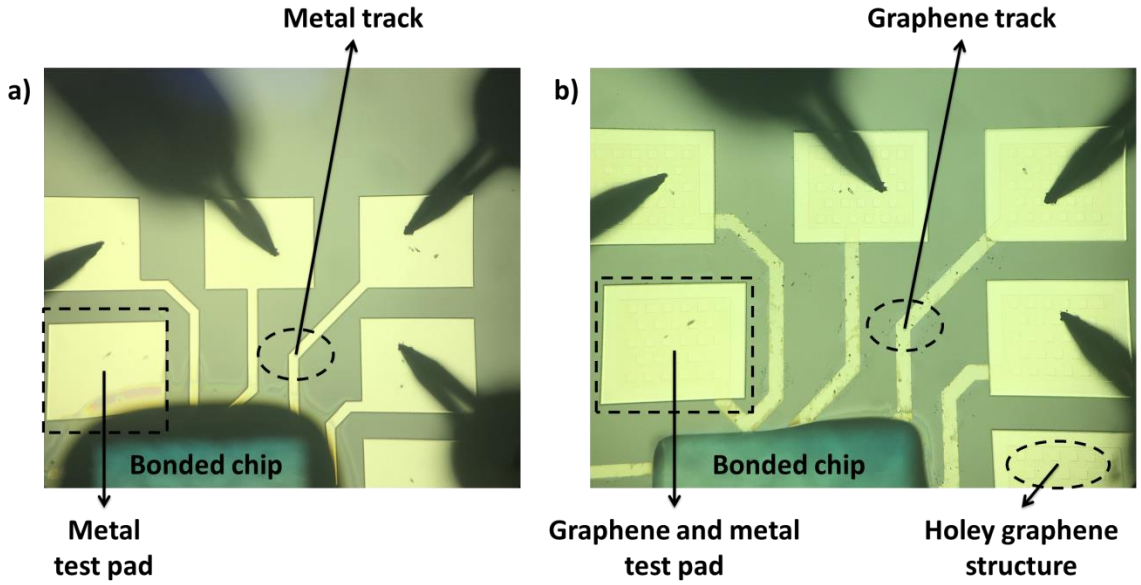

Fig. 69. Four-point measurement of dummy chips after the bonding process. In a), the metal test pads and tracks are shown. In b), the graphene and metal test pads, together with the graphene-only tracks are illustrated.

The results in Fig. 70, indicate resistance values in the range of mΩ for the chips bonded on substrates having metal test pads and tracks (substrate type 1 and 2 from Table 4). For the other chips, bonded on substrates having graphene and metal test pads and graphene-only tracks (substrate types 3 and 4 from Table 4), the resistance values were slightly increased but still in the range of a few ohms, meaning that the graphene track from the test pads towards the chip influences the final measured value. Moreover, calculating the average values for each of the four types of samples evaluated (Table 5), it can be concluded that the materials used during the fabrication process lead to significant differences in the resistive evaluation of the bonding process.

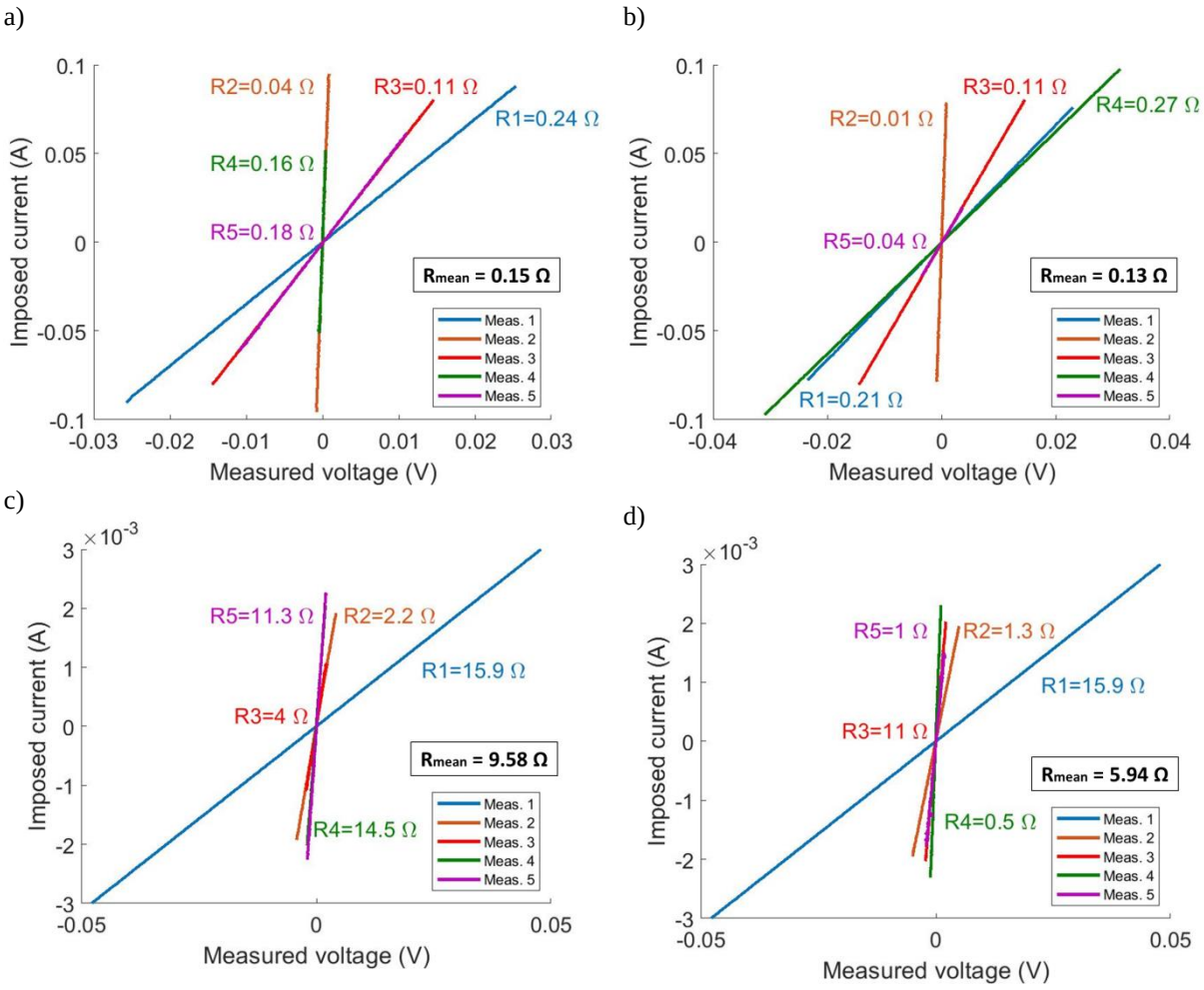

Fig. 70. Four-point measurements of dummy chips after the bonding process. In a) and b), substrate type 1 and 2 from Table x were used. In c) and d) sybstrate types 3 and 4 from Table x were used

Table 5. Average resistance values after four-point measurement evaluation of the bonding process.

Flip-chip bonding results on redesigned substrates	
SUBSTRATE TYPE	**AVERAGE RESISTANCE VALUE**
1	0.15 Ω
2	0.13 Ω
3	9.58 Ω
4	5.94 Ω

From these results it can be concluded that even if the contact resistances do not play a role in the final measurements, the stack of materials used for the substrate is essential.

4. 4. Optical transmittance

The intended use of both passive and active devices is for spinal cord monitoring of the stimulated area, during optogenetic activation of the cells. Therefore, transparency constitutes a key aspect for the project. Although having as few layers of graphene as possible leads to an increase in transparency (as the absorption rate for a monolayer is 2.3 % [34]) and conductivity, mechanical stability of graphene is extremely important. Therefore, having a monolayer graphene electrode exposed to the harsh environment of the body might be too fragile and potentially not survive from the mechanical point of view. Moreover, using CVD as means of

graphene growth makes it rather difficult to develop monolayer graphene structures. Generally this is being done using transfer methods which, in turn, are neither scalable, nor 100% reproducible.

To investigate the level of transparency of the final device, optical transmittance measurements were conducted. Structures comprising of graphene and one PDMS layer, as well as just a PDMS layer were measured and compared. To be able to estimate the transmittance rate of graphene-only, to the results measured on the sample comprising of graphene and PDMS, the contribution of PDMS was added.

As illustrated in Fig. 71, for a graphene structure, the transmittance rate is ~ 78.3 % at 500 nm wavelength, after the ~3 % contribution of PDMS was added to the measured values. This leads to an absorption rate of 21.7 % for the evaluated structure. As shown by Mak et al., in 2008 [34], the absorption rate for a monolayer graphene structure is 2.3 %. From this, it can be concluded that for the structure used in the present project, an approximate number of 10 layers of graphene were grown (Table 6).

Table 6. Optical transmittance employed to measure the number of graphene layers of a graphene-on-PDMS structure.

Optical transmittance		
Known values (graphene monolayer)	**Measured values (at 550 nm wavelength)**	**Number of graphene layers**
-> **2.3 %** absorption rate ($\%\boldsymbol{A_{monolayer}}$) [34]	-> **78.3 %** transmittance rate ($\%\boldsymbol{T_{measured}}$) -> **21.7 %** absorption rate ($\%\boldsymbol{A_{measured}}$)	$N_{layer} = \frac{\%A_{measured}}{\%A_{monolayer}} = \frac{21.7}{2.3} = \sim\mathbf{10}\ \boldsymbol{layers}$

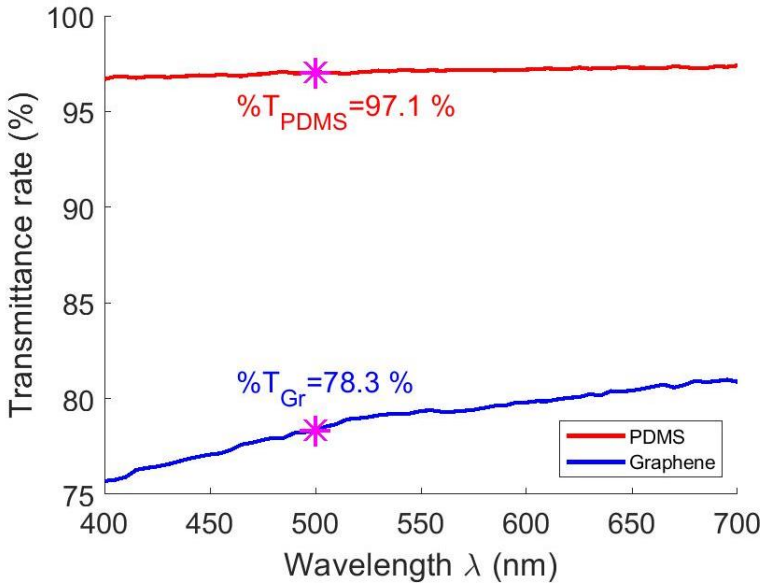

Fig. 71. Optical transmittance measurements for a graphene-on-PDMS structure.

4. 5. Bending tests

As described in the previous chapters of this thesis, the implantation site for the microfabricated graphene-based spinal cord implant is the epidural space of mice. Besides the stringent requirements in terms of size, another important aspect is the mechanical stability of the prototype. As the implant will potentially be subjected to different types and degrees of movements, evaluating its mechanical properties is of great interest.

Therefore, bending tests, using metal rods with sizes ranging from 3 mm to 8 mm in diameter, have been employed. To quantify the effect of bending under different angles, two-point resistive measurements were performed before and after bending the structures and the results are shown in Fig. 72.

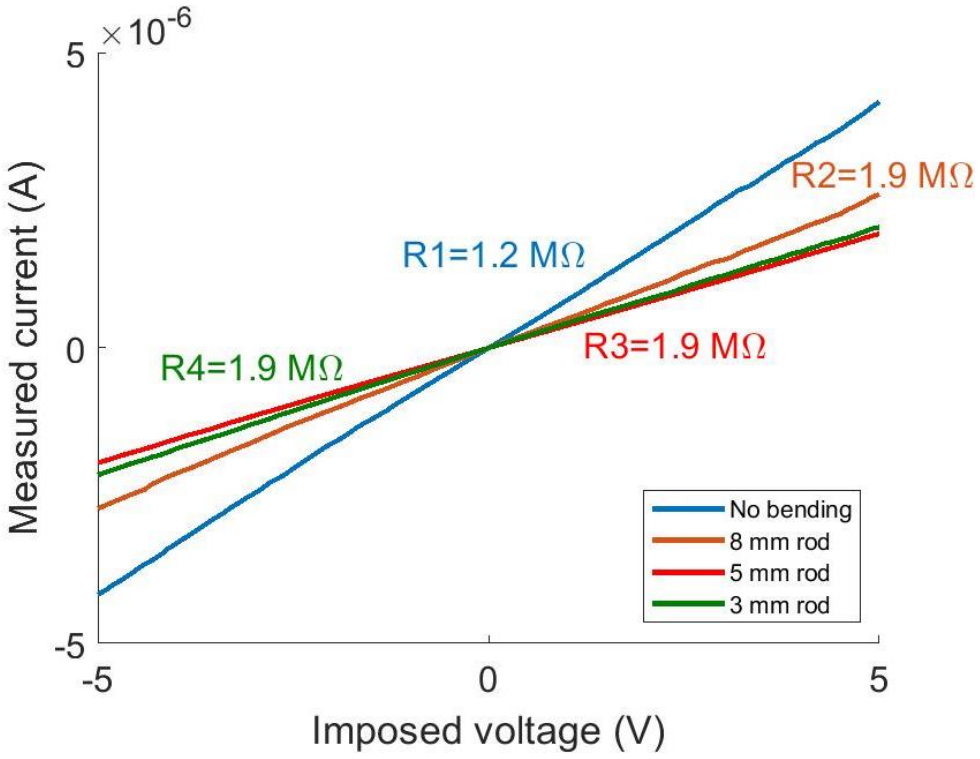

Fig. 72. Two-point measurement results before and after bending the graphene-based structure over different metal rods.

As presented in Chapter 3. 4 of this thesis, the masks used for the development of the implants included dedicated structures for bending tests that could be evaluated employing four-point resistive measurements and thus eliminating the influence of contact resistances over the measurements. However, because of their positioning, relatively close to the edges of the wafer, after employing DRIE process steps, these structures did not survive. To overcome this issue and still be able to evaluate the mechanical stability of the prototypes, a graphene-on-PDMS electrode array was used for bending tests. The measured part of the structure shown in Fig. 73, was a graphene track of ~ 2 cm in length and 70 μm in width.

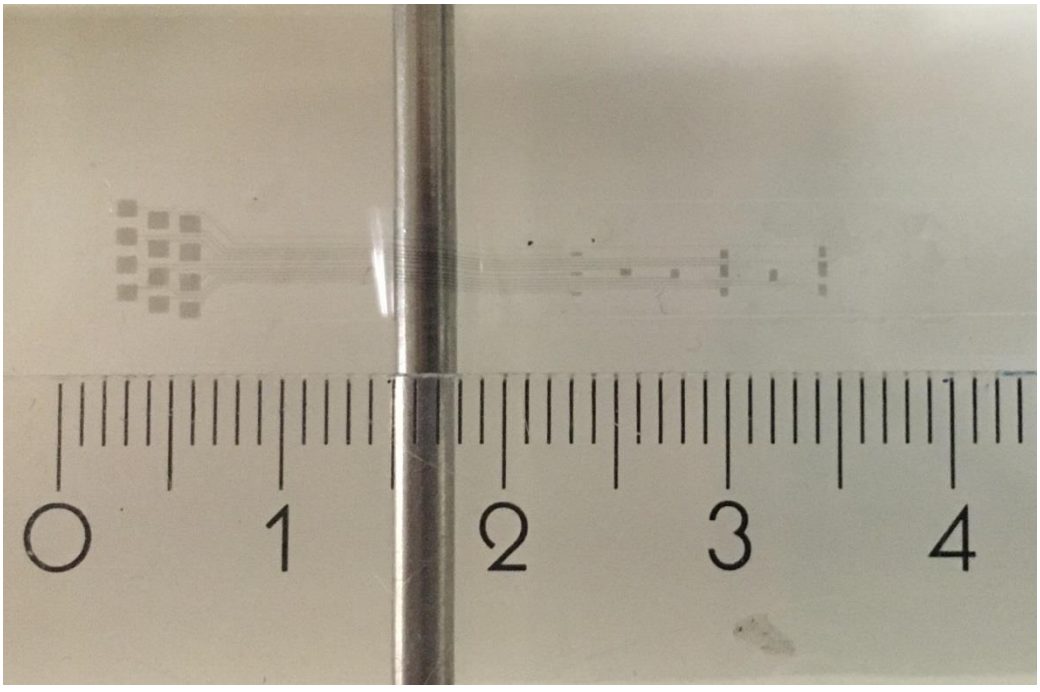

Fig. 73. Implant prototype (graphene-on-PDMS) released from the wafer and placed on a 3 mm bending rod.

Since there were no metal layers on top of graphene and the measurement setup was not tailored for such small samples, accurate probing of the structure represented a significant challenge. Due to this aspect and to the large length-to-width (L/W) ratio of the track under measurement, the resistance values are in the rage of MΩ and show a relative large sample-to-sample variation.

However, from the results shown, it can be concluded that the passive structures are able to conduct even after being bent over a metal rod with a diameter of 3 mm. Moreover, as shown in the previous sections of this thesis, if the application requires, the resistance could potentially be lowered either by leaving Mo on some parts of the graphene tracks or by depositing other metal layers on top of the graphene structures. However, the amount of metal present on graphene should be as low as possible and only over areas that are neither subjected to high mechanical strain, nor interfering with the light source used for optogenetic activation of the biological tissue.

4. 6. In-vitro (saline) experiments

The development of the envisioned graphene-based passive and active spinal cord implants requires an extensive microfabrication process and thus, investigating the graphene-based structures throughout the process is essential. Equally important is the evaluation of graphene in biological environments, over time. However, before conducting *in-vivo* experiments, *in-vitro* evaluation of the structures is compulsory. Therefore, after suspending the implants and removing the remaining oxide and Mo layers, thus having a graphene-on-PDMS structure, they were immersed in phosphate-buffered saline (PBS) solution for 24 hours and 7 days, respectively.

For the final implant structure, only the graphene electrodes will be exposed to the biological environment, the rest of the implant being encapsulated in PDMS. However, for the initial saline experiments, the complete graphene layer (electrodes, tracks and test pads) was exposed to saline solution. Evaluating the graphene layer before and after immersing it in PBS was performed by employing Raman spectroscopy and two-point electrical measurements.

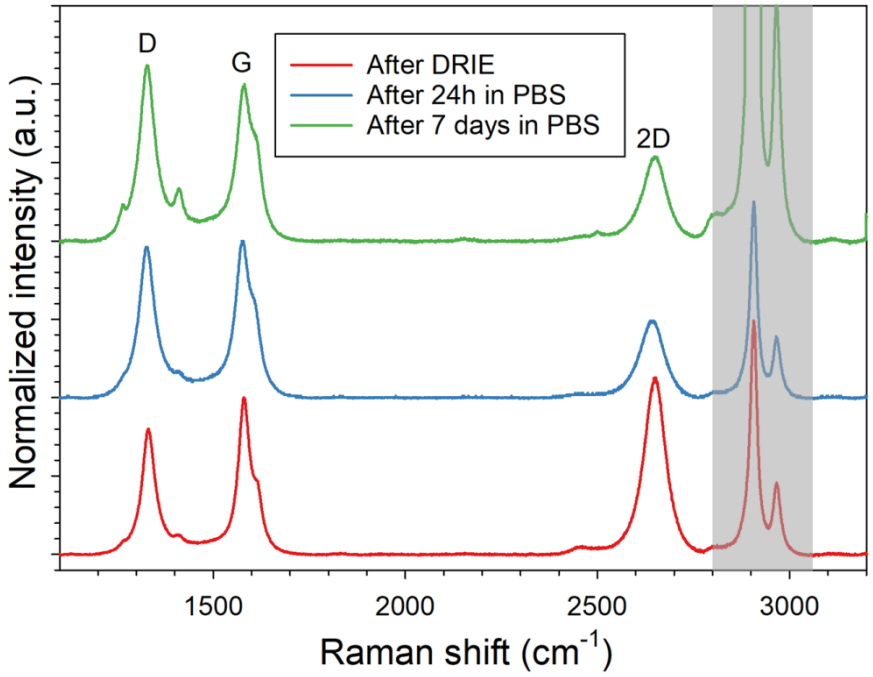

Fig. 74. Raman spectroscopy results after DRIE process and after immersing the graphene-on-PDMS structures in PBS for 24 h and 7 days respectively. The grey area represents the PDMS Raman signal.

In Fig. 74, the Raman spectra after immersing the structures in PBS, in comparison to the Raman spectra performed after suspending the implants is shown. From the results it can be concluded that there was no critical damage present on the graphene layer after the suspension process. However, after immersing the samples in PBS, the D peak, indicating the amount of defects present, slightly increases. Yet, the width of the peak remains the same, indicating that the size of graphene defects present within the layers did not change [66]. Therefore, it cannot be concluded that graphene deteriorates over time in PBS solution, since the increase in amplitude of the D peaks could also be caused by surface contamination of the graphene layer with different ions and particles from the saline solution or absorption of different molecules on its surface. The grey area represents the influence of PDMS over the Raman spectra.

Apart from Raman spectroscopy evaluation, the conductivity of graphene after being exposed to environments similar to the biological tissue is of great importance. To this end, two-point measurements over graphene tracks of 1 mm in length and 70 μm in width were employed (Fig. 75).

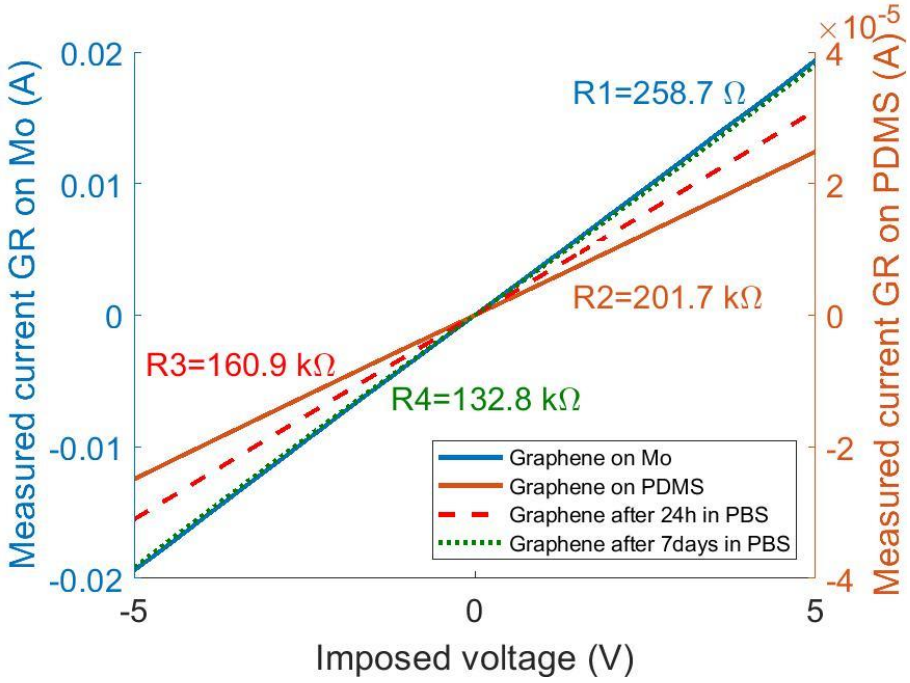

Fig. 75. Two-point electrical evaluation of graphene structures after the CVD process and after immersing the structures in PBS.

As illustrated in one of the previous sections of this chapter, a significant difference in resistance values is observed after removing the Mo layer on which graphene has been grown. This originates from the fact that the resistance of Mo is significantly lower than that of graphene. However, Fig. 75, illustrates that the resistance of graphene remains relatively stable, in the range of kΩ, both after removing the Mo layer as well as after immersing the structures in PBS for 24 h and 7 days respectively. The observed differences are likely due to the inaccuracy of the two-point measurements. However, from these preliminary results it can be concluded that graphene does not appear to deteriorate *in-vitro*.

4. 7. Characterization of electrodes

Throughout the previous sections of this thesis, graphene has been extensively evaluated since it is considered, for this project as the most important and challenging material. However, since graphene is being used for the development of electrode arrays, electrical characterization of these is required. Therefore, in parallel with the microfabrication process for the flexible passive and active implants, dedicated samples for electrode characterization were developed. These consist of the same structures, encapsulated in the first layer of PDMS and while kept on the Si rigid substrate, electrodes were opened, and the metal layers protecting the graphene electrodes, were removed, together with the Mo underneath to create exposed graphene-only electrodes with a diameter of 340 μm. For the tracks connecting the test pads with the graphene electrodes, the Mo catalyst was not removed for these samples. In order to connect the samples to the Autolab measurement setup for EIS and CV, wires were glued, using conductive glue, to each of the test pads that were in direct contact with an electrode as seen in Fig. 76. The setup used to measure the electrodes is shown in Fig. 77.

a)

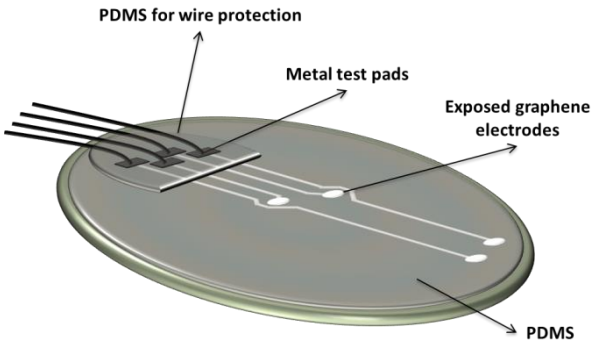

b)

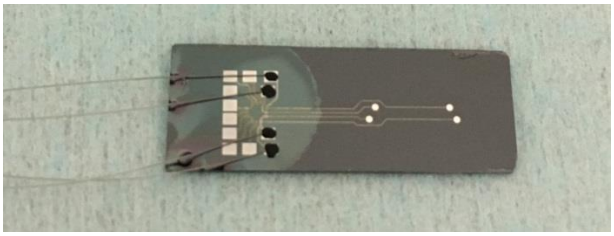

Fig. 76. Representation of the developed sample in a). Photograph of an actual sample used for EIS and CV measurements in b).

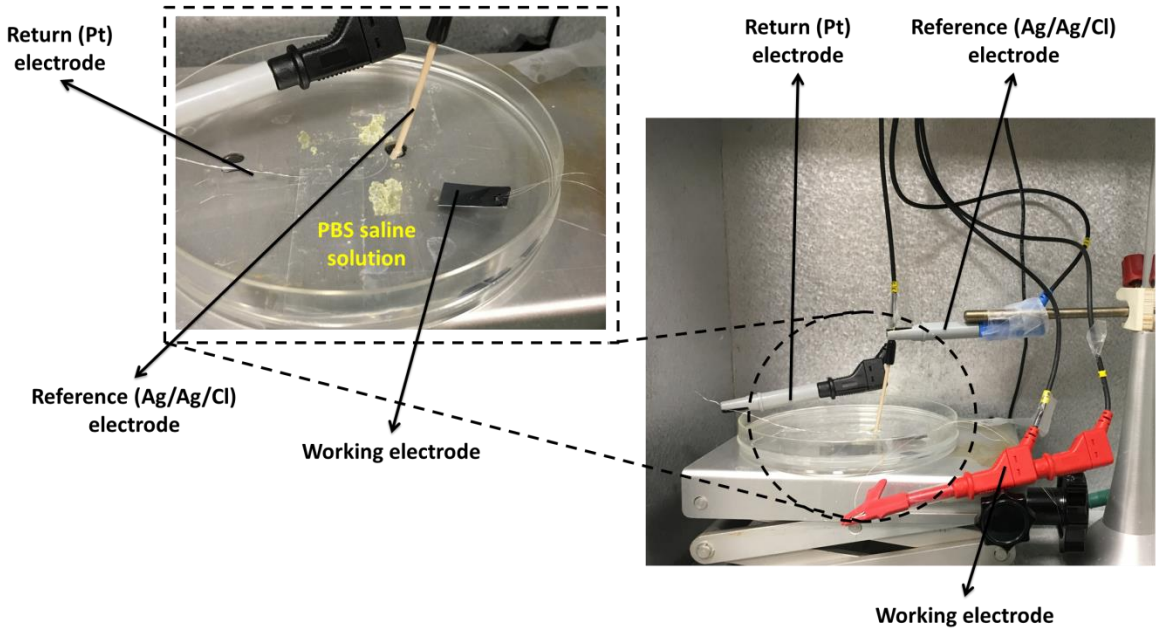

Fig. 77. Setup used for characterizing the electrodes. The working, return and reference electrode, immersed in PBS are illustrated.

4. 7. 1. Electrochemical impedance spectroscopy (EIS)

As described in section *3. 3. Characterization methods for the spinal cord implants* of this thesis, EIS is used to evaluate the impedance magnitude and phase of the electrodes over different frequency values in order to get a better understanding of both the electrode and tissue properties. According to the model used for the electrode-electrolyte interface, a typical capacitive behaviour should be observed at low frequencies, while becoming more resistive at high frequencies since the C_{el} in this case becomes a short circuit. In Fig. 78, the results obtained for two individual graphene electrodes ("Electrode 1" and "Electrode 2" are represented using Bode plots as impedance over frequency and phase over frequency. "Electrode1&2" indicate the results obtained for two shorted graphene electrodes and a Pt return electrode. As in this case, the two electrodes are in parallel, the value of the impedance decreases, as expected.

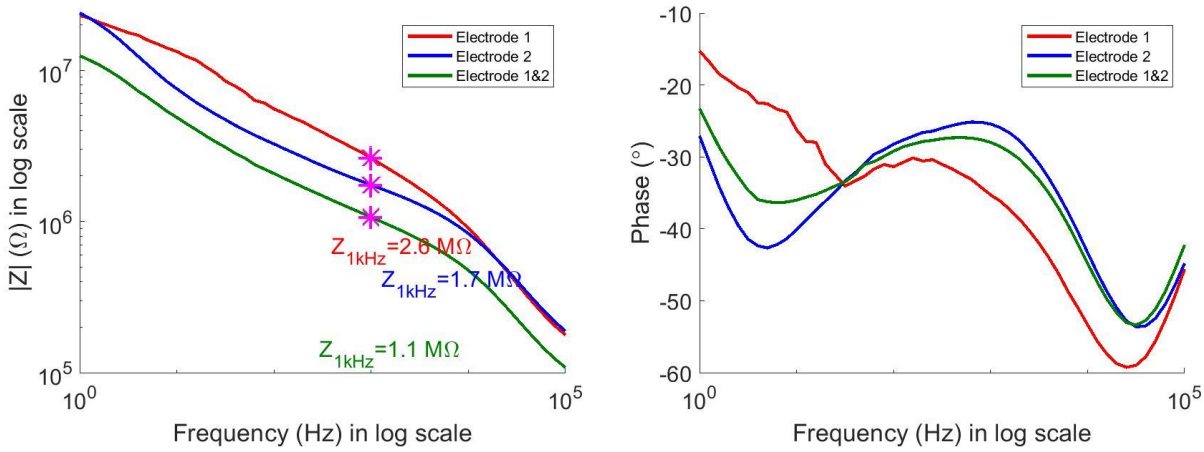

Fig. 78. Bode plots for impedance magnitude and phase with respect to frequency for two different electrodes.

From the results obtained, contradictory to what was expected, as the electrodes indicate a resistive behaviour at low frequencies and capacitive at high frequencies, it can only be concluded that there is a very high resistance influencing the measurement results. This resistance might only appear from the graphene on Mo tracks coming from the test pads towards the electrodes. However, as reported in section *4. 1*, the resistance of a graphene on Mo line (70 µm wide and 1 mm long) is ~250 Ω. Therefore this could not justify the MΩ impedance values observed during EIS. Considering that in this case the track is longer, a two-point measurement, on a new sample, from test pad to electrode was conducted in order to see if the length of the track influences the value of the resistance such that the impedance measurements indicate a completely opposite behaviour than what was expected. The results obtained are illustrated in Fig. 79 and as expected, although the resistance increases, ~600 Ω, due to the increase in length (7 mm in this case) of the measured track, it is still not large enough to explain the behaviour of the electrodes.

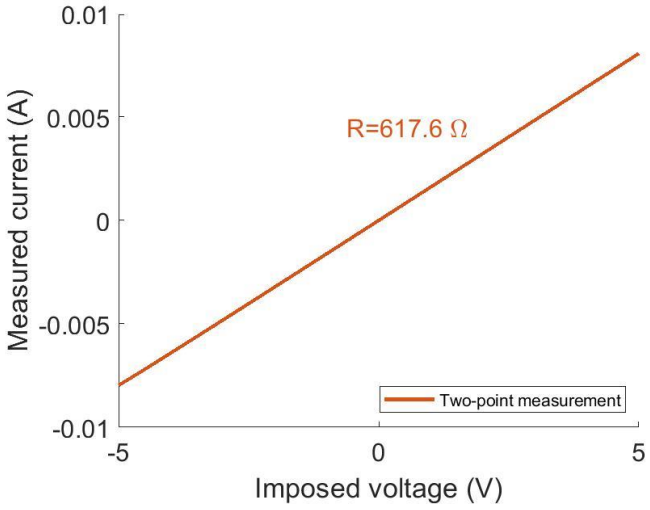

Fig. 79. Two-point measurement for a 7 mm long graphene on Mo track.

After visual inspection of the samples, it has been observed that the graphene on Mo tracks broke (Fig. 80) during the etching processes of the metal layers. Although unexpected, it confirmed the electrochemical results observed.

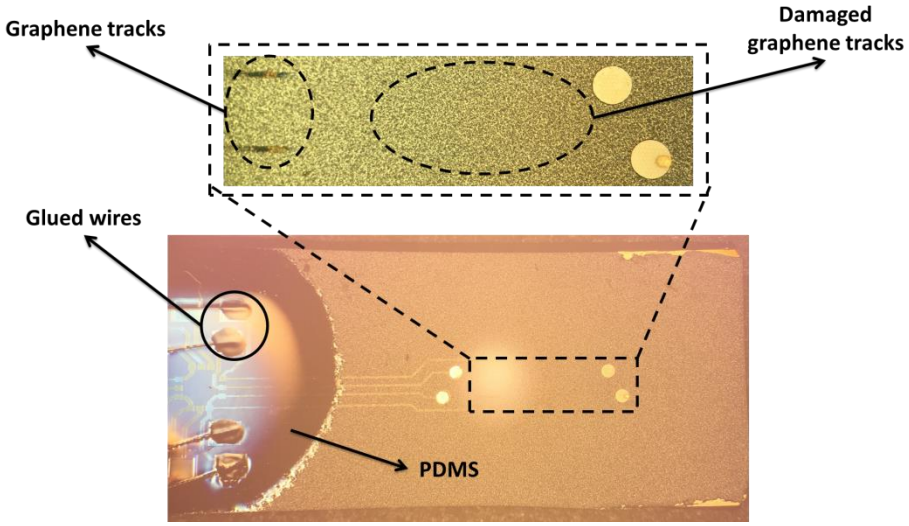

Fig. 80. Sample used for EIS and CV with graphene tracks damaged.

To further confirm that the EIS results are due to the failure in the etching process, 3 types of new samples were created, as shown in Fig. 81. The difference among them consisted in the structure of the electrodes. For the first type, the electrodes consisted of graphene on Mo encapsulated in the protective metal layer stack (Ti and Al) (Fig. 81 a). The second category (Fig. 81 b) consisted of electrodes without any metal on top of graphene but with the Mo catalyst still underneath while the third, consisted of graphene-only electrodes (Fig. 81 c). From Fig. 81 b) and c), a clear difference in colour can be observed. Graphene, when not having the metal catalyst underneath, shows a grey colour, whereas graphene on Mo has a more metallic colour, as seen in Fig. 81 b).

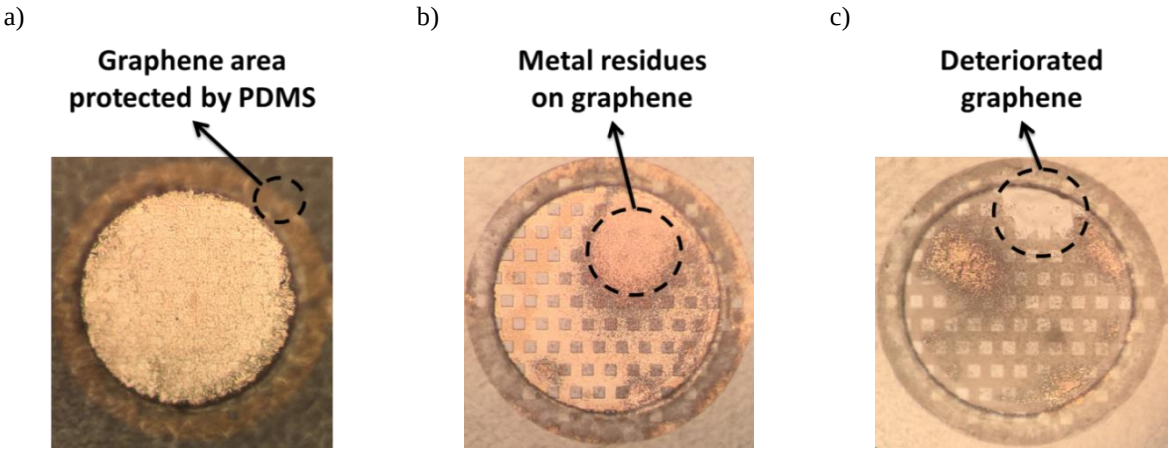

Fig. 81. Electrode samples used for EIS and CV measurements. In a), a graphene on Mo electrode encapsulated in a protective stack of metal layers. In b), a graphene on Mo electrode while in c), a graphene-only electrode.

In Fig. 82, the results obtained for the EIS measurements performed on all three electrode samples are illustrated. It can be seen that in all cases the electrode behaviour is as expected, mainly capacitive at low frequencies and resistive at high frequencies. However, for graphene-only electrodes it can be noticed that the impedance drops significantly compared to the other two electrodes, showing impedance values of 8.2 kΩ at 1kHz, similar to what has been previously reported in the literature [67].

The assumption in this case is that graphene has a relatively low contact resistance with liquids compared to metals [68]. Moreover, since the layer of graphene is in direct contact with the oxide underneath, being kept in place by weak forces, the PBS molecules might have also formed an interface between graphene and oxide, thus providing more contact area. Apart from this, the metal layer that is on top of graphene, for the first type of electrodes, presents a native oxide layer which might also lead to an increase in the impedance values.

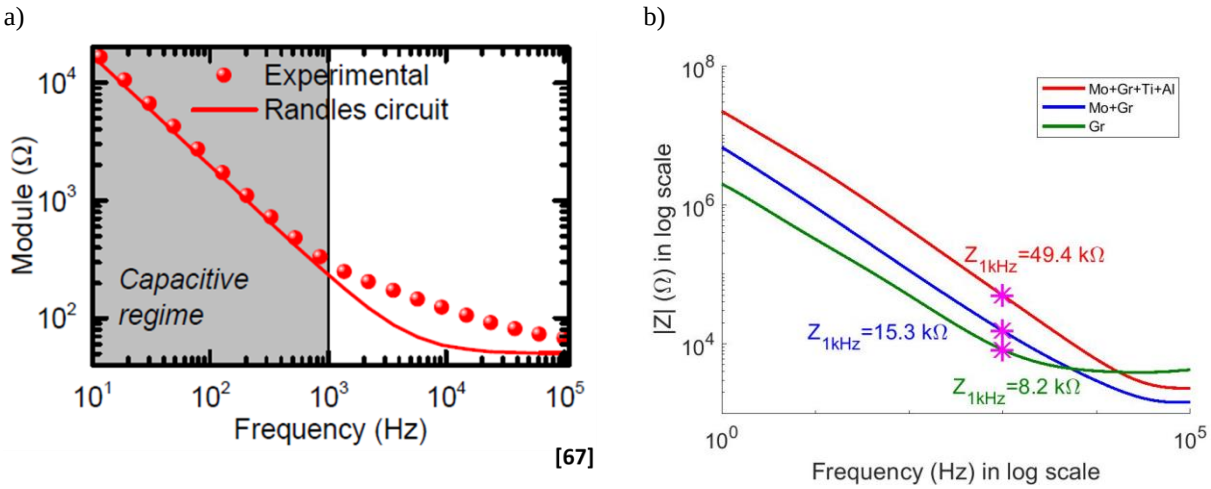

Fig. 82. Bode plots for impedance magnitude reported in literature a) [67] and measured for this project b).

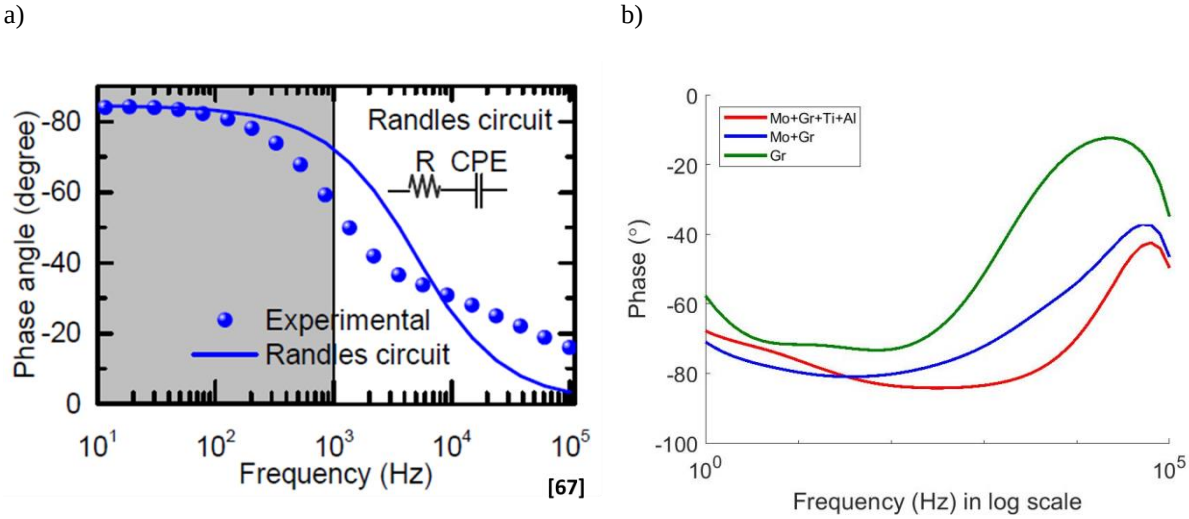

Fig. 83. Bode plots for impedance phase reported in literature a) [67] and measured for this project b).

4. 7. 2. Cyclic voltammetry (CV)

Together with EIS, CV measurements were performed in order to evaluate the voltage range (water window) in which the electrodes do not present any Faradaic reactions and therefore can be used safely. Moreover, from the CV plot, by integrating the area between the CV curves, the CSC for the graphene electrodes can be evaluated. In Fig. 84 b the results obtained for the CV measurements corresponding to the damaged samples are illustrated. It can be noticed that also from the CV curve, the behaviour of the electrode is mostly resistive. However, in Fig. 84 c the CV curve for the graphene electrode illustrated in Fig. 81 c are shown. It can be noticed from the plot that the CSC is relatively low for graphene electrodes, as mentioned also in [69]. However, it should be noted that these results and the electrode characterization procedure have to be further investigated for more reliable results. Due to lack of time, the ones presented in this thesis are only preliminary data.

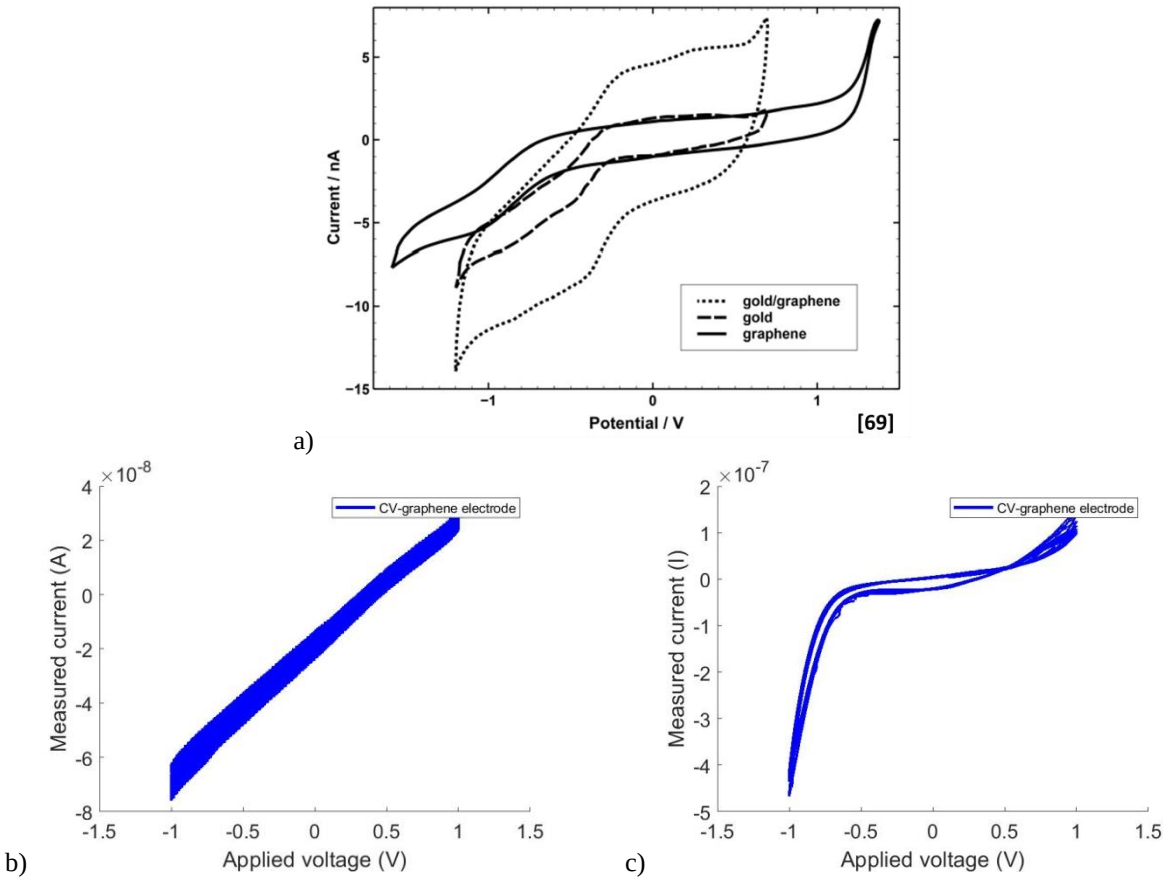

Fig. 84. CV evaluation of graphene electrodes.In a), what has been reported in the literature. In b), the samples with broken tracks were evaluated. In c), the new sample with graphene-only electrodes was evaluated.

5. Conclusions and future work

5. 1. Conclusions

The topic of spinal cord stimulation has been gaining a lot of interest in the neuroscience community. Understanding the mechanisms that occur while stimulating the neuronal circuitry within the spinal cord is still unclear. Therefore, there is a high need for developing platforms: implantable devices that could ease the experimental procedures but also lead to more conclusive results. Moreover, new methods of exciting the neuronal tissue are under investigation and one that has been proven to be very promising is optogenetics. By means of light, specific types of cells, previously genetically modified to be made sensitive to light, are activated, and thus the stimulation effects can be easily correlated with the location and type of cell that was activated. Moreover, recording the electrical activity of the cells during optogenetic stimulation, at the same location, could provide better insight into the mechanisms of action. However, tailored technologies that could combine both are limited. To circumvent this, the use of transparent and conductive materials throughout the development process of such devices is of great importance.

Therefore, the objective of this thesis was to develop, by means of microfabrication, fully transparent, graphene-based passive and active spinal cord implants. Throughout the chapters of this thesis it has been demonstrated that spinal cord implants can be developed only by means of microfabrication and that graphene can be used both as a conductive as well as a transparent material for the development of optogenetic compatible spinal cord implants. Moreover, system integration of test chips with the passive array of electrodes has been proven to be successful and thus providing, apart from passive devices, active graphene-based spinal cord implants.

The novelty of this project lies in different aspects. First, the targeted spinal cord applications as these impose serious limitations. Therefore, the materials used had to be carefully chosen such that they could fulfil the strict requirements, mainly in terms of transparency, conductivity and high flexibility of the envisioned spinal cord implant. Apart from that, since having just a passive spinal cord implant is not sufficient for long-term evaluation, active devices represent the ultimate goal. To this end, hybrid system integration techniques were employed to bring the active components, ideally in the form of ASICs, on the same area as the electrode arrays and thus creating a compact and scalable active spinal cord implant. Lastly, the combination of microfabrication process steps used for the development of the implants represented a novelty by itself, yet, also a challenge.

Throughout the iterations of the process, issues had to be overcome and the process had to be further improved. Initially, in order to validate the process flow, old masks, designed by G. K. Wardhana, were used. However, problems such as delamination of the metal layer from graphene together with the lack of dedicated structures for flip-chip bonding processes and their evaluation, lead to the redesign of all process masks. Significant improvements were seen afterwards and these results have been presented in Chapter 4 of this thesis. The adhesion problem was successfully solved and the flip-chip bonding processes could accurately be evaluated, indicating resistance values ranging from 10 mΩ up to 16 Ω, depending on the substrate structure, as illustrated in section *4.3* of this thesis. Also, the release of the final implants from the rigid Si substrate was successfully achieved.

The microfabrication aspect represented most of this thesis. However, intermediate evaluations and measurements were equally important to establish and validate the most critical processing aspects. Therefore, methods such as Raman spectroscopy, two- and four-point electrical measurements were extensively used to evaluate the quality of the graphene layer throughout the process. Raman spectroscopy evaluation indicated that graphene does not deteriorate throughout the microfabrication process, judging from the similar I_D/I_G values before (~0.9) and after (~0.8 – 0.9, depending on the location measured) suspending the implants. In terms of resistances, it has been proven that the metal catalyst on top of which graphene was grown, had a dominant influence on the measurements (R = ~250 Ω for a 70µm wide and 1 mm long graphene on Mo track and R = ~ 250 kΩ for a 70µm wide and 1 mm long graphene track on PDMS).

Moreover, since the implant was intended for use in optogenetics-related applications, the optical transmittance rate had to be investigated. From this it was concluded that for this process, ~10 layers of graphene are grown and their transmittance rate is ~78 %.

To estimate how fragile the graphene-based implant is, especially since the implantation location is subjected to different types and degrees of movements, bending tests were employed and it was shown that the structures can be bent down to 3 mm without presenting any critical damage, judging from the resistance measured (1.2 MΩ before and 1.9 MΩ after the bending procedures being employed). Apart from this, the electrodes of such an implant had to be evaluated. Therefore, preliminary EIS and CV measurements were performed and it was concluded that the behaviour of the electrodes is as expected over a certain frequency

range. Moreover, the impedance measurements indicated results comparable to literature for graphene electrodes (8.2 kΩ at 1kHz). However, in order to draw clear conclusions regarding their performance, more evaluation is needed.

5. 2. Future work

This thesis successfully reported the development of a stable and reproducible microfabrication process flow for passive and active graphene-based, flexible spinal cord implants. However, there are several aspects that need to either be further investigated or changed. As shown in section *4. 2* of this thesis, after suspending the final implants, electrical measurements could not be performed as the structures were damaged after the DRIE process, due to the high compressive stress induced by TEOS oxide. Therefore, in order to develop high quality structures, that could survive the entire process, the oxide layer on top of which the structures are developed should be changed with one that does not induce tensile nor compressive stress to the structure on top.

The development of graphene-based spinal cord implants has been proven to be challenging from many perspectives. Among all, perhaps the most challenging step in the process flow is the suspension of the implants while still achieving high yield and quality. Apart from the stress induced by the oxide layer which damaged the structures in various places, removing the oxide and Mo layer lead to problems as well, mainly in the electrodes and test pads areas which broke after wet etching steps. This is due to the fact that on the frontside, those areas were not protected by any material and thus they were very fragile. Moreover, as described previously, BHF, used for wet etching of the oxide layer, etches also Ti and thus, the metal areas were completely removed leaving a thin layer of graphene fully suspended which eventually broke due to the fragility of the structure. Therefore, to overcome this in the future, it is highly recommended that the openings in the PDMS layer for the electrodes and test pads are performed at the end of the fabrication process, after the second layer of encapsulation has been applied. This will provide enough mechanical support for the structures both during the suspension of the implant but also while creating the opening in the polymer layer.

Regarding the development of active implants and the system integration of chips with the passive, graphene-based structures, several aspects should be underlined. First of all, it is highly recommended that the dummy chips are developed on thin Si wafers or that they are thinned down, once fabricated. This reduces the risk that the encapsulation layer does not provide full coverage of the structures, due to the relatively large step height between the substrate and the chip after the bonding process. Apart from that, it would be interesting to investigate the monolithic approach for integrating the active components with the passive structure. In this way, there will be no need for developing separate chips and later integrating them. However, this requires the development of new lithography masks.

Apart from improving the microfabrication process in order to develop a stable and completely reproducible process flow, it is important to understand the performance of the final implants. Therefore, electrodes have to be thoroughly characterized and this thesis only reported preliminary results in terms of EIS and CV for graphene-based electrodes. Apart from that, in order to estimate the amount of charge that can safely be delivered to the tissue using a typical biphasic current stimulation, voltage transient recordings are needed. For such measurements, a three-electrode setup is needed, similar to the one used for CV and EIS. However, in this case, the implant has to be connected to a stimulator that can inject the biphasic current pulses between the working and return electrode, while the voltage with respect to the reference electrode is evaluated. Moreover, since the envisioned prototype should be used to record the electrical activity of the cells during optogenetic stimulation, it is important to characterize the electrodes also as recording electrodes.

In section *4. 6* of this thesis, saline-based experiments have been reported. These consisted of immersing a graphene-on-PDMS structure in saline for 24 hours and one week respectively and evaluate the quality of graphene afterwards. It has been shown that graphene does not present any critical damage after these experiments. However, the evaluation was done at room temperature. The reported results might change if temperature is also considered. Moreover, in order to better understand and evaluate the graphene performance of the spinal cord implant in a real scenario, together with temperature, voltage transient recordings should also be employed. Thus, before performing any *in-vivo* evaluation of the fabricated prototypes, thorough *in-vitro* characterization has to be performed.

After performing an extensive *in-vitro* characterization and understanding the behaviour as well as the performance of the graphene-based spinal cord implants, animal experiments can be conducted. These types of experiments provide insight into the biological reactions that might occur after implantation of biomedical devices. As for this project different and unconventional materials have been used, it is of great importance to understand how these interact with the biological tissue. Therefore, biocompatibility tests should be conducted. These usually consist of two groups of subjects, one the control and the second, the experimental group. For the

control group, generally the implantation location is defined while for the experimental group, the actual device is implanted inside the body. Depending on how the protocol is defined, subjects from both groups are evaluated over time, mainly in terms of tissue response. Another type of experiment is the acute experiment which provides insight into the anatomical and biological behaviour of the subject while the device is being operated. Usually, these experiments are conducted over short periods of time in order to evaluate the performance of the device while inside the body. However, since implantable devices are meant to be inside and fully operate for longer periods of time, chronic experiments should be employed. These provide insight into both the response of the subject as well as the performance of the device over longer periods of time.

REFERENCES

[1] B. Greenstein and A. Greenstein, "Anatomy," in *Color Atlas of Neuroscience: neuroanatomy and neurophysiology*.: Ed. Stuttgart: Georg Thieme Verlag, 2000, pp. 2-53.

[2] R. L. Drake, A. W. Vogl, and A. W. M. Mitchell, "The body," in *Gray's Basic Anatomy*.: Ed. Philadelphia: Elsevier Churchill Livingstone, 2012, pp. 1-30.

[3] iStock. [Online]. www.istockphoto.com

[4] K. Kayalioglu, "The vertebral column and spinal meanings," in *The Spinal Cord: A Christopher and Dana Reeve foundation text and atlas*.: Ed. London: Academic Press, 2009, pp. 17-36.

[5] G. Sengul and C. Watson, "Spinal Cord," in *The Mouse Nervous System*.: Academic Press, 2012, pp. 424-458.

[6] F. M. Maynard, Jr et al., "International Standards for Neurological and Functional Classification of Spinal Cord Injury," *Spinal Cord*, vol. 35, pp. 226-274, 1997.

[7] O. Kiehn, "Decoding the organization of spinal circuits that control locomotion," *Nature Reviews Neuroscience*, vol. 17, pp. 224-238, 2016.

[8] V. Pikov, "Spinal plasticity," in *Neuroprosthetics: Theory and Practice*.: Ed. Singapore: World Scientific Publishing Co. Pte. Ltd., 2007, pp. 302-316.

[9] V. R. Edgerton, N. J. K. Tillakaratne, A. J. Bigbee, R. D. de Leon, and R. R Roy, "Plasticity of the spinal neural circuitry after injury," *Annual Review of Neuroscience*, vol. 27, pp. 145-167, 2004.

[10] (2013) World Health Organization. [Online]. https://www.who.int/news-room/fact-sheets/detail/spinal-cord-injury

[11] American Association of Neurological Surgeons. [Online]. https://www.aans.org/Patients/Neurosurgical-Conditions-and-Treatments/Spinal-Cord-Injury

[12] Yu. P. Gerasimenko, A. N. Makarovskii, and O. A. Nikitin, "Control of Locomotor Activity in Humans and Animals in the Absence of Supraspinal Influences," *Neuroscience and Behavioral Physiology*, vol. 32, no. 4, 2002.

[13] V. R. Edgerton and R. R. Roy, "Activity-Dependent Plasticity of Spinal Locomotion: Implications for Sensory Processing," *Exercise and sport sciences review*, vol. 37, no. 4, pp. 171-178, 2009.

[14] K. L. Montgomery, M. I. Shrivats, A. J. Christensen, K. Deisseroth, and S. L. Delp, "Beyond the brain: optogenetic control in the spinal cord and peripheral nervous system," *Science Translational Medicine*, vol. 8, no. 337, p. 337rv5, 2016.

[15] H. Zhao, "Recent progress of development of optogenetic implantable neural probes," *International Journal of Molecular Sciences*, vol. 18, no. 8, 2017.

[16] R. van den Brand et al., "Restoring voluntary control of locomotion after paralyzing spinal cord injury," *Science*, vol. 336, no. 6085, pp. 1182-1185, 2012.

[17] L. Jacques and M. Safaee, "Epidural spinal cord stimulation for recovery from spinal cord injury: its place in therapy," *Journal of Neurorestoratology*, vol. 4, pp. 63-67, 2016.

[18] A. N. Dalrymple and V. K. Mushahwar, "Stimulation of the Spinal Cord for the Control of Walking: Theory and Practice," in *Neuroprosthetics*.: World Scientific, 2017, pp. 811-849.

[19] R. Herman, J. He, S. D'Luzansky, W. Willis, and S. Dilli, "Spinal cord stimulation facilities functional walking in a chronic, incomplete spinal cord injured," *Spinal Cord*, vol. 40, no. 2, pp. 65-68, 2002.

[20] S. Harkema et al., "Effect of epidural stimulation of the lumbosacral spinal cord on voluntary movement, standing, and assisted stepping after motor complete paraplegia: a case study," *Lancet*, vol. 377, no. 9781, pp. 1938-1947, 2011.

[21] C. A. Angeli, V. R. Edgerton, Y. P. Gerasimenko, and S. J. Harkema, "Altering spinal cord excitability enables voluntary movements after chronic complete paralysis in humans," *Brain*, vol. 137, no. 5, pp. 1394-1409, 2014.

[22] Y. LeChasseur et al., "A microprobe for parallel optical and electrical recordings from single neurons in vivo," *Nature Methods*, vol. 8, pp. 319-325, 2011.

[23] E. Stark, T. Koos, and T. Buzsaki, "Diode probes for spatiotemporal optical control of multiple neurons in freely moving animals," *Journal of Neurophysiology*, vol. 108, no. 1, pp. 349-363, 2012.

[24] T. I. Kim et al., "Injectable, cellular-scale optoelectronics with applications for wireless optogenetics," *Science*, vol. 340, no. 6129, pp. 211-216, 2013.

[25] W. J. Alilain et al., "Light-induced rescue of breathing after spinal cord injury," *Journal of Neuroscience*, vol. 28, no. 46, pp. 11862-11870, 2008.

[26] L. Borgius, K. Dougherty, and O. Kiehn, "Activation of groups of excitatory neurons in the mammalian spinal cord or hindbrain evokes locomotion," *Nature Neuroscience*, vol. 13, no. 2, pp. 246-252, 2010.

[27] P. Gad et al., "Development of a multi-electrode array for spinal cord epidural stimulation to facilitate stepping and standing after a complete spinal cord injury in adult rats," *Journal of Neuroengineering and Rehabilitation*, vol. 10, no. 2, 2013.

[28] I. R. Minev et al., "Electronic dura mater for long-term multimodal neural interfaces," *Science*, vol. 347, no. 6218, pp. 159-163, 2015.

[29] T. Stieglitz, M. Schuetter, and K. P. Koch, "Implantable biomedical microsystems for neural prostheses," *IEEE Engineering in Medicine and Biology Magazine*, vol. 24, no. 5, pp. 58-65, 2005.

[30] L. Guo et al., "A PDMS-based integrated stretchable microelectrode array (isMEA) for neural and muscular surface interfacing," *IEEE Transactions on Biomedical Circuits and Systems*, vol. 7, no. 1, pp. 1-10, 2013.

[31] V. Giagka, A. Demosthenous, and N. Donaldson, "Flexible active electrode arrays with ASICs that fit inside the rat's spinal canal," *Biomedical Microdevices*, vol. 17, no. 6, pp. 106-118, 2015.

[32] P. Ledochowitsch, E. Olivero, T. Blanche, and M. M. Maharbiz, "A transparent μECoG array for simultaneous recording and optogenetic stimulation," *Conference proceedings: Anual International Conference of the IEEE Engineering in Medicine and Biology Society*, pp. 2937-2940, 2011.

[33] W. F. Quiros-Solano, N. Gaio, C. Silvestri, G. Pandraud, and P. M. Sarro, "PEDOT:PSS: A Conductive and Flexible Polymer for Sensor Integration in Organ-on-Chip Platforms," *Procedia Engineering*, vol. 168, pp. 1184-1187, 2016.

[34] K. F. Mak et al., "Measurement of the optical conductivity of graphene," *Physical Review Letters*, vol. 101, no. 19, pp. 2-5, 2008.

[35] S. Ye et al., "Thickness-dependent strain effect on the deformation of the graphene-encapsulated Au nanoparticles," *Journal of Nanomaterials*, vol. 4, pp. 1-6, 2014.

[36] J-Y. Hong, W. Kim, D. Choi, J. Kong, and H. S. Park, "Omnidirectionally strechable and transparent graphene electrodes," *ACS Nano*, vol. 10, no. 10, pp. 9446-9455, 2016.

[37] C. Galiotis et al., "Mechanical Properties of Graphenes and Graphene-Polymer Nanocomposites," *15th European Conference on Composite Materials*, pp. 8-10, 2012.

[38] K. S. Novoselov et al., "Electric field effect in atomically thin carbon films," *Science*, vol. 306, no. 5696, pp. 666-669, 2004.

[39] Y. Zhang, L. Zhang, and C. Zhou, "Review of chemical vapor deposition of graphene and related applications," *Acc. Chem. Res*, vol. 46, no. 10, pp. 2329-2339, 2013.

[40] A. C. Vilatela, R. S. Weatherup, P. Braeuninger-Weimer, S. Caneva, and S. Hofmann, "Towards a general growth model for graphene CVD on transition metal catalysts," *Nanoscale*, vol. 8, pp. 2149-2158, 2016.

[41] Y. Wu et al., "Synthesis of large-area graphene on molybdenum foils by chemical vapor deposition," *Carbon*, vol. 50, no. 14, pp. 5226-5231, 2012.

[42] American elements. [Online]. https://www.americanelements.com/

[43] S. Vollebregt et al., "A transfer-free wafer-scale CVD graphene fabrication process for MEMS/NEMS sensors," *Proc. IEEE MEMS*, pp. 17-20, 2016.

[44] D. Bitounis, H. Ali-Boucetta, B. H. Hong, D-H. Min, and K. Kostarelos, "Prospects and challenges of graphene in biomedical applications," *Advanced Materials*, vol. 25, no. 16, 2013.

[45] S. Syama and P. V. Mohanan, "Safety and biocompatibility of graphene : A new generation nanomaterial for biomedical application," *International Journal of Biological Macromolecules*, vol. 86, pp. 546-555, 2016.

[46] D-W. Park et al., "Graphene-based carbon-layered electrode array technology for neural imaging and optogenetic applications," *Nature Communications*, vol. 5, no. 5258, pp. 1-11, 2014.

[47] D-W. Park et al., "Electrical neural stimulation and simultaneous in vivo monitoring with transparent graphene electrode arrays implanted in GCaMP6f mice," *ACS Nano*, vol. 12, no. 1, pp. 148-157, 2018.

[48] C. Hassler, T. Boretius, and T. Stieglitz, "Polymers for neural implants," *Journal of Polymer Science: Part B: Polymer Physics*, vol. 49, no. 1, pp. 18-33, 2011.

[49] B. Hiebl et al., "In vivo assessment of tissue compatibility and functionality of a polyimide cuff electrode for recording afferent peripheral nerve signals," *Applied Cardiopulmonary Pathophysiology: ACP*, vol. 14, no. 4, pp. 212-219, 2010.

[50] J-M. Hsu et al., "Characterization of Parylene-C films as an encapsulation material for neural interface devices," *Proceedings Third International Conference on Multi-Material Micro Manufacture*, 2007.

[51] D. S. Lee et al., "Comparison of in vivo biocompatibilities between Parylene-C and polydimethylsiloxane for implantable microelectronic devices," *Bulletin of Materials Science*, vol. 36, no. 6, pp. 1127-1132, 2013.

[52] K. Scholten and E. Meng, "Materials for microfabricated implantable devices: a review," *Lab on a Chip*, vol. 15, no. 22, pp. 4256-4272, 2015.

[53] A. Zahid, B. Dai, R. Hong, and D. Zhang, "Optical properties study of silicone polymer PDMS substrate surfaces modified by plasma treatment Optical properties study of silicone polymer PDMS substrate surfaces modified by plasma treatment," *Materials Research Express*, vol. 4, no. 10.

[54] C. Alex and M. Kuo, "Poly(dimethylsiloxane," in *Polymer Data Handbook*.: Oxford University Press, 1999, pp. 411-435.

[55] S. Shi, *Effects of silicon oxides as substrates for graphene-based gas sensor*.: TU Delft, 2017.

[56] E. Watanabe, A. Conwill, D. Tsuya, and Y. Koide, "Low contact resistance metals for graphene based devices," *Diamond & Related Materials*, vol. 24, pp. 171-174, 2012.

[57] J. A. Robinson et al., "Contacting graphene," *Applied Physics Letters*, vol. 98, 2011.

[58] B. Mimoun, V. Henneken, A. Van der Horst, and R. Dekker, "Flex-to-rigid (F2R): A generic platform for the fabrication and assembly of flexible sensors for minimally invasive instruments," *IEEE Sensors Journal*, vol. 13, no. 10, pp. 3873-3882, 2013.

[59] M. S. Dresselhaus, A. Jorio, M. Hofmann, G. Dresselhaus, and R. Saito, "Perspectives on carbon nanotubes and graphene Raman spectroscopy," *Nano Letters*, vol. 10, pp. 751-758, 2010.

[60] Z. Jian et al., "Irradiation effects of graphene and thin layer graphite induced by swift heavy ions," *Chin. Phys. B*, vol. 24, no. 8, 2015.

[61] D. R. Merrill, M. Bikson, and J. G. R. Jefferys, "Electrical stimulation of excitable tissue: design of efficacious and safe protocols," *Journal of Neuroscience Methods*, vol. 141, pp. 171-198, 2005.

[62] P. T. Kissinger and W. R. Heineman, "Cyclic voltammetry," *Journal of Chemical Education*, vol. 60, no. 9, pp. 702-706, 1983.

[63] G. K. Wardhana, *A flexible transparent graphene electrode array for spinal cord stimulation in rats*.: TU Delft, 2019.

[64] Y. Y. Wang et al., "Raman studies of mnolayer graphene: the substrate effect," *J. Phys. Chem. C*, vol. 112, no. 29, pp. 10637-10640, 2008.

[65] M. Fretz, *Flip chip bonding technologies for hybrid integration*.: Universite de Neuchatel, 2009.

[66] E. F. Antunes, A. O. Lobo, E. J. Corat, and V. J. Trava-Airoldi, "Influence of diameter in the Raman spectra of aligned multi-walled carbon nanotubes," *Carbon*, vol. 45, no. 5, pp. 913-921, 2007.

[67] S. Drieschner et al., "Frequency response of electrolyte-gated graphene electrodes and transistors," *Journal of Physics D: Applied Physics*, vol. 50, 2017.

[68] Y. Lu et al., "Ultralow impedance graphene microelectrodes with high optical transparency for simultaneous deep two-photon imaging in transgenic mice," *Advanced Functional Materials*, vol. 28, 2018.

[69] B. Korbitzer, P. Kraus, S. Belle, J. J. Schneider, and C. Thielemann, "Electrochemical characterization of graphene microelectrodes for biological applications," *ChemNanoMat*, vol. 5, pp. 1-10, 2019.

Towards a Microfabricated Flexible Graphene-Based Active Implant for Tissue Monitoring During Optogenetic Spinal Cord Stimulation

Andrada Iulia Velea[1,2], Sten Vollebregt[2], Tim Hosman[1,3], Anna Pak[1,3], Vasiliki Giagka[1,3]

[1]*Bioelectronics Section and* [2]*Electronic Components, Technology and Materials Section, Department of Microelectronics, Delft University of Technology, Mekelweg 4, 2628 CD, Delft, The Netherlands*
[3]*Technologies for Bioelectronics Group, Department of System Integration and Interconnection Technologies, Fraunhofer Institute for Reliability and Microintegration IZM, Berlin, Germany*

A.I.Velea@student.tudelft.nl, S.Vollebregt@tudelft.nl, timothy.benjamin.hosman@izm.fraunhofer.de, A.Pak@tudelft.nl, V.Giagka@tudelft.nl

***Abstract* – This work aims to develop a smart neural interface with transparent electrodes to allow for electrical monitoring of the site of interest during optogenetic stimulation of the spinal cord. In this paper, a microfabrication process for the wafer-level development of such a compact, active, transparent and flexible implant is presented. Graphene has been employed to form the transparent array of electrodes and tracks, on top of which chips have been bonded using flip-chip bonding techniques. To provide high flexibility, soft encapsulation, using polydimethylsiloxane (PDMS) has been used. Making use of the "Flex-to-Rigid" (F2R) technique, cm-size graphene-on-PDMS structures have been suspended and characterized using Raman spectroscopy to qualitatively evaluate the graphene layer, together with 2-point measurements to ensure the conductivity of the structure. In parallel, flip-chip bonding processes of chips on graphene structures were employed and the 2-point electrical measurement results have shown resistance values in the range of kΩ for the combined tracks and ball-bonds.**

***Keywords* – Neural interface, optogenetic stimulation, transparent active implant, graphene, PDMS.**

I. Introduction

Epidural spinal cord stimulation (ESCS) has been proven to promote locomotion recovery in patients affected by spinal cord injuries (SCIs) [1]. However, optimization of the specifications for such therapies is still under research and identifying the mechanism of action could greatly benefit from parallel monitoring of the response of the biological tissue during stimulation. Traditionally, in ESCS, energy is injected into the tissue in the form of electrical pulses, leading to activation. Recently, the use of light for activating the biological tissue after genetic modification of the cells, a method known as optogenetics, has been gaining popularity in the field of spinal cord stimulation, due to the fact that it enables more selective activation of the neural cells [2].

Most electrode arrays for ESCS feature opaque electrodes which limit the electrical monitoring of the tissue response during optogenetic excitation [3, 4]. Therefore there is the need to develop optically transparent, conductive, and flexible neural interfaces that can enable capturing the electrical activity of the neurons below the activation site at the time of stimulation. One potential material for these electrodes is graphene, as the material is optically transparent, bendable, potentially biocompatible, and has excellent electrical properties [5, 6]. Graphene microelectrode arrays have been previously reported as passive implants with Au tracks to interface the electrodes with the outside active system [5]. However, for a smart implant, ultimately, active components, e.g. integrated circuits (ICs), have to be embedded with the electrodes to allow for signal acquisition, in-situ amplification and processing.

The aim of the current work is the development, by means of microfabrication, of a compact, flexible, graphene-based, active spinal cord monitoring implant to be used during optogenetic stimulation.

II. Materials and Methods

A microfabrication process has been used to ensure reproducibility and maintain the small size of the implant while achieving high resolution. Fig. 1 illustrates the process steps of the current work.

Chemical vapour deposited (CVD) graphene tracks and electrodes have been microfabricated on a silicon (Si) wafer, using a pre-patterned 50 nm molybdenum (Mo) layer as a

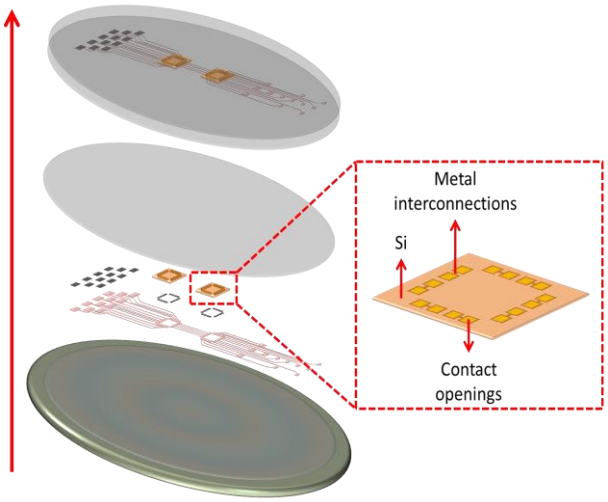

Fig. 1. Process steps of the proposed method. A molybdenum catalyst layer is used for graphene growth, on top of which chips are bonded and later, the complete structure is encapsulated in polymer.

catalyst, deposited on a silicon dioxide (SiO_2) layer as described in detail by Vollebregt et al., [7]. On top, metal was deposited and patterned to create a bonding interface between graphene and the gold (Au) stud bumps existent on the pads of the chips. Two different metallization versions were created; one consisted of 675 nm of aluminium (Al) and the other of 100 nm of titanium (Ti) and 675 nm of Al.

Chips were then bonded to the substrate using a thermocompression flip-chip bonding technique. As an underfill material and to improve the bonding stability, either an anisotropic conductive adhesive (ACA) (Toshiba TAP0212E) or a non-conductive adhesive (NCA) (Epotek 303-2FL) was manually applied to the substrate before bonding. The adhesive was pre-heated at 90 °C for 30 seconds for degassing purposes. Finally, the chips were bonded using a thermocompression bonding cycle of 60 seconds at 250 °C while applying roughly 19 MPa of pressure. The applied temperature also cured the adhesive. Next, 50 µm of Sylgard 184 polydimethylsiloxane (PDMS), 1:10 ratio, was spin-coated on top of the structure and cured at 90 °C for 1 hour. At this point, the complete structure had to be transferred or released from the original wafer in order to spin coat the final backside PDMS encapsulation layer. To do so, two approaches were investigated, as illustrated in Fig. 2.

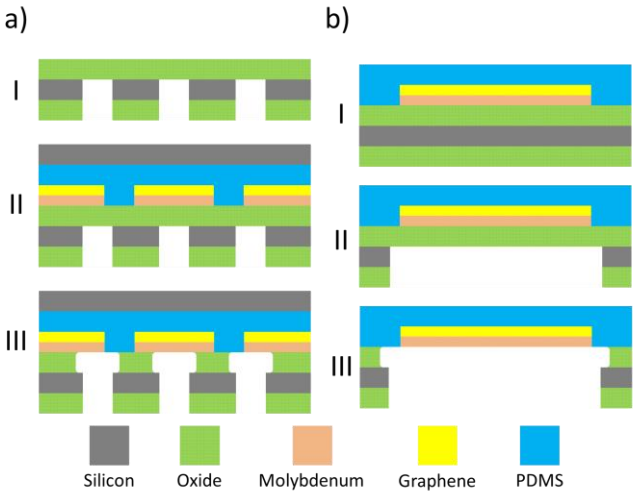

Fig. 2. Approaches used to transfer/ release the structure. In (a), a wet transfer approach, using buffered hydrofluoric acid (BHF) 7:1 for oxide etching. In (b), a "Flex-to-Rigid" (F2R) approach [8].

The approach in Fig. 2(a) consists of the creation of through-silicon vias (TSV), using a deep reactive ion etching (DRIE) process before graphene growth, to increase the number of access points for the etchant. The alternative approach in Fig. 2(b) consists of a DRIE process for cm-size suspended areas (that can later be coated with PDMS as final encapsulation), performed after the graphene growth completion, an approach known as Flex-to-Rigid (F2R) [8]. Any of the two aforementioned approaches is followed by a BHF 7:1 wet etching step for the removal of the remaining oxide layer which acts as a stopping layer for the DRIE process.

III. Results and Discussion

A. *Wafer-level graphene growth*

First, Raman spectroscopy was performed to ensure the presence of graphene after growth on the full wafer and to evaluate the quality of the layer at this step (Fig. 3).

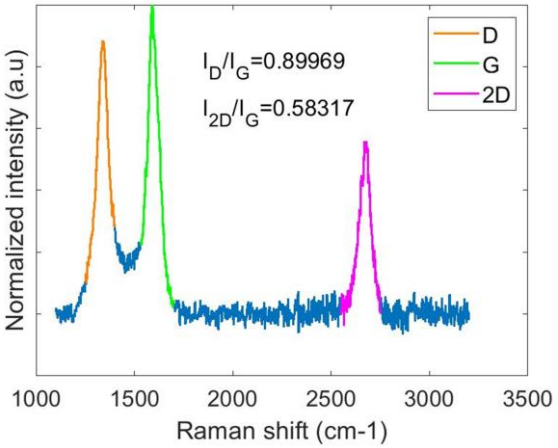

Fig. 3. Raman spectroscopy measurement, acquired using a 633 nm laser. The 3 peaks indicate the presence of graphene after the growth step.

Based on what has been previously reported in the literature, if graphene is present, the D band should appear at ~1330 cm^{-1}, G band at ~1590 cm^{-1} and 2D band at ~2660 cm^{-1} [9]. The ratio I_{2D}/I_G, greater than 1 for a monolayer graphene, suggests that multilayer graphene has been grown, since its value decreases significantly with the increase in number of layers [10]. This constitutes an advantage for this application due to the fact that within a multilayer graphene structure the grain boundaries will not be aligned, thus providing more mechanical stability, an important aspect for flexible devices. The ratio I_D/I_G estimates the number of defects, originating from the growth process, present in the graphene layer (the greater the ratio, the more defects can be found) [7]. Ideally, if no defects are present, I_D should be equal to 0 but as observed in Fig. 3, the D peak is relatively pronounced.

Besides Raman spectroscopy, 2-point measurements were conducted over an area of 70 µm in width and approximately 1 mm in length, to electrically evaluate the graphene tracks. The results can be observed in Fig. 4.

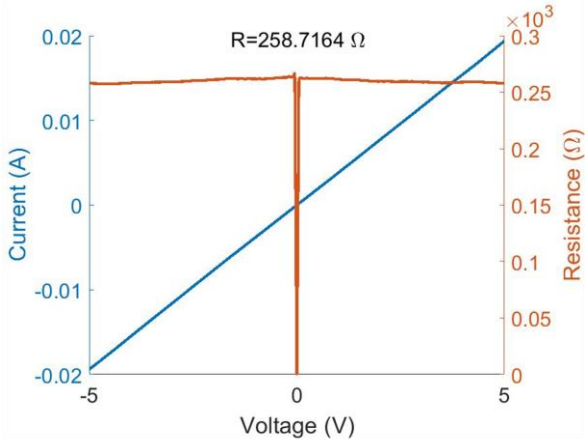

Fig. 4. 2-point measurement result over a graphene area of 70 um in width and 1 mm in length.

The measured resistance is ~250 Ω for a parallel configuration of Mo and graphene since, at this point, Mo has not been removed from the wafer.

B. *"Wet" transfer of structure*

BHF etching of the oxide layer from beneath the structure has been tested. The expected etch rate was 150 nm/min and the total calculated etching time was 40 min. Yet, after 7 hours, no etching around the TSV has been observed. Possibly, DRIE of the TSV resulted in the deposition of a polymer layer which could not be removed by O_2-plasma treatment. To circumvent this, potassium hydroxide (KOH) etching was performed to widen the pathways for the BHF. However, after these long wet etching steps, the structures were highly damaged or even removed, likely due to the PDMS being affected by the etchants. Since later in the process, at this step, chips containing active components will also be present, wet transfer of the structure is to be avoided.

C. *"Flex-to-rigid" approach*

Fig. 5 shows the structure after the F2R and oxide removal steps. The complete area of the implant, with Mo tracks and electrodes, was successfully suspended and the membranes did not contain any significant wrinkles or damages.

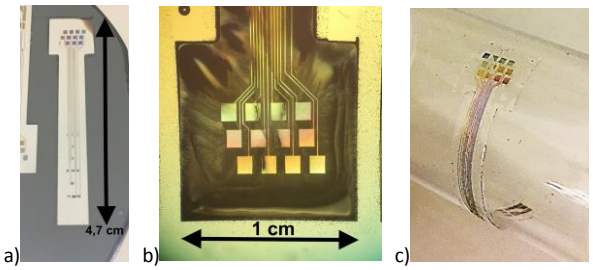

Fig. 5. Implant structure with Mo tracks after DRIE. In a), the complete suspended implant can be observed. In b), a detailed perspective of the PDMS membrane and tracks is presented. In c), the high flexibility of the structure is shown.

Fig. 6 illustrates the graphene-on-PDMS implant structures after the complete removal of the Mo layer using peroxide for ~ 5 min.

Fig. 6. Implant structure with graphene-only tracks and electrodes after F2R approach and catalyst removal. In this image the implant has not yet been released from the Si carrier wafer.

After the successful suspension of the graphene-on-PDMS structures, Raman spectroscopy evaluation has been conducted in order to ensure that the layer encapsulated in PDMS is graphene only. These results can be seen in Fig. 7.

The ratio I_D/I_G, which indicates the amount of defects present in the graphene layer, remains similar to the one measured after graphene growth and before any post-processing method has been applied. This result indicated that the transferring processes did not influence the quality of graphene. The ratio I_{2D}/I_G, which estimates the number of graphene layers present on the structure, increased compared to the previous measurements. The change in the measured value is likely influenced by the layer of material present underneath graphene, in this case PDMS, or previously, Mo on top of oxide [11]. The gray area represents the influence of PDMS over the measurement.

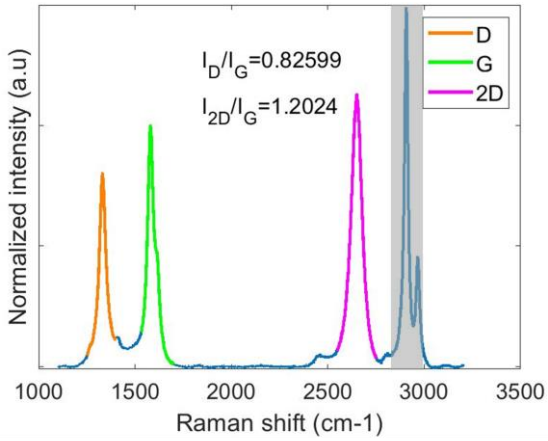

Fig. 7. Raman spectroscopy results after the suspension of the graphene-on-PDMS membranes.

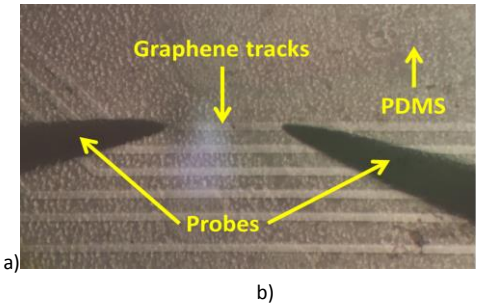

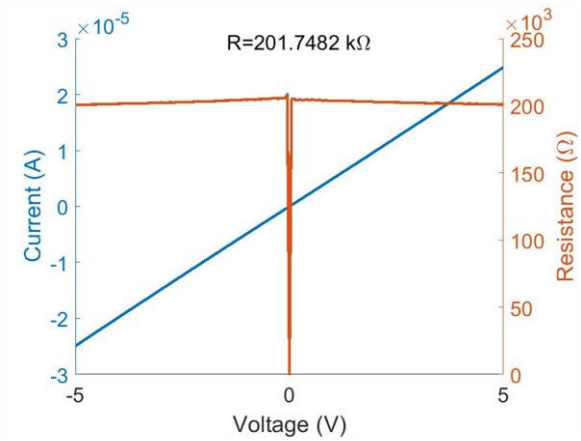

Fig. 8. 2-point measurement after releasing the structures using DRIE and wet etching steps for oxide and Mo removal. In a), the measurement points are illustrated. In b), the results obtained after the measurement can be observed.

A 2-point measurement evaluation has been conducted over the graphene tracks in order to evaluate their conductivity after Mo removal. Fig. 8 illustrates both measurement points as well as the I/(R)-V curves. The measured resistance value, for approximately the same area

of 70 µm in width and 1 mm in length, was in the range of kΩ (~200 kΩ), meaning that the resistance of Mo is much lower (cf. Fig. 4), thus having a great influence on the total resistance value when still underneath graphene.

An approximately square graphene pad (1050 µm by 910 µm) for which the dimensions do not influence the resistivity that much, therefore the resistivity resembles the sheet resistance of the material, showed a resistance value of about 7.5 kΩ as illustrated in Fig. 9.

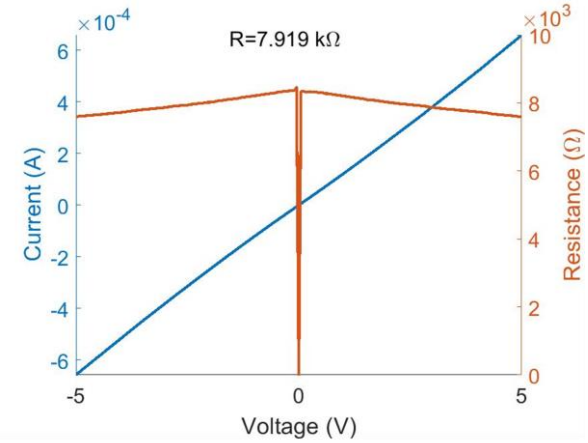

Fig. 9. 2-point measurement for a graphene pad of 1050 µm by 910 µmafter the release of the structures.

The influence of the contact resistance between graphene and the measurement probes, which is difficult to estimate, could play an important role in the measured value.

D. Flip-chip bonding

So far, no flip-chip bonding processes on graphene substrates have been reported in the literature and our initial attempt on flip-chip bonding dummy chips directly on graphene showed that the adhesion between graphene and Au stud bumps is poor, therefore chips could not be bonded. Even when using an NCA, as a different flip-chip bonding technique, as presented in section II "Materials and Methods" of this paper, the 2-point measurement results indicated open connections. Therefore, metal layers have been deposited on the pads of the implant to create an interface with the purpose of easing the assembly and improving the adhesion between Au stud bumps and graphene. Initially, only Al has been used as a metal interface since it is considered a good candidate for bonding processes but it has been noticed that there is poor adhesion between it and graphene [12]. Later, a stack of Ti and Al layers has been chosen to serve as an interface since Ti has been proven to have a good contact resistance with graphene [12] but it is not considered a good material for bonding processes.

Fig. 10(a) depicts a visual representation of the structures before and after flip-chip bonding. In Fig. 10(b), a computed tomography (CT) scan, after the bonding process is illustrated and it can be seen that the bumps have a coined-like shape, indicating that contact between the dummy chip and the substrate was made. In 10(c) a 2-point measurement result is shown. The resistance, ~8.9 kΩ, is the sum of the ball-bond and 2 graphene tracks resistances.

A second attempt of bonding dummy chips directly on graphene was performed using an ACA with nickel (Ni) particles. The 2-point measurement results are presented in Fig. 11 and it can be observed that they are similar

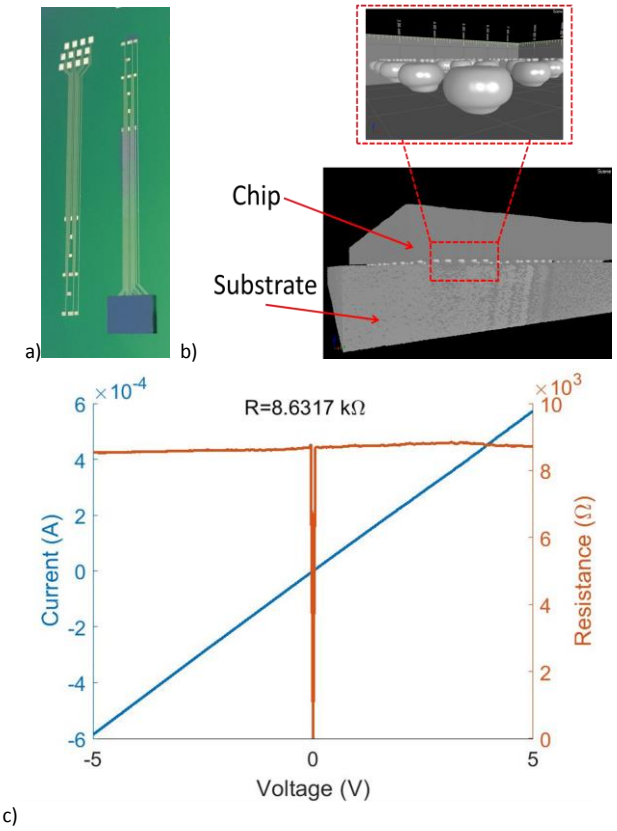

Fig. 10. Preliminary results after bonding. CT scans and 2-point measurements have been performed to ensure that the bonding process was successful.

(resistance value ~7.2 kΩ) to the previous case where a metal interface has been used for flip-chip bonding. This indicates that the Ni particles in the ACA adhere better to graphene than Au, thus creating a stable bonding interface between the stud bumps of the chip and the graphene substrate, without the need of depositing and patterning a metal layer on top of graphene. The chemistry behind this process is outside the scope of this research project.

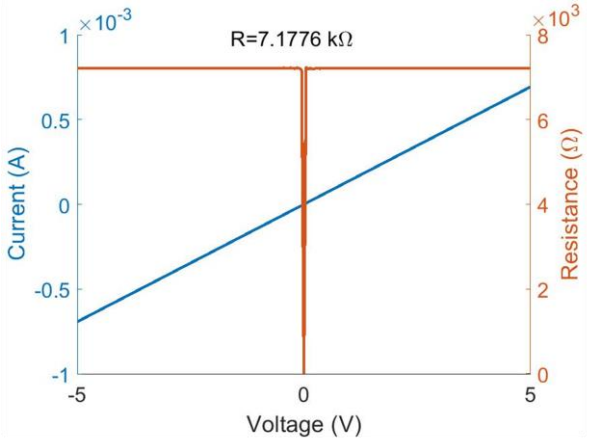

Fig. 11. 2-point measurement results for dummy chips bonded on a graphene substrate using a conductive adhesive (CA) flip-chip bonding technique.

Currently new devices are being fabricated which will allow the measurement of the flip-chip ball-bond only.

In the future, to meet the tight area requirements for the envisioned epidural monitoring implant the assembly will have to be performed with thin chips, which present unique handling challenges [13].

Moreover, before performing any *in-vivo* experiments, the implants have to be thoroughly characterized *in-vitro*. This implies optical transmittance evaluation, to establish the degree of transparency of the final device as well as electrical characterization to determine the signal to noise ratio (SNR) of graphene electrodes, important as low amplitude signals are expected to be recorded from the biological tissue. Apart from that, connecting the final device to the outside recording system constitutes a major challenge due to the small feature size of the test pads and the softness of the implant.

Once all these aspects are investigated outside the body, *in-vivo* experiments can be conducted in order to evaluate the biocompatibility of the materials used, mainly how the spinal cord reacts to graphene electrodes and PDMS encapsulation, as well as the reliability of the implant after it is implanted at its intended site, as in [14].

IV. Conclusions

This work presents the process for developing flexible, active, graphene-based epidural spinal cord monitoring implant, by means of microfabrication only. It has been shown that F2R approach can be used to suspend large areas of the graphene-on-PDMS structures, on the Si substrate, thus avoiding as much as possible wet process steps that can cause damage to the devices. Moreover, it has been demonstrated that flip-chip bonding of chips on a graphene substrate, using either metal interfaces or conductive adhesives, is possible and initial measurements have shown that there is electrical conductivity after the bonding process. To the authors' best knowledge, this is the first work that aims to fabricate a graphene-based active implant that can be used to enable in-situ recording of the evoked activity of optically activated neuronal populations during optogenetic spinal cord stimulation.

Acknowledgments

We acknowledge the staff of the Else Kooi Laboratory (EKL) from Delft University of Technology and Fraunhofer Institute for Reliability and Microintegration IZM for their support.

References

[1] R. van den Brand et al., "Restoring voluntary control of locomotion after paralyzing spinal cord injury", *Science*, vol. 336, no. 6085, pp. 1182-1185, 2012.

[2] K. L. Montgomery, S. M. Iver, A. J. Christensen, K. Deisseroth, and S. L. Delp., "Beyond the brain: Optogenetic control in the spinal cord and peripheral nervous system," *Science Transl. Med.*, vol. 8, no. 337rv5, pp. 1 – 12, May 2016.

[3] V. Giagka, A. Demosthenous, and N. Donaldson, "Flexible active electrode arrays with ASICs that fit inside the rat's spinal canal," *Biomed. Microdev.*, vol. 17, no. 6, pp. 106 – 118, Dec. 2015.

[4] I. R. Minev et al., "Electronic dura mater for long-term multimodal neural interfaces", *Science*, vol. 347, no. 6218, pp 159-163.

[5] D. W. Park et al., "Graphene-based carbon layered electrode array technology for neural imaging and optogenetic applications", *Nature Communications*, vol. 5, no. 5258, pp. 1 – 11, Oct. 2014.

[6] J. Y. Hong, W, Kim, D. Choi, J. Kong, and H. S. Park, "Omnidirectionally stretchable and transparent graphene electrodes," *ACS Nano*, vol. 10, pp. 9446 – 9455, Sept. 2016.

[7] S. Vollebregt et al., "A transfer-free wafer-scale CVD graphene fabrication process for MEMS/NEMS sensors", In Proc. *IEEE MEMS*, pp.17 – 20, Sanghai, China, Jan. 2016.

[8] B. Mimoun, V. Henneken, A. van der Horst, and R. Dekker, "Flex-to-rigid (F2R): A generic platform for the fabrication and assembly of flexible sensors for minimally invasive instruments", *IEEE Sensors*, vol. 13, no. 10, pp. 3873 – 3882, Mar. 2013.

[9] Y. Wu et al.,"Synthesis of large-area graphene on molybdenum foils by chemical vapor deposition", *Carbon*, vol. 50, no. 14, pp. 5226-5231, Nov. 2012.

[10] Z. Jian et al., "Irradiation effects of graphene and thin layer graphite induced by swift heavy ions", *Chinese Physics B*, vol. 24, no. 8, June 2015.

[11] Y. Y. Wang et al., "Raman Studies of Monolayer Graphene: The Substrate Effect", *J. Phys. Chem.*, vol. 112, no. 29, pp. 10637-10640, June 2008.

[12] S. Shi, "Effects of Silicon Oxides as Substrates for Graphene-based Gas Sensor", *TU Delft*, 2017

[13] V. Giagka, N. Saeidi, A. Demosthenous, and N. Donaldson, "Controlled silicon IC thinning on individual die level for active implant integration using a purely mechanical process," in Proc. *ECTC 2014*, Orlando, FL, USA, May 2014, pp. 2213 – 2219.

[14] V. Giagka, A. Vanhoestenberghe, N. Wenger, P. Musienko, N. Donaldson, and A. Demosthenous, "Flexible platinum electrode arrays for epidural spinal cord stimulation in paralyzed rats: An in vivo and in vitro evaluation," in Proc. *3rd Annual Conf. IFESSUKI 2012*, Birmingham, UK, Apr. 2012, pp. 52 – 53.

WAFER-SCALE GRAPHENE-BASED SOFT ELECTRODE ARRAY WITH OPTOGENETIC COMPATIBILITY

Andrada I. Velea,[1,2], Sten Vollebregt[2], Gandhika K. Wardhana[1,2]and Vasiliki Giagka[1,3]
[1]Bioelectronics Section, Department of Microelectronics, TU Delft, Delft, THE NETHERLANDS,
[2]Electronic Components, Technology and Materials Section, Department of Microelectronics, TU Delft, Delft, THE NETHERLANDS and
[3]Technologies for Bioelectronics Group, Department of System Integration and Interconnection Technologies, Fraunhofer IZM, Berlin, GERMANY

ABSTRACT

This paper reports on the characterization of a microfabricated wafer-scale, graphene-based, soft implant for spinal cord applications. Graphene is used because of its high transparency and good conductivity, making it suitable for optogenetic applications. Moreover it has a high mechanical strength and is potentially biocompatible. The implant consists of multi-layered chemical vapor deposited graphene, in the form of electrodes and tracks, encapsulated between 2 layers of silicone. Methods such as Raman spectroscopy, optical transmittance, and electrical measurements combined with bending tests and *in-vitro* experiments, using phosphate-buffered saline (PBS) solution, were employed to characterize the device. The results have shown high bendability and no critical damage of the graphene after immersing the device in PBS solution up to 7 days. To the authors' best knowledge, this is the first work that presents a soft and fully scalable optogenetics-compatible graphene-based spinal cord electrode array.

KEYWORDS

Wafer-scale implant, graphene, silicone, optogenetic compatibility.

INTRODUCTION

Spinal cord stimulation studies are an important research topic, mostly for pain relief but also for restoring locomotion after spinal cord injuries. Apart from clinical trials, more exploratory research is mostly conducted in rodents. However, the availability of suitable neurotechnologies tailored to small animals is limited. For instance, the spinal cord shows significant mechanical mismatch with rigid neural implants. Even flexible implants encapsulated in stiffer polymers such as polyimide can cause significant damage and compression to the spinal cord [1].

Therefore, effort has been put into the design and fabrication of reliable soft spinal cord implants, based on silicone elastomers.

Existing spinal cord microelectrode arrays (MEAs) feature opaque electrodes [1, 2] which are used to electrically activate the tissue or record evoked electrical activity. Alternatively, tissue activation by means of light, i.e. optogenetics, is promising to increase the resolution of activation. This is due to the fact that it activates the tissue in a more type-specific manner. Only neurons that are genetically modified to respond to light will be activated, as long as they are in the vicinity of the light source and the intensity of it is enough to trigger action potentials [3].

To quantify the effect of this new technology there is great need to monitor the electrical response of cells at the site of optogenetic stimulation. To this end, MEAs with transparent electrodes are a necessary tool. In such a system, the transparency will guarantee that light, coming from an external source, can pass through the electrode site, activating the target location. Moreover, the conductivity of MEAs will allow for in situ recording of the evoked electrical response. This temporally and spatially concurrent recording during stimulation is not possible with conventional electrodes, as these systems require both the activating and recorded signals to be in the electrical domain. Transparent parylene-based graphene electrode arrays, with metal tracks, have previously been developed to allow for electrophysiology, *in-vivo* imaging and optogenetics in the brain [4]. However, parylene, with a Young's modulus of ~2 GPa [5] is still very stiff for the spinal cord.

This work proposes a wafer-scale fabrication process for a silicone-sandwiched graphene-based implant. The materials used ensure the required transparency and conductivity but also provide the necessary softness for interacting with the spinal cord. The design of the proposed implants ensures that any metal layers, if present, only appear at areas which are not under mechanical strain as they have been proven to have poor adhesion to graphene, thus causing delamination [6].

MATERIALS AND METHODS

The proposed solution was implemented by employing a scalable, 2-mask microfabrication process, inspired by the "flex-to-rigid" (F2R) approach [7], together with a transfer-free CVD process for graphene growth [8] as shown in Fig.1.

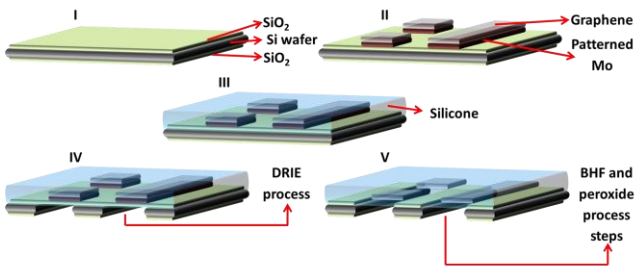

***Figure 1**: Microfabrication process flow. SiO_2 deposition (I). Graphene growth on the molybdenum (Mo) catalyst (II). First layer of silicone spin-coated and cured on top of the structure (III). Release of the complete area using DRIE for Si and wet etching steps to remove the oxide and Mo layers (IV, V).*

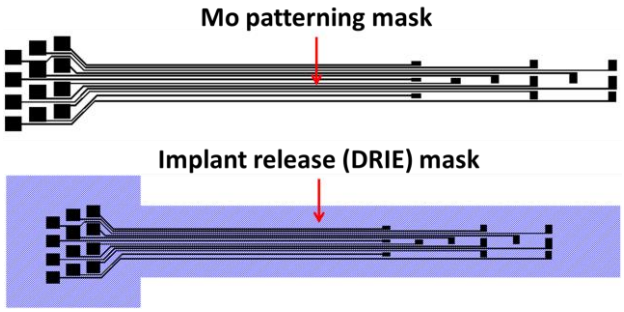

***Figure 2**: Masks used to develop and suspend the graphene-based passive implants.*

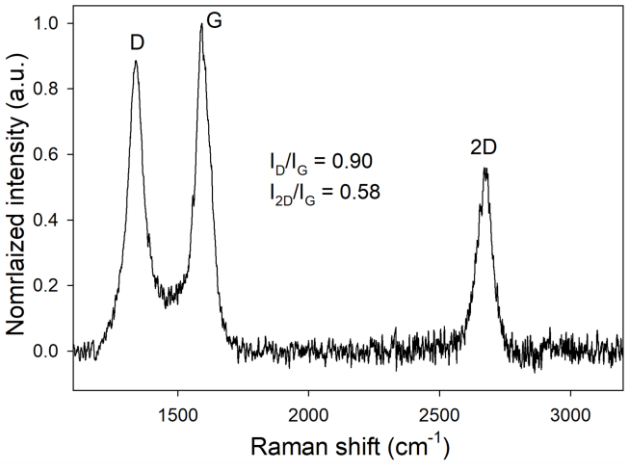

***Figure 3**: Raman spectroscopy evaluation (using a 633 nm laser) after the CVD process. The I_{2D}/I_G ratio, indicate that a multi-layer graphene has been grown [11].*

As the developed prototypes are intended to be used for *in-vivo* experiments in rats, the MEAs had to be designed accordingly. A total of 12 electrodes were distributed as in Fig. 2, each of them being connected to individual test pads. This number allows for a large coverage of the spinal cord but also fits into the limited space available for implantation in rats [9].

For the microfabrication process, 6 µm of plasma-enhanced chemical vapor deposited (PECVD) oxide were deposited on both sides of a double-side polished (DSP) silicon (Si) wafer. Then, on the frontside, 50 nm of molybdenum (Mo) were sputtered and patterned. This serves as a catalyst for graphene growth. Next, graphene was grown using a CVD process [8] to ensure uniformity of the layer, reproducibility and scalability of the manufacturing.

Before encapsulating the structures in silicone, Raman spectroscopy and two-point measurements were employed to evaluate the graphene layer. Next, 50 µm of Sylgard 184 silicone were spin coated on top of the structures and cured for 1 h at 90 °C. Finally, for the backside of the wafer, a deep reactive ion etching (DRIE) process, was employed only over the areas containing the implants, thus suspending them completely (Fig. 3). This was followed by wet etching of the oxide and Mo layers. Before spin-coating the final encapsulation layer on the backside of the wafer, the structure was again evaluated

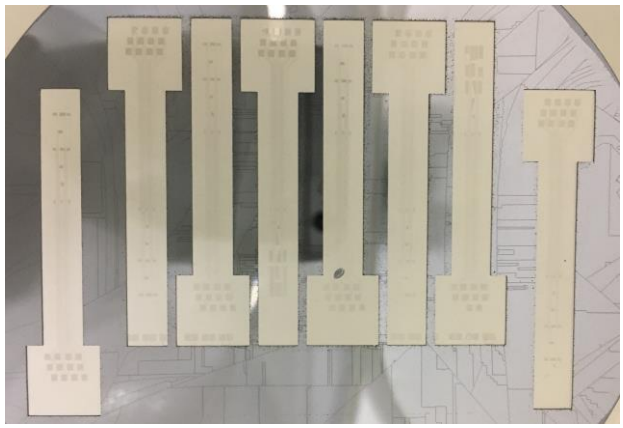

***Figure 4**: Photograph of the 8 implants fabricated on a single 10 cm wafer.*

by means of Raman spectroscopy and 2-point measurements to ensure that no critical damage was present after the microfabrication process. Moreover, optical transmittance measurements were performed to approximate the number of graphene layers and the transparency of the released graphene-on-silicone structure. In addition, *in-vitro* experiments were conducted using PBS saline solution for 24 h and 7 days to quantify how much graphene degrades over time.

The structures were then cut out from the wafers and bending tests were performed by placing the implant around rods with different diameters to emulate handling and deformation expected at the site of implantation. For the actual implant, the final layer of silicone encapsulation can be applied and openings for the electrodes and test pads can be created before removing the samples from the Si wafer. The robust process achieves high yield and the authors are employing a similar microfabrication process as a basis for the first graphene-based active implants (details can be found in [10]).

RESULTS AND DISCUSSION

Raman Spectroscopy

After developing the graphene MEAs on the Si wafer, Raman spectroscopy was employed to determine the presence of graphene and to qualitatively evaluate it. The results in Fig. 3 demonstrate that a multi-layer graphene is present, judging from $I_{2D}/I_G < 1$ [11]. To monitor graphene, Raman spectroscopy was employed after suspending the implants and removing the oxide and Mo layers (the structures are shown in Fig. 4). Also, after conducting the *in-vitro* experiments, in saline solution, to emulate the biological environment, the graphene layer had to be investigated to evaluate if the graphene is damaged by the PBS solution.

The results in Fig. 5, illustrate that there was no critical damage present on the graphene layer after the microfabrication process. After immersing the structures in PBS, the D peak (indicating the number of defects present) slightly increases. This could be caused by surface contamination of the graphene layer with different particles from the solution. The additional peaks seen on the Raman spectra represent the influence of the silicone Raman signal over the measurement.

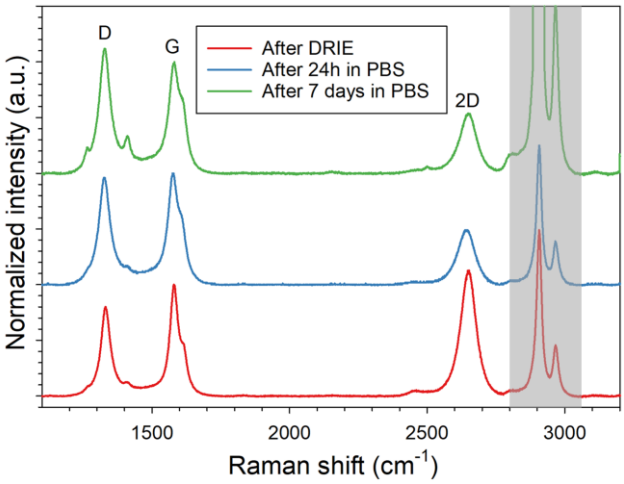

***Figure 5**: Raman Spectroscopy results DRIE process and after immersing the structure in PBS for 24 h and 7 days, respectively. The grey area represents the silicone Raman signal.*

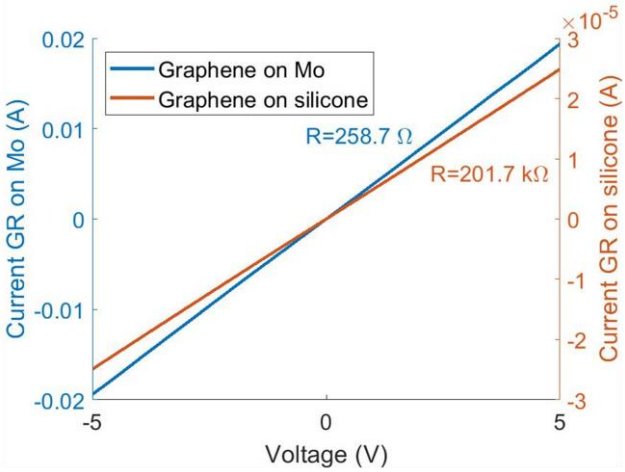

***Figure 6**: Two-point electrical evaluation of graphene after the CVD process. The results show a resistance value of ~250 Ω for graphene on Mo, and ~200 kΩ for graphene on silicone. The contact resistances from the probes also contribute to the overall resistance.*

Two-Point Measurements

Apart from Raman spectroscopy, the electrical properties of the graphene were investigated. To this end, two-point measurements were employed after graphene growth (Fig. 6), after suspension of the passive implants (Fig. 6 and Table 1), as well as after conducting the *in-vitro* experiments (Table 1). All measurements were performed over a graphene line of 70 µm in width and 1 mm in length.

A significant difference in resistance can be seen from Fig. 6. This originates from the fact that after graphene growth, the measured value is the resistance of both Mo and graphene, whereas for the suspended implants, only the graphene layer was probed as the Mo catalyst had been removed. From this it can be concluded that the resistance of Mo is significantly lower than that of graphene. Moreover, for the suspended implants, the probes were landed directly on graphene which was resting on a 50 µm soft silicone substrate, without any metal interface between the measured layer and the two-point probes. Therefore, the accuracy of the measurement was significantly reduced due to the less controllable contact resistance. Ideally, the graphene track should be measured using a four-point measurement setup to reduce the contact resistance and, on top of that, a metal layer is needed for landing the probes and not damaging the graphene layer. Such designs were not included in the current layout but will be included in future work.

***Table 1**. Two-point electrical measurement results*

Sample type	Voltage range	Measured resistance
After DRIE	-5 V to 5 V	200 kΩ
After DRIE and 24 h in PBS	-5 V to 5 V	160 kΩ
After DRIE and 7 days in PBS	-5 V to 5 V	130 kΩ

Having the implants suspended, *in-vitro* experiments using PBS solution were conducted for periods of 24 h and 7 days respectively. After each period of time, the samples were electrically evaluated, and the results synthesized in Table 1 demonstrate that graphene does not deteriorate *in-vitro*. The observed differences likely originate from the inaccuracy of the two-point measurements.

Bending Tests

As the implantation site for the described structures is subjected to different types and degrees of movements, mechanical evaluation is also needed. To this end, bending tests using metal rods with diameters ranging from 8 mm down to 3 mm, followed by resistive measurements were employed. In Fig. 7, a passive implant on a 3 mm metal rod is shown while Table 2 synthesizes the electrical measurements performed after bending the samples on different rods. The measured resistance is ~2 MΩ, which originates from the large length-to-width (L/W) ratio of the implant and the high contact resistance. Since the probing setup was not tailored for such small prototypes, longer tracks had to be measured such that the probes could properly be landed on the sample under test. However, the results in Table 2, all in the same range, demonstrate that the passive structures can be bent down to 3 mm without damage.

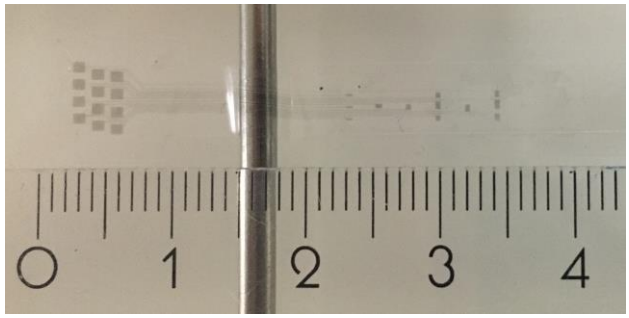

***Figure 7**: Implant released from the wafer and placed on top of a 3 mm bending rod.*

***Table 2**. Bending test results (using two-point electrical measurements)*

Sample type	Voltage range	Measured resistance
No bending	-5 V to 5 V	1.2 MΩ
Bending (8 mm rod)	-5 V to 5 V	1.8 MΩ
Bending (5 mm rod)	-5 V to 5 V	2.5 MΩ
Bending (3 mm rod)	-5 V to 5 V	2.4 MΩ

Note: In case the application requires, this resistance could be lowered (Fig. 5) by leaving the Mo on some parts of the graphene tracks. Using Mo instead of another metal has the advantage that the graphene-Mo bonds are strong, originating from the CVD process.

Optical Transmittance

As these MEAs are intended to be used in optogenetics, optical transmittance measurements had to be conducted to evaluate the degree of transparency for the final implant. From the optical transmittance result in Fig. 8 it was determined that the implant consists of ~11 graphene layers and has a transmittance of 72-77% [12].

CONCLUSIONS

This paper describes the methods used to evaluate graphene-based passive implants for spinal cord applications. Graphene quality (using Raman), electrical and mechanical characterizations of the final prototypes were performed. Although there were no dedicated structures to evaluate the electrical conductivity of the implants, it has been proven that graphene does not deteriorate and moreover, still conducts after immersing the implants in PBS up to 7 days, as well as after bending them over different rod diameters, down to 3 mm.

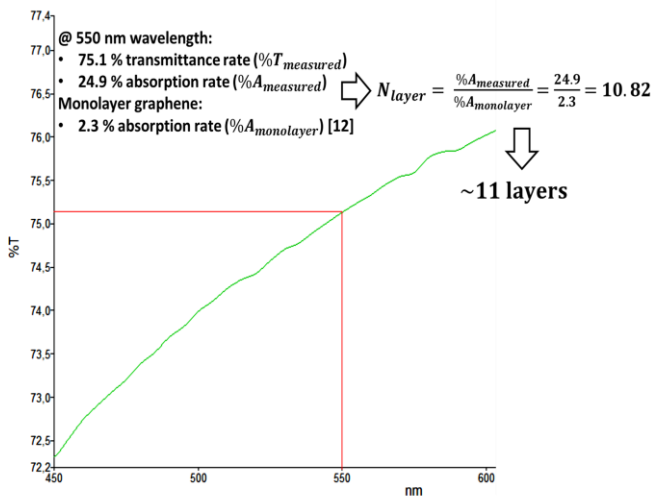

***Figure 8**: Optical transmittance results for the graphene-based implant. On the X-axis, the light wavelength range (visible spectrum). On the Y-axis, the percentage of the light transmitted through the sample.*

This paper demonstrates the potential of soft, graphene-based passive implants, to enable unique, currently not available, spinal cord tissue monitoring during optogenetic activation, which is paramount to map the neuronal activation at this level.

ACKNOWLEDGMENTS

We acknowledge the staff of Else Kooi Laboratory (EKL) and the Bioelectronics group from Delft University of Technology for their support throughout the project.

REFERENCES

[1] I. R. Minev et al., "Electronic dura mater for long-term multimodal neural interfaces", *Science*, vol. 347, no. 6218, pp. 159-163, 2015.

[2] V. Giagka, A.Demosthenous and N. Donaldson, "Flexible active electrode arrays with ASICs that fit inside the rat's spinal canal", *Biomed. Microdev.*, vol. 17, no. 6, pp. 106-118, 2015.

[3] K. L. Montgomery et al., "Beyond the brain: Optogenetic control in the spinal cord and peripheral nervous system", *Science Transl. Med.*, vol. 8, no. 337rv5, pp. 1-12, 2016.

[4] D. W. Park et al., "Fabrication and utility of a transparent graphene neural electrode array for electrophysiology, in vivo imaging and optogenetics", *Nat. Protoc.*, vol. 11, no. 11, pp. 2201-2222, 2016.

[5] K. Scholten and E. Meng, "Materials for microfabricated implantable devices: a review", *Lab on a Chip*, vol. 15, no. 22, pp, 4256-4272, 2015.

[6] J. Robinson et al., "Contacting graphene", *Appl. Phys. Lett.*, vol 98, no. 5, 2011.

[7] B. Mimoun et al., "Flex-to-rigid (F2R): A generic platform for the fabrication and assembly of flexible sensors for minimally invasive instruments", *IEEE Sensors*, vol. 13, no. 10, pp. 3873-3882, 2013.

[8] S.Vollebregt et al., "A transfer-free wafer-scale CVD graphene fabrication process for MEMS/NEMS sensors", in Proc. *IEEE MEMS 2016*, Sanghai, China, 2016, pp. 17-20.

[9] V. Giagka et al., "Flexible platinum electrode arrays for epidural spinal cord stimulation in paralyzed rats: An in vivo and in vitro evaluation", in Proc. *3rd Annual Conf. IFESSUKI 2012*, Birmingham, UK, 2012, pp. 52-53.

[10] A. I. Velea, S. Vollebregt, T. Hosman, A. Pak and V. Giagka "Towards a microfabricated flexible graphene-based active implant for tissue monitoring during optogenetic spinal cord stimulation", in Proc. *IEEE NMDC 2019*, Stockholm, Sweden, 2019.

[11] Z. Jian et al., "Irradiation effects of graphene and thin layer graphite induced by swift heavy ions", *Chinese Phys. B*, vol. 24, no. 8, 2015.

[12] K. F. Mak et al., "Measurement of the optical conductivity of graphene", *Phys. Rev. Lett*, vol. 101, no. 19, pp. 2-5, 2008.

CONTACT

*A. I. Velea; A.I.Velea@student.tudelft.nl;
*S. Vollebregt; S.Vollebregt@tudelft.nl;
*G. K. Wardhana; G.K.Wardhana@tudelft.nl;
*V. Giagka; V.Giagka@tudelft.nl.

Name: Implant substrate

Version: 1
Valid from: 26 August 2019
Made by: Andrada Velea

Run number: BE 2325
Process engineer: Andrada Velea
Mentor: Sten Vollebregt

Start date processing: 01 September 2019
Estimated end date:
Contamination: Yes

Labs: CR100, CR10000

EKL(Else Kooi Laboratory)
DELFT UNIVERSITY OF TECHNOLOGY
Address Feldmannweg 17, 2628 CT Delft, The
P.O. Box 5053, 2600 GB Delft, The Netherlands
Phone +31 - (0)15 - 2783868
Fax : +31 - (0)15 - 2622163
Website http://ekl.tudelft.nl/EKL/Home.php

Detailed information about possible contamination:

Place/Clean Rooms used in process:
Write the sequence of used labs from start to finish.
Which (Non-standard) materials or process steps
Process step number
What kind of process or machine was used?
The other materials or wafers that contain non-green metals that are also processed in this machine

Lab/ Clean Room	Non-standard materials	Process step	Machine-process	Other materials used in machine
CR100	none	none	none	none
CR10000	Yes, graphene	30	BlackMagic	Cu, Pt, Ni

If there are custom steps in a standard process or possible cross contamination materials are used: Write down the
Step number
Material
Machine/tool where the process is done
Pre and past process step numbers that are used to prevent cross contamination.

None

Step number	Material	Machine/Tool/lab	Process steps to prevent cross contamination
31	Cu	Trikon Sigma	Use own dedicated transport wafers and cassette for contaminated wafers
39	Cu/PDMS	Trikon Sigma	Use own dedicated transport wafers and cassette for contaminated wafers
45	Cu	Trikon Ωmega 201	Use own dedicated transport wafers and cassette for contaminated wafers
4	Cu	Alcatel	Use dedicated chuck for contaminated wafers

GENERAL RULES

CLEANROOM BEHAVIOUR

Always follow the "**Security and Behaviour**" rules when working in the EKL laboratories.

Always handle wafers with care during processing. Use cleanroom gloves and work as clean as possible!!

Use cleanroom gloves when working with vacuum equipment. Do not touch the inside or carriers with bare hands.

Always check equipment and process conditions before starting a process. Do NOT make unauthorized changes!

Directly notify the responsible staff member(s) when there are problems with equipment (like malfunction or contamination). Put the system down in the Phoenix reservation system, and turn the equipment status sign from UP or Usable to DOWN.

DO NOT TRY TO REPAIR OR CLEAN EQUIPMENT YOURSELF, and NEVER try to refresh a contaminated etch or cleaning bath! Only authorized staff members are allowed to do this.

PCC RULES

All substrates, layers and chemicals which are not CMOS compatible are considered to be "NON-STANDARD" materials, and may be contaminating.

The use of "non-standard" materials for processing in the class100 and SAL cleanroom must ALWAYS BE EVALUATED AND APPROVED by your mentor and in agreement with the PCC document.
Wafers that are contaminated may NEVER be processed in any of the equipment without permission of the Equipment owner Special precautions may have to be taken, like the use of a special substrate holder or container.

Check the PCC "Rules & Instructions" - available on the "EKL intranet webpage" - for more details.

CLASS 100 RULES

CLEANING OF WAFERS

After several hours (4 hours max) of storage wafers must always be cleaned before performing a COATING, FURNACE, EPITAXY OR DEPOSITION step.

Use the correct cleaning procedure:

- Tepla stripper ⇨ for removal of implanted or plasma etched photoresist
- Acetone ⇨ for removal of photoresist that is not implanted or plasma etched
- HNO_3 99% (Si) ⇨ for IC compatible wafers which do not need a HNO_3 69.5% step
- HNO_3 99% (Al) ⇨ for wafers which are or have been in contact with one of the following metals: like Al, Al(1%Si), Ge, Ti, Zr
- HNO_3 99% (Si) + HNO3 69.5% (Si) ⇨ for all other IC compatible wafers

Note:

▪The above described cleaning procedures are only valid for IC compatible wafers with "standard" materials on them. **In all other situations follow the PCC rules (Previously to be discussed with the mentor).**

▪Wafers do not have to be cleaned **after** a furnace, epitaxy or deposition step if the next process step will be performed immediately, unless the wafers are covered with particles.

FURNACE RESTRICTIONS

Wafers that are covered with photoresist or a metal layer may NEVER be processed in any of the furnaces. This also applies for wafers from which a metal layer has been removed by etching. Only alloying in tube C4 is allowed for wafers with an aluminium layer.

MEASUREMENTS

Always perform all the measurement and inspection steps, and **write down the results in your journal and in the result tables that can be found at some of the equipment!!** The results are used to check the condition of the processes and/or equipment.

It is possible to use the following Class 100 equipment to measure directly onto your (IC compatible) process wafers:

•The Leitz MPV-SP, the WOOLLAM and the SAGAX. These systems are used for thickness measurements of transparent layers. The measurements are non-destructive and without contact to the wafer surface.

•The Dektak 8 surface profilometer. This system is used for step height measurements. In this case a needle will physically scan over the wafer surface (contact measurement), which can be destructive for structures.

•The XL50 SEM. It can be used for inspection of your wafers and for width, depth or thickness measurements.

Note:

▪After certain measurements cleaning of your wafers may be required for further processing.

An extra wafer must be processed when other measurement methods will be used (like sheet resistance and junction depth measurements). These wafers cannot be used for further processing.

STARTING MATERIAL

Use **10 double side polished test wafers of 500 µm** with the following specifications:

Type:	p (p-type)
Orientation:	<100>
Resistivity:	2-5 Ωcm
Thickness:	500 ± 15 µm
Diameter:	100 mm
Number of wafers:	10

PROCESS DESCRIPTION

The aim of the current process is to develop a graphene-based, flexible implant. Graphene is being grown on a Mo layer. After graphene growth, post-processing is required to achieve the final implant structure. Therefore, cross contamination might occur. The required process steps to prevent cross contamination are mentioned in the beginning of the document.

The process consists of 11 parts:

Part 1: Cleaning step
Part 2: Creation of zero layer
Part 3: DRIE preparation
Part 4: Molybdenum deposition, patterning and graphene growth
Part 5: Metal deposition and patterning
Part 6: Flip-chip bonding @ Fraunhofer (Berlin)
Part 7: PDMS encapsulation-first layer
Part 8: PDMS etching
Part 9: DRIE – @ CR10000
Part 10: Oxide etching and Mo removal
Part 11: PDMS encapsulation-second layer

PART 1: CLEANING STEP

Perform this step ONLY when wafers are taken out of an already opened box!

1. CLEANING PROCEDURE: HNO_3 99% and 69.5%

Cleaning:

10 minutes in fuming nitric acid (Merck: HNO_3 99%) at ambient temperature.
Use wet bench "HNO_3 (99%)" and the carrier with the white dot.

QDR:

Rinse in the Quick Dump Rinser with the standard program until the resistivity is 5 MΩ.

Cleaning:

10 minutes in concentrated nitric acid (Merck: HNO_3 69.5%) at 110 °C.
Use wet bench "HNO_3 (69.5%)" and the carrier with the white dot.

QDR:

Rinse in the Quick Dump Rinser with the standard program until the resistivity is 5 MΩ.

Drying:

Use the Semitool "rinser/dryer" with the standard program, and the white carrier with a red dot.

PART 2: CREATION OF ZERO LAYER

FRONTSIDE

2. COATING AND BAKING

Use the EVG 120 wafertrack to coat the wafers with resist. The process consists of a treatment with HMDS (hexamethyldisilazane) vapor with nitrogen as a carrier gas, spin coating with Shipley SPR3012 positive photoresist, and a soft bake at 95degC for 90 seconds. Always check the temperature of the hotplate and the relative humidity (48 ± 2 %) in the room first.

- Use coating **Co – Zero Layer** (resist thickness: 1.400 µm).

3. ALIGNMENT AND EXPOSURE

Use the ASM PAS 5500/80 automatic waferstepper.

- Use **COMURK mask**, die-size 10x10 mm, job: **litho/Zefwam**, energy: **120** mJ/cm^2.

4. DEVELOPMENT

Use the EVG 120 wafertrack to develop the wafers. The process consists of a post-exposure bake at 115 degC for 90 seconds, followed by a development step using Shipley MF322 developer (single puddle process), and a hard bake at 100 degC for 90 seconds. Always check the temperature of the hotplates first.

- Use development **program Dev - SP**

5. INSPECTION: LINEWIDTH

Visually inspect the wafers through a microscope, and check the linewidth. No resist residues are allowed.

6. PLASMA ETCHING OF ALIGNMENT MARKS

Use the Trikon Ωmega 201 plasma etcher.

- Use sequence **URK_NPD** and set the platen temperature to **20 °C** to etch 1200 Å deep ASM URK's into the silicon.

7. CLEANING PROCEDURE: TEPLA + HNO_3 99% and 69.5%

Plasma strip:

Use the Tepla plasma system to remove the photoresist in an oxygen plasma.

- Use **program 1**

Cleaning:

10 minutes in fuming nitric acid (Merck: HNO_3 99%) at ambient temperature.
Use wet bench "HNO_3 (99%)" and the carrier with the white dot.

QDR:

Rinse in the Quick Dump Rinser with the standard program until the resistivity is 5 MΩ.

Cleaning:

10 minutes in concentrated nitric acid (Merck: HNO_3 69.5%) at 110 °C.
Use wet bench "HNO_3 (69.5%)" and the carrier with the white dot.

QDR:

Rinse in the Quick Dump Rinser with the standard program until the resistivity is 5 MΩ.

Drying:

Use the Semitool "rinser/dryer" with the standard program, and the white carrier with a red dot.

BACKSIDE

8. COATING AND BAKING

Use the EVG 120 wafertrack to coat the wafers with resist. The process consists of a treatment with HMDS (hexamethyldisilazane) vapor with nitrogen as a carrier gas, spin coating with Shipley SPR3012 positive photoresist, and a soft bake at 95degC for 90 seconds. Always check the temperature of the hotplate and the relative humidity (48 ± 2 %) in the room first.

- Use coating **Co – Zero Layer** (resist thickness: 1.400 µm).

9. ALIGNMENT AND EXPOSURE

Processing will be performed on the ASM PAS 5500/80 automatic waferstepper.

- Use **COMURK mask**, die-size 10x10 mm, job: **litho/ZEFWAM FTBA.2**, energy: **120** mJ/cm^2.

10. DEVELOPMENT

Use the EVG 120 wafertrack to develop the wafers. The process consists of a post-exposure bake at 115 degC for 90 seconds, followed by a development step using Shipley MF322 developer (single puddle process), and a hard bake at 100 degC for 90 seconds. Always check the temperature of the hotplates first.

- Use development **program Dev – SP**

11. INSPECTION: LINEWIDTH

Visually inspect the wafers through a microscope, and check the linewidth. No resist residues are allowed.

12. PLASMA ETCHING OF ALIGNMENT MARKS

Use the Trikon Ωmega 201 plasma etcher.

- Use sequence **URK_NPD** and set the platen temperature to **20 °C** to etch 1200 Å deep ASM URK's into the silicon.

13. CLEANING PROCEDURE: TEPLA + HNO_3 99% and 69.5%

Plasma strip:

Use the Tepla plasma system to remove the photoresist in an oxygen plasma.

- Use **program 1**

Cleaning:

10 minutes in fuming nitric acid (Merck: HNO_3 99%) at ambient temperature.
Use wet bench "HNO_3 (99%)" and the carrier with the white dot.

QDR:

Rinse in the Quick Dump Rinser with the standard program until the resistivity is 5 MΩ.

Cleaning:

10 minutes in concentrated nitric acid (Merck: HNO_3 69.5%) at 110 °C.
Use wet bench "HNO_3 (69.5%)" and the carrier with the white dot.

QDR:

Rinse in the Quick Dump Rinser with the standard program until the resistivity is 5 MΩ.

Drying:

Use the Semitool "rinser/dryer" with the standard program, and the white carrier with a red dot.

PART 3: DRIE PREPARATION

14. BACKSIDE TEOS OXIDE DEPOSITION @ Class 100

Use the Novellus to deposit 6 µm of PECVD oxide on the **backside** of the wafer.

- For oxide deposition use reipe: **xxxnmteos @ 350°C** (check Novellus logbook for **time)**

15. BACKSIDE STD OXIDE DEPOSITION @ Class 100 (to prevent degasing)

Use the Novellus to deposit 200 nm of PECVD oxide on the **backside** of the wafer (as a capping layer for TEOS).

- For oxide deposition use reipe: **xxxstdSiO @ 400°C** (check Novellus logbook for **time)**

16. FRONTSIDE TEOS OXIDE DEPOSITION @ Class 100

Use the Novellus to deposit 6 µm of PECVD oxide on the **frontside** of the wafer.

- For oxide deposition use reipe: **xxxnmteos @ 350°C** (check Novellus logbook for **time)**

17. OXIDE THICKNESS MEASUREMENT

Use the Leitz MPV-SP measurement system to measure the oxide thickness, program: **Th. SiO2 on Si >50nm auto5pts**

18. COATING AND BAKING-BACKSIDE

Use the EVG 120 wafertrack to coat the wafers with resist. The process consists of a treatment with HMDS (hexamethyldisilazane) vapor with nitrogen as a carrier gas, spin coating with AZ ECI 3027 positive photoresist, and a soft bake at 95degC for 90 seconds. Always check the temperature of the hotplate and the relative humidity (48 ± 2 %) in the room first.

- Use coating **Co –3027 – 3,1um – noEBR** (resist thickness: 3.100 µm).

19. ALIGNMENT AND EXPOSURE

Use the EVG 420 Contact aligner to expose the photoresist.

- Use **mask** for device BE2325, layer **DRIE**.

Calculate the exposure time by consulting the contact aligner exposure energy data log.

20. DEVELOPMENT

Use the EVG 120 wafertrack to develop the wafers. The process consists of a post-exposure bake at 115 degC for 90 seconds, followed by a development step using Shipley MF322 developer (double puddle process), and a hard bake at 100 degC for 90 seconds. Always check the temperature of the hotplates first.

- Use development **program Dev – SP**.

21. INSPECTION

Visually inspect the wafers through a microscope, and check openings.

22. PLASMA ETCHING OF 6 µm TEOS OXIDE + 200nm STD OXIDE-BACKSIDE

Use the Drytek 384T plasma etcher.

- Use program **StdOxide** (8-10 nm/s) and change time to **t=15 min**

23. CLEANING PROCEDURE: TEPLA + HNO_3 99% and 69.5%

Plasma strip:

Use the Tepla plasma system to remove the photoresist in an oxygen plasma.

- Use **program 1**

Cleaning:

10 minutes in fuming nitric acid (Merck: HNO_3 99%) at ambient temperature.
Use wet bench "HNO_3 (99%)" and the carrier with the white dot.

QDR:

Rinse in the Quick Dump Rinser with the standard program until the resistivity is 5 MΩ.

Cleaning:

10 minutes in concentrated nitric acid (Merck: HNO_3 69.5%) at 110 °C.
Use wet bench "HNO_3 (69.5%)" and the carrier with the white dot.

QDR:

Rinse in the Quick Dump Rinser with the standard program until the resistivity is 5 MΩ.

Drying:

Use the Semitool "rinser/dryer" with the standard program, and the white carrier with a red dot.

PART 4: MOLYBDENUM DEPOSITION, PATTERNING AND GRAPHENE GROWTH

24. Mo DEPOSITION: 50nm

Use the TRIKON SIGMA sputter coater for the deposition of the catalyst metal (Mo) layer on the process and test wafers.

- If necessary perform a target clean with recipe **'_Trgt_Cln_Mo_50C'**.
- Use recipe **'Mo_50nm_50C'**.

Visual inspection: the metal layer must look shiny.

25. COATING AND BAKING

Use the EVG 120 wafertrack to coat the wafers with resist. The process consists of a treatment with HMDS (hexamethyldisilazane) vapor with nitrogen as a carrier gas, spin coating with AZ ECI 3027 positive photoresist, and a soft bake at 95degC for 90 seconds. Always check the temperature of the hotplate and the relative humidity (48 ± 2 %) in the room first.

- Use coating **'Co –3012 – 2.1um'** (resist thickness: 2.100 µm).

26. ALIGNMENT AND EXPOSURE

Use the EVG 420 Contact aligner to expose the photoresist.

- Use **mask** for device BE2325, layer **GRAPHENE**.

Calculate the exposure time by consulting the contact aligner exposure energy data log.

27. DEVELOPMENT

Use the EVG 120 wafertrack to develop the wafers. The process consists of a post-exposure bake at 115 degC for 90 seconds, followed by a development step using Shipley MF322 developer (double puddle process), and a hard bake at 100 degC for 90 seconds. Always check the temperature of the hotplates first.

- Use development **'program Dev – SP'**.

Inspection – Visually inspect the wafers through a microscope, and check openings.

28. PLASMA ETCHING OF Mo

Use the Trikon Ωmega 201 plasma etcher.

- Use sequence **'MoTEST2'** and set the etching time to **t=30s.**

29. CLEANING PROCEDURE: TEPLA

Plasma strip:

Use the Tepla plasma system to remove the photoresist in an oxygen plasma.

- Use **program 1** (Use it twice if there are still photoresist residues)

Visual inspection: the metal layer (protected by the photoresist) must look shiny.

30. GRAPHENE GROWTH

Use the AIXTRON BlackMagic Pro to grow graphene using LPCVD at 1000°C.

- Use recipe **'Mo_NEW_915C_20min_CH4'**.

The process wafers are now considered Cu contaminated. Beware of which tweezers to use when handling the wafers. Put the wafers in a process box dedicated for Cu contaminated processes.

PART 5: METAL DEPOSITION AND PATTERNING

31. METAL DEPOSITION

Use the TRIKON SIGMA sputter coater for the deposition of metal interface Ti+Al(1%Si) layer on the process and test wafers.

- If necessary perform a target clean with recipe **'_Trgt_Cln_Ti_50C'** and **'_Trgt_Cln_AlSi_50'**.
- Use recipe **'Ti100nmAl675-50C'**.

Visual inspection: the metal layer must look shiny.

32. COATING AND BAKING

MANUAL COATING (use brewer manual spinner and chuck for contaminated wafers):

10 mins HMDS - treatment with HMDS (hexamethyldisilazane) vapor with nitrogen as a carrier gas
Photoresist coating - Shipley SPR3012 positive photoresist spin coating (3.1 µm), and a **soft bake (using the hot plate for contaminated wafers) at 95degC for 1 min**

- Use coating **'AZ_ECI-3027-3100nm'** (resist thickness: 3.1 µm).

33. ALIGNMENT AND EXPOSURE

Use the EVG 420 Contact aligner to expose the photoresist.

- Use **mask** for device BE2325, layer **METAL**. (Use the contaminated chuck for this step)

Calculate the exposure time by consulting the contact aligner exposure energy data log.

33. DEVELOPMENT

MANUAL DEVELOPMENT

Post-exposure baking - Baking at **115degC for 1 min**
Photoresist **development** - Shipley MF322 developer for **1 min**
Inspection - Visually inspect the wafers through a microscope, and check openings
Hard baking - Baking at **100degC for 1 min (using the hot plate for contaminated wafers)**

Inspection – Visually inspect the wafers through a microscope, and check openings.

- Perform an extra baking step for 30 min at 115 °C

34. ETCHING OF Ti+Al(1%Si)

Perform this step in SAL lab.

- Use HF **0.55%** for metal etching for ~**15 min.**

35. CLEANING PROCEDURE

- Use Acetone and IPA to remove the remaining photoresist.

PART 6: FLIP-CHIP BONDING @FRAUNHOFER (BERLIN)

36. THERMOCOMPRESSION FLIP-CHIP BONDING

Perform a thermocompression flip-chip bonding procedure with/without adhesive (conductive/non-conductive)

PART 7: PDMS ENCAPSULATION-FIRST LAYER

37. PDMS MIXING

Mix **Sylgard 184 elastomer and curing agent with a ratio of 10:1** using 6 grams of elastomer per wafer. Mix and degas the solution in Thinky are-250 mixer.

38. PDMS DEPOSITION AND CURING

Use Brewer Science Manual Spinner (and chuck for contaminated wafers) to spin coat the PDMS solution on the wafer.

- Program name : **x_PDMS_50um**.
- Bake the wafer in Memmert oven for **60 minutes** at **90°C** -> fully cured PDMS layer.

PART 8: PDMS ETCHING

39. METAL DEPOSITION

Perform a LUR test before depositing metal on top of PDMS! (Use cassette for contaminated wafers)

Use the TRIKON SIGMA sputter coater for the deposition of Al(1%Si) metal layer (as a hard mask for PDMS etching and to provide mechanical stability during future DRIE steps) on the process and test wafers.

- If necessary perform a target clean with recipe **'_Trgt_Cln_AlSi_25_LP'**. (Use the cassette for clean wafers)
- Use recipe **'AlSi_500nm_1kW_25C'**. (Use cassette for contaminated wafers)

Visual inspection: the metal layer must look shiny.

40. COATING AND BAKING

MANUAL COATING (use brewer manual spinner and the chuck for contaminated wafers):

10 mins HMDS - treatment with HMDS (hexamethyldisilazane) vapor with nitrogen as a carrier gas
Photoresist coating - Shipley SPR3012 positive photoresist spin coating (3.1 μm), and a **soft bake (using the hot plate for contaminated wafers) at 90degC (or lower) for 2 min**

- Use coating **'AZ_ECI-3027-3100nm'** (resist thickness: 3.10μm).

For wafers with bonded chips, use the spray coater (and chuck for contaminated wafers) for better coverage!

41. ALIGNMENT AND EXPOSURE

Use the EVG 420 Contact aligner to expose the photoresist.

- Use **mask** for device BE2325, layer **PDMS**. (Use the contaminated chuck for this step)

Calculate the exposure time by consulting the contact aligner exposure energy data log.

42. DEVELOPMENT

MANUAL DEVELOPMENT

Post-exposure baking - Baking at **90degC (or lower) for 2 min**
Photoresist **development** - Shipley MF322 developer for **1 min**
Inspection - Visually inspect the wafers through a microscope, and check openings
Hard baking - Baking at **90degC (or lower) (using the hot plate for contaminated wafers) for 2 min**

Inspection – Visually inspect the wafers through a microscope, and check openings.

Perform an extra baking step for 1h at 90 °C (or lower)

43. ETCHING OF Al(1%Si)

Perform this step in SAL lab.

- Use HF **0.55%** for metal etching for **~15 min.**

44. CLEANING PROCEDURE

Use **Acetone + IPA** to remove the photoresist.

45. ETCHING OF PDMS

Use the Trikon Ωmega 201 plasma etcher.

Use sequence **PDMS_4** and set the platen temperature to **25 ºC**. Etch until reaching the sacrificial metal layer. Typical etch time 60-90 min. Etch rate is about 1 μm/minute.

PART 9: DRIE @ CR10000

46. DRIE FOR Si WAFER

Use AMS100 tool in CR10000 to perform a DRIE step through the Si wafer.

- Use recipe **WINOP_SINGLE** for **~90 min**.

Visually inspect the wafers to check that all structures are opened.

PART 10: OXIDE ETCHING AND Mo REMOVAL

Some of these process steps have to be performed inside SAL lab.

47. OXIDE REMOVAL

For wafers that **do not** have bonded chips:

- Use BHF 7:1 **(create your own bath)** for ~40 min to remove the remaining oxide layer. Protect the frontside of the wafer with the KOH holder for contaminated wafers.

For wafers that **do** have bonded chips:

Use AMS100 tool in CR10000 to thin down the oxide layer.

- Use recipe **OXIDE_ETSEN** in steps of **~10 min** and measure the oxide thickness.

Use Alcatel in CR100 and chuck for contaminated wafers to remove the remaining oxide layer

- Use SF_6 and CF_4 gases for this step.

48. Mo REMOVAL

Use Peroxide **(create your own bath)** for ~5 min to remove the Mo layer.

Note: At this point, graphene-on-PDMS suspended structures should be visible (graphene has a grey color).Do not dry the wafer neither with N_2 nor with the dryer.

PART 11: PDMS ENCAPSULATION-SECOND LAYER

49. PDMS MIXING

Mix **Sylgard 184 elastomer and curing agent with a ratio of 10:1** using 6 grams of elastomer per wafer. Mix and degas the solution in Thinky are-250 mixer.

50. PDMS DEPOSITION AND CURING

Use Brewer Science Manual Spinner (and chuck for contaminated wafers) to spin coat the PDMS solution on the wafer.

- Program name : **x_PDMS_50um**.
- Bake the wafer in Memmert oven for **60 minutes** at **90°C** -> fully cured PDMS layer.

51. CLEANING PROCEDURE

Use **Acetone + IPA** to remove the photoresist.

52. Al REMOVAL

This process step has to be performed inside SAL lab.

Use BHF 7:1 **(create your own bath)** to remove the Al layer.

Name: Dummy chips

Version: 1
Valid from: 29 March 2019
Made by: Andrada Velea

Run number:
Process engineer: Andrada Velea
Mentor: Sten Vollebregt

Start date processing: 01 April 2019
Estimated end date:
Contamination: No

Labs: CR100, CR10000

EKL(Else Kooi Laboratory)
DELFT UNIVERSITY OF TECHNOLOGY
Address Feldmannweg 17, 2628 CT Delft, The
P.O. Box 5053, 2600 GB Delft, The Netherlands
Phone +31 - (0)15 - 2783868
Fax : +31 - (0)15 - 2622163
Website http://ekl.tudelft.nl/EKL/Home.php

Detailed information about possible contamination:

Place/Clean Rooms used in process:
Write the sequence of used labs from start to finish.
Which (Non-standard) materials or process steps
Process step number
What kind of process or machine was used?
The other materials or wafers that contain non-green metals that are also processed in this machine

Lab/ Clean Room	Non-standard materials	Process step	Machine-process	Other materials used in machine
CR100	none	none	none	none
CR10000	none	none	none	none

If there are custom steps in a standard process or possible cross contamination materials are used: Write down the
Step number
Material
Machine/tool where the process is done
Pre and past process step numbers that are used to prevent cross contamination.

None

Step number	Material	Machine/Tool/lab	Process steps to prevent cross contamination

GENERAL RULES

CLEANROOM BEHAVIOUR

Always follow the "**Security and Behaviour**" rules when working in the EKL laboratories.

Always handle wafers with care during processing. Use cleanroom gloves and work as clean as possible!!

Use cleanroom gloves when working with vacuum equipment. Do not touch the inside or carriers with bare hands.

Always check equipment and process conditions before starting a process. Do NOT make unauthorized changes!

Directly notify the responsible staff member(s) when there are problems with equipment (like malfunction or contamination). Put the system down in the Phoenix reservation system, and turn the equipment status sign from UP or Usable to DOWN.

DO NOT TRY TO REPAIR OR CLEAN EQUIPMENT YOURSELF, and NEVER try to refresh a contaminated etch or cleaning bath! Only authorized staff members are allowed to do this.

PCC RULES

All substrates, layers and chemicals which are not CMOS compatible are considered to be "NON-STANDARD" materials, and may be contaminating.

The use of "non-standard" materials for processing in the class100 and SAL cleanroom must ALWAYS BE EVALUATED AND APPROVED by your mentor and in agreement with the PCC document.
Wafers that are contaminated may NEVER be processed in any of the equipment without permission of the Equipment owner Special precautions may have to be taken, like the use of a special substrate holder or container.

Check the PCC "Rules & Instructions" - available on the "EKL intranet webpage" - for more details.

CLASS 100 RULES

CLEANING OF WAFERS

After several hours (4 hours max) of storage wafers must always be cleaned before performing a COATING, FURNACE, EPITAXY OR DEPOSITION step.

Use the correct cleaning procedure:

- Tepla stripper ⇨ for removal of implanted or plasma etched photoresist
- Acetone ⇨ for removal of photoresist that is not implanted or plasma etched
- HNO_3 99% (Si) ⇨ for IC compatible wafers which do not need a HNO_3 69.5% step
- HNO_3 99% (Al) ⇨ for wafers which are or have been in contact with one of the following metals: like Al, Al(1%Si), Ge, Ti, Zr
- HNO_3 99% (Si) + HNO3 69.5% (Si) ⇨ for all other IC compatible wafers

Note:

- The above described cleaning procedures are only valid for IC compatible wafers with "standard" materials on them. **In all other situations follow the PCC rules (Previously to be discussed with the mentor).**
- Wafers do not have to be cleaned **after** a furnace, epitaxy or deposition step if the next process step will be performed immediately, unless the wafers are covered with particles.

FURNACE RESTRICTIONS

Wafers that are covered with photoresist or a metal layer may NEVER be processed in any of the furnaces. This also applies for wafers from which a metal layer has been removed by etching. Only alloying in tube C4 is allowed for wafers with an aluminium layer.

MEASUREMENTS

Always perform all the measurement and inspection steps, and **write down the results in your journal and in the result tables that can be found at some of the equipment!!** The results are used to check the condition of the processes and/or equipment.

It is possible to use the following Class 100 equipment to measure directly onto your (IC compatible) process wafers:

- The Leitz MPV-SP, the WOOLLAM and the SAGAX. These systems are used for thickness measurements of transparent layers. The measurements are non-destructive and without contact to the wafer surface.

- The Dektak 8 surface profilometer. This system is used for step height measurements. In this case a needle will physically scan over the wafer surface (contact measurement), which can be destructive for structures.

•The XL50 SEM. It can be used for inspection of your wafers and for width, depth or thickness measurements.

Note:

▪After certain measurements cleaning of your wafers may be required for further processing.

An extra wafer must be processed when other measurement methods will be used (like sheet resistance and junction depth measurements). These wafers cannot be used for further processing.

STARTING MATERIAL

Use **2 single side polished wafers (500 μm thickness)** and **2 single side polished wafers (300 μm thickness)** with the following specifications:

Type: p (p-type)
Orientation: <100>

Resistivity: 2-5 Ωcm

Thickness: 500 ± 15 μm; 300 ± 5 μm

Diameter: 100 mm

Number of wafers: 4

PROCESS DESCRIPTION

The aim of the current process is to develop dummy chips for testing the flip-chip bonding process. The chips will only have the metal layer and the contact openings.

The process consists of 5 parts:

Part 1: Cleaning step
Part 2: Creation of zero layer
Part 3: Thermal oxide deposition
Part 4: Creation of metal layer and interconnections
Part 5: Creation of contact openings

PART 1: CLEANING STEP

Perform this step ONLY when wafers are taken out of an already opened box!

1. CLEANING PROCEDURE: HNO_3 99% and 69.5%

Cleaning:

10 minutes in fuming nitric acid (Merck: HNO_3 99%) at ambient temperature.
Use wet bench "HNO_3 (99%)" and the carrier with the white dot.

QDR:

Rinse in the Quick Dump Rinser with the standard program until the resistivity is 5 MΩ.

Cleaning:

10 minutes in concentrated nitric acid (Merck: HNO_3 69.5%) at 110 °C.
Use wet bench "HNO_3 (69.5%)" and the carrier with the white dot.

QDR:

Rinse in the Quick Dump Rinser with the standard program until the resistivity is 5 MΩ.

Drying:

Use the Semitool "rinser/dryer" with the standard program, and the white carrier with a red dot.

PART 2: CREATION OF ZERO LAYER

2. COATING AND BAKING

Use the EVG 120 wafertrack to coat the wafers with resist. The process consists of a treatment with HMDS (hexamethyldisilazane) vapor with nitrogen as a carrier gas, spin coating with Shipley SPR3012 positive photoresist, and a soft bake at 95degC for 90 seconds. Always check the temperature of the hotplate and the relative humidity (48 ± 2 %) in the room first.

- Use coating **Co – Zero Layer** (resist thickness: 1.400 µm).

3. ALIGNMENT AND EXPOSURE

Processing will be performed on the ASM PAS 5500/80 automatic waferstepper.

- Use **COMURK mask**, die-size 10x10 mm, job: **litho/Zefwam**, energy (120 mJ/cm^2).

4. DEVELOPMENT

Use the EVG 120 wafertrack to develop the wafers. The process consists of a post-exposure bake at 115 degC for 90 seconds, followed by a development step using Shipley MF322 developer (single puddle process), and a hard bake at 100 degC for 90 seconds. Always check the temperature of the hotplates first.

- Use development **program Dev - SP**

5. INSPECTION: LINEWIDTH

Visually inspect the wafers through a microscope, and check the linewidth. No resist residues are allowed.

6. PLASMA ETCHING OF ALIGNMENT MARKS

Use the Trikon Ωmega 201 plasma.

- Use sequence **URK_NPD** and set the platen temperature to **20 °C** to etch 1200 Å deep ASM URK's into the silicon.

7. CLEANING PROCEDURE: TEPLA + HNO_3 99% and 69.5%

Plasma strip:

Use the Tepla plasma system to remove the photoresist in an oxygen plasma.

- Use **program 1**

Cleaning:

10 minutes in fuming nitric acid (Merck: HNO_3 99%) at ambient temperature.
Use wet bench "HNO_3 (99%)" and the carrier with the white dot.

QDR:

Rinse in the Quick Dump Rinser with the standard program until the resistivity is 5 MΩ.

Cleaning:

10 minutes in concentrated nitric acid (Merck: HNO_3 69.5%) at 110 °C.
Use wet bench "HNO_3 (69.5%)" and the carrier with the white dot.

QDR:

Rinse in the Quick Dump Rinser with the standard program until the resistivity is 5 MΩ.

Drying:

Use the Semitool "rinser/dryer" with the standard program, and the white carrier with a red dot.

PART 3: THERMAL OXIDE DEPOSITION

8. WET OXIDATION: 300nm thermal SiO2 deposition

Use furnace tube C1 to deposit 300nm of thermal SiO2 on the wafers.

Use an oxide growth calculator to calculate the **time** needed to reach the desired thickness. Check cleanroom.byu.edu/OxideTimeCalc or www.lelandstanfordjunior.com/thermaloxide.html or lelandstanfordjunior.com

- Use recipe **'WET1000'**. **Time~42 min**
- Use the Leitz MPV-SP measurement system to measure the oxide thickness, program: **Th. SiO2 on Si >50nm auto5pts.**

PART 4: CREATION OF METAL LAYER AND INTERCONNECTIONS

9. METALLIZATION: 1475nm @ 350 °C OF Al(1%Si)

Use the TRIKON SIGMA sputter coater for the deposition of the aluminium layer.

- If necessary, perform a target clean with recipe: **_Trgt_Cln_AlSi_350C.**
- Use recipe: **AlSi_1475nm_350C.**

10. COATING AND BAKING

Use the EVG 120 wafertrack to coat the wafers with resist. The process consists of a treatment with HMDS (hexamethyldisilazane) vapor with nitrogen as a carrier gas, spin coating with Shipley SPR3012 positive photoresist, and a soft bake at 95degC for 90 seconds.

Always check the temperature of the hotplate and the relative humidity (48 ± 2 %) in the room first.

- Use coating **1 - Co - 3012 – 2.1µm** (resist thickness: 2.100 µm).

11. ALIGNMENT AND EXPOSURE

Use the EVG Contact Aligner to expose the photoresist.

- Use **mask TNW2019-VI-IC.**

Calculate the exposure time **(~300mJ/cm^2)** by consulting the contact aligner exposure energy data log.

12. DEVELOPMENT

Use the EVG 120 wafertrack to develop the wafers. The process consists of a post-exposure bake at 115 degC for 90 seconds, followed by a development step using Shipley MF322 developer (single puddle process), and a hard bake at 100 degC for 90 seconds. Always check the temperature of the hotplates first.

- Use development **program Dev - SP**

13. INSPECTION: LINEWIDTH

Visually inspect the wafers through a microscope, and check the linewidth. No resist residues are allowed.

14. PLASMA ETCHING: 1475nm OF Al

Use the Trikon Ωmega 201 plasma etcher.

- Use recipe: **Al14_350 @25 °C.**

15. METAL FENCE REMOVAL

Plasma strip:

Use the Tepla plasma system to remove the photoresist in an oxygen plasma.

- Use **program 1**

Moisten:

Rinse for **1 minute** in wet bench "H_2O/Triton-X 100 tbv Al.Ets".
Use the carrier with the yellow dot.

Etching:

30 seconds in wet bench "Al. ets 35 °C".
Use the carrier with the yellow dot.

QDR:

Rinse in the Quick Dump Rinser with the standard program until the resistivity is 5 MΩ.

Drying:

Use the "Avenger Ultra-Pure 6" rinser/dryer with the standard program and the carrier with a black dot.

16. CLEANING PROCEDURE: HNO_3 99% METAL

NOTE: DO NOT PERFORM A "HNO_3 69,5% 110C (Si)" CLEANING STEP !!!

Cleaning:

10 minutes in fuming nitric acid (Merck: HNO_3 99%) at ambient temperature.
Use wet bench "HNO_3 (99%) (**metal)**" and the carrier with a red and yellow dot.

QDR:

Rinse in the Quick Dump Rinser with the standard program until the resistivity is 5 MΩ.
Drying:

Use the Semitool "rinser/dryer" with the standard program, and the white carrier with a black dot.

PART 5: CREATION OF CONTACT OPENINGS

17. NOVELLUS STD OXIDE DEPOSITION: 800nm

Use Novellus to deposit 800nm of PECVD oxide on top of the metal layer.

- For oxide deposition use recipe: **xxxstdSiO @ 400 °C** (check Novellus logbook for **time**).

18. COATING AND BAKING

Use the EVG 120 wafertrack to coat the wafers with resist. The process consists of a treatment with HMDS (hexamethyldisilazane) vapor with nitrogen as a carrier gas, spin coating with Shipley SPR3012 positive photoresist, and a soft bake at 95degC for 90 seconds. Always check the temperature of the hotplate and the relative humidity (48 ± 2 %) in the room first.

- Use coating **1 - Co - 3012 – 2.1µm** (resist thickness: 2.100 µm).

19. ALIGNMENT AND EXPOSURE

Use the EVG Contact Aligner to expose the photoresist.

- Use **mask TNW2019-VI-CO.**

Calculate the exposure time **(~320mJ/cm^2)** by consulting the contact aligner exposure energy data log.

20. DEVELOPMENT

Use the EVG 120 wafertrack to develop the wafers. The process consists of a post-exposure bake at 115 degC for 90 seconds, followed by a development step using Shipley MF322 developer (single puddle process), and a hard bake at 100 degC for 90 seconds. Always check the temperature of the hotplates first.

- Use development **program Dev - SP**

21. INSPECTION: LINEWIDTH

Visually inspect the wafers through a microscope, and check the linewidth. No resist residues are allowed.

PLASMA ETCHING OF 800nm OF OXIDE

Use the Drytek 384T plasma etcher.

- Use program **Oxstdlnd** (8-10 nm/s for ~700nm @ 300W and (8-10)/3 nm/s for ~100nm+overetch @ 100W) and change time accordingly.

CLEANING PROCEDURE: TEPLA + HNO_3 99% METAL

Plasma strip:

Use the Tepla plasma system to remove the photoresist in an oxygen plasma.
Follow the instructions specified for the Tepla stripper, and use the quartz carrier.
Use program 1

Cleaning:

10 minutes in fuming nitric acid (Merck: HNO_3 99%) at ambient temperature.
Use wet bench "HNO_3 (99%) (**metal)**" and the carrier with a red and yellow dot.

QDR:

Rinse in the Quick Dump Rinser with the standard program until the resistivity is 5 MΩ.
Drying:

Use the Semitool "rinser/dryer" with the standard program, and the white carrier with a black dot.

NOTE: DO NOT PERFORM A "HNO_3 69,5% 110C (Si)" CLEANING STEP !!!